CONTROLLING ELECTROMAGNETIC WAVES WITH ACTIVE GRAPHENE DEVICES

A THESIS SUBMITTED TO
THE GRADUATE SCHOOL OF ENGINEERING AND SCIENCE
OF BILKENT UNIVERSITY
IN PARTIAL FULFILLMENT OF THE REQUIREMENTS FOR
THE DEGREE OF
DOCTOR OF PHILOSOPHY
IN
PHYSICS

By
Osman Balcı
September, 2015

CONTROLLING ELECTROMAGNETIC WAVES

WITH ACTIVE GRAPHENE DEVICES

By Osman Balcı

September, 2015

We certify that we have read this thesis and that in our opinion it is fully adequate, in scope and in quality, as a dissertation for the degree of Doctor of Philosophy.

_____

Asst. Prof. Dr. Coşkun Kocabaş (Advisor)

_____

Prof. Dr. Hayrettin Köymen

_____

Prof. Dr. Oğuz Gülseren

_____

Prof. Dr. Raşit Turan

_____

Assoc. Prof. Dr. Hakan Altan

Approved for the Graduate School of Engineering and Science:

_____

Prof. Dr. Levent Onural
Director of the Graduate School

Copyright Information

ABSTRACT

CONTROLLING ELECTROMAGNETIC WAVES WITH ACTIVE GRAPHENE DEVICES

Osman Balcı
Ph.D. in Physics
Advisor: Asst. Prof. Dr. Coşkun Kocabaş
September, 2015

The dynamic control of electromagnetic waves forms the basis of modern communication technologies. Although sources of microwaves can be controlled by electrical means, the active control of microwaves in the free space has been a challenge due to the lack of an active material. Graphene, the 2-dimensional crystal of carbon, provides a unique platform to control light-matter interaction in a broad spectrum. This thesis describes a new approach to control microwaves using large area active graphene devices. Our strategy relies on electrostatic tuning of the density of high mobility charge carriers on an atomically thin graphene electrode which operates as a tunable metal in microwave frequencies. We developed a method to synthesize large area graphene (20x20 cm^2) by chemical vapor deposition. Using large area graphene electrodes, we demonstrate a new class of active surfaces capable of real-time electrical control of reflection, transmission, and absorption of microwaves over a broad spectrum. These active devices allow us to fabricate electrically tunable microwave surfaces such as switchable radar absorbing surfaces and tunable metamaterials with modulation depth of $50dB$ and operation voltage of $3V$. Large modulation depth, simple device architecture, and mechanical flexibility are the key attributes of the graphene-enabled active microwave surfaces that could find a wide range of applications ranging from active signal processing to adaptive camouflage.

Keywords: Graphene, Microwave Modulator, Radar Absorbers, Active Metadevices.

ÖZET

ELEKTROMANYETİK DALGALARIN AKTİF GRAFEN AYGITLARI İLE KONTROL EDİLMESİ

Osman Balcı
Fizik, Doktora
Tez Danışmanı: Yr. Doç. Dr. Coşkun Kocabaş
Eylül, 2015

Elektromanyetik dalgaların dinamik olarak kontrol edilmesi modern iletişim teknolojilerinin temelini oluşturmaktadır. Mikrodalga kaynaklarının kolaylıkla kontrol edilebiliyor olmasına rağmen, kaynaktan ayrılan mikrodalgaların boş uzayda kontrol edilmesi mikrodalgada kullanılabilecek aktif bir malzemenin olmayışından dolayı çözülmesi gereken çok önemli bir problemdir. Bu tezde geniş alanlı grafenden elde edilmiş aygıtlar kullanarak mikrodalgaların yeni bir yaklaşım ile kontrol edilmesi anlatılmaktadır. Kullandığımız teknikte atomik derecede ince olan ve mikrodalga frekanlarında degişken bir metal gibi davranabilen grafen elektrotlar üzerindeki yük yoğunluğunu elektrostatik olarak kontrol ediyoruz. Geniş alanlı ($20x20cm^2$) grafen tabakaları kimyasal buhar yükleme sistemi kullanılarak sentezlenmiştir. Bu geniş alanlı grafen tabakalarını kullanarak geliştirdiğimiz aygıt sayesinde mikrodalgaların geniş bir band aralığında geçirgenliğini, yansımasını, ve emilmesini elektriksel olarak kontrol edebiliyoruz. Bu aktif yüzeyler sayesinde açılıp kapatılabilir radar emici yüzeyler ve kontrol edilebilir metamalzemeler 50dB genlik seviyelerine kadar sadece 3V voltaj uygulayarak kontrol edilebilmiştir. Yüksek mudülasyon oranı, basit aygıt yapısı ve meknik esnekliği, üretilen mikrodalga modülatörlerinin en önemli özellikleri ve bu aygıtlar aktif sinyal işletiminde, kontrollü görünmezlik araştırmalarında geniş bir uygulama alanı bulabilir.

Anahtar sözcükler: Grafen, mikrodalga modülatörler, radar emiciler, aktif meta-aygıtlar.

Acknowledgement

Although this thesis belongs to me, many people contributed to this thesis. This short acknowledgement section is not enough to thank all of them one by one hence I would like to thank everyone contributing to this theses all at once here.

I have been educated in Bilkent University with a full scholarship during both my B.S. and Ph.D. study. I learned almost everything that I know in Bilkent University. Therefore, I would like to first thank to Bilkent University for giving me such a unique and high quality scientific and social education.

It was an honor and great chance for me to work with my advisor Asst. Prof. Dr. Coskun Kocabas during my Ph.D. study. He has endless ambition to work without considering the time. We have found a lot of new ideas and methods together during "Friday afternoon" experiments. His quick and smart problem solving ability save me from many desperate conditions. He taught me many useful "research hacks" that I will certainly use in my future life. We spent almost six years in my Ph.D. study, I owe all my scientific achievements to him. I learned a lot from him, I will follow his lead in the future. I would like to express my sincere thanks and gratitude to him for everything.

I am grateful to members of my thesis committee Prof. Dr. Oğuz Gülseren and Prof. Dr. Hayrettin Köymen. They attended eight thesis progress presentations and they supported and guided me through all my PhD. study.

I would like to thank diroctory of Advanced Research Labarator (ARL), Prof. Dr. Atilla Aydınlı. He spent a lot of time for the problems of ARL and he provided us one of the best labaratory and office conditions in Turkey.

I would like to express my gratitute to my brother Asst. Prof. Dr. Sinan Balci and also his family. He encouraged me to work in the hard times of my Ph.D. He shared

his valuable scientific experiences with me throughout my Ph.D. He and his family made me to feel not alone through six years. We had many discussions together on scientific, family, social and daily topics. Thank you brother for everything.

I would like to express my gratitude to all current and former group mates; Dr. Omer Salihoglu, Dr. Emre Ozan Polat, Nurbek Kakenov, Dr. Ivgenia Kovalska, Shahnaz Aas, Pınar Köç, Erçağ Pinçe, Melih Okan. We worked on different projects together, I learned many things from each of them. They helped me a lot during my Ph.D. study and they had a considerable amount of contribution to this thesis. They are all friendly and hardworking scientists, I am sure each of them will be in the position that they want to be. I will miss our discussions in the office. Many thanks to each of them.

I would like to thank undergrads Onur Çakıroğlu, Burkay Uzlu, and Muhammed Bilgin. We work together in the last months of my Ph.D., they are such a hardworking and smart guys.

I would like to thank Prof. Dr. Ekmel Özbay, Dr. Semih Çakmakyapan and Dr. Ertuğrul Karademir for colobrating with us for the simulation of active metadevices.

I would like to thank Ergün Karaman, Elvan Ogün and all the ARL stuffs for their valuable technical and secreterial support.

I would like to thank TÜBİTAK-BİDEB for the scholarship program 2211-DOKTORA BURS PROGRAMI in which I had been a scholar.

I would like to thank TÜBİTAK for the projects (114F052, 113F278, 112T686, 109T259) which I worked in and got scholarship from.

I would like to thank all my family; my mother Şadiye Balcı, my father Mustafa Balcı, my brothers, and my sisters. I could not succeed anything without you.

Finally, I would like to thank my wife Hatice Balcı and my son Mustafa Selim Balcı. Everything I achieved is yours. I dedicate this thesis to you.

Osman Balcı

…..to my wife and son

Contents

List of Figures

List of Tables

Chapter 1

Introduction

Graphene is a new candidate for an active material to investigate light matter interactions. Monoatomic thickness, linear band structure, high mobility charge carriers together with the electrical tunability are the key physical properties that make graphene unique to control electromagnetic waves in a very broad spectrum. This broad optical response originates from interband and intraband electronic transitions. In visible and near infrared frequencies, interband transitions yields a universally constant optical conductivity of $\sigma = e^2/4\hbar$ where e is the charge of electron and $\hbar$ is Planck's constant. As a consequence of that graphene can absorb at most $\sim 2.24\%$ of the incident radiation (Figure 1.1) [1]. This broadband constant optical conductivity can be blocked by doping. When the Fermi energy of graphene is above half of the incident radiation energy, Pauli blocking suppresses the interband transitions hence graphene becomes transparent below that energy. For long wavelengths, from far infrared to microwave region, graphene has a frequency dependent optical conductivity of $\sigma(\omega) = \sigma_0/(1 - i\omega\tau)$ due to the dominant intraband transitions where ω is frequency and τ is scattering time. For this regime, the optical conductivity of graphene is due to intraband transitions and it can be enhanced by doping. In the free standing form, doped graphene can absorb at most 50% of incident radiation when the impedance of the graphene matches the half

of free space impedance (377Ω) (Figure 1.1). This significant amount of absorption can be tuned by varying the charge density of graphene (Figure 1.1). This tunable optical absorption over a broad spectrum makes graphene a unique material for optoelectronic applications. Figure 1 summaries some possible applications based on tunable optical absorption of single layer graphene.

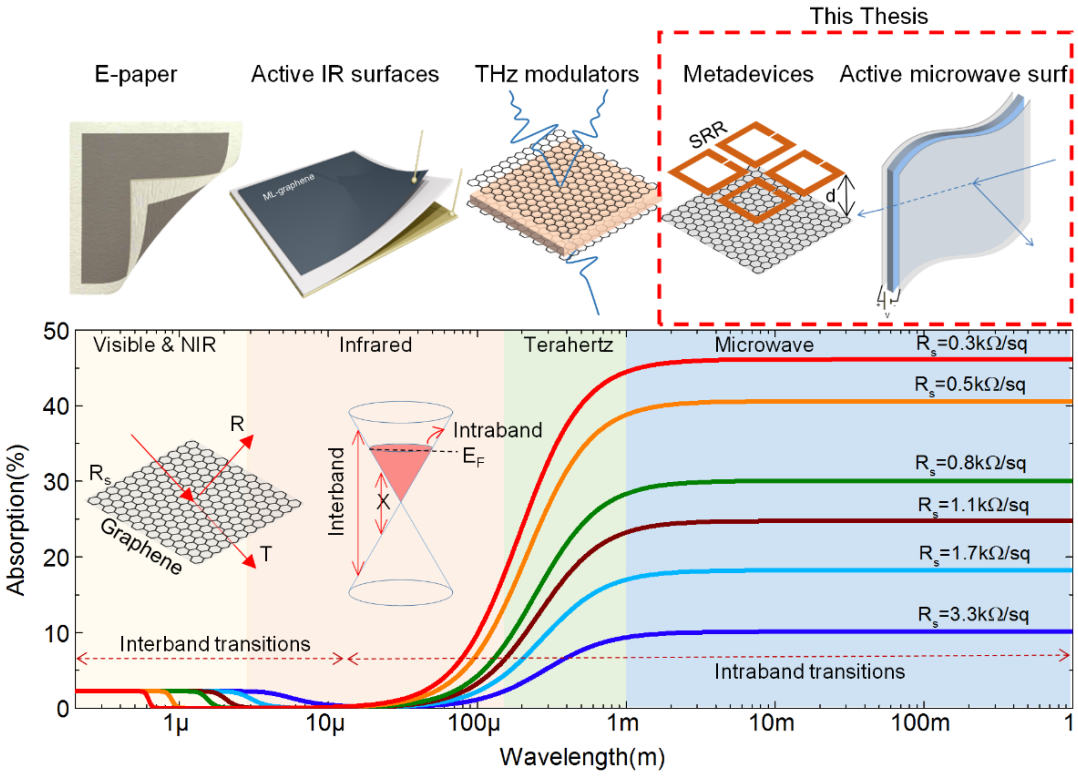

Figure 1.1 Graphene based optoelectronic devices working in various wavelengths investigated by our group. The highlighted devices in the microwave regime are investigated during my Ph.D. study. This thesis will describe the fabrication and characterization of these devices. The graph shows the calculated optical absorption of single layer graphene which yields controllable optical absorption in a very broad electromagnetic spectrum. Although the amount of absorption in visible and infrared wavelengths is small, especially for the long wavelength region tunability is as high as 50%.

Although the main stream graphene research is focused on electronic applications, recently, there has been various device structures investigated to tune the optical properties of graphene from visible to terahertz frequencies. Feng Wang et al. develops a gate tunable absorption in infrared for the first time [2] and Li et al. investigated the optical properties of graphene by varying conductivity of graphene again in the infrared [3]. Ming Liu et al. developed a broadband electro optical modulator mounted on top of a waveguide working in near-infrared wavelengths [4]. Polat et al. investigated for the first time a broadband graphene modulator working in the visible and near-infrared by using self-gated graphene supercapacitors [5] and they improved the method for the multilayer graphene modulators to increase the modulation performance of the device [6]. Rodriguez et al. investigated broadband graphene terahertz modulators and absorbers [7, 8]. Further, Kakenov et al. developed high performance terahertz spatial light modulators using self-gating device structure [9]. Graphene modulators were integrated also with terahertz metamaterials to tune amplitude and frequency of the metamaterials [10-14]. The optical properties of graphene for the visible and infrared region have been investigated in detail. However, the microwave region of the electromagnetic spectrum has not been investigated due the long wavelength and requirement of large area graphene devices. This thesis aims to bridge this gap by overcoming the challenging growth and fabrication processes for active microwave devices. Our strategy is to synthesize large area graphene samples using chemical vapor deposition and to develop transfer printing technique. After achieving high quality graphene samples, we fabricated large area active graphene devices using self-gated supercapacitor structures. Self-gated graphene supercapacitors provides a homogenous doping over a large surface area. In this thesis I will describe the details of the growth, fabrication, and characterization of these devices.

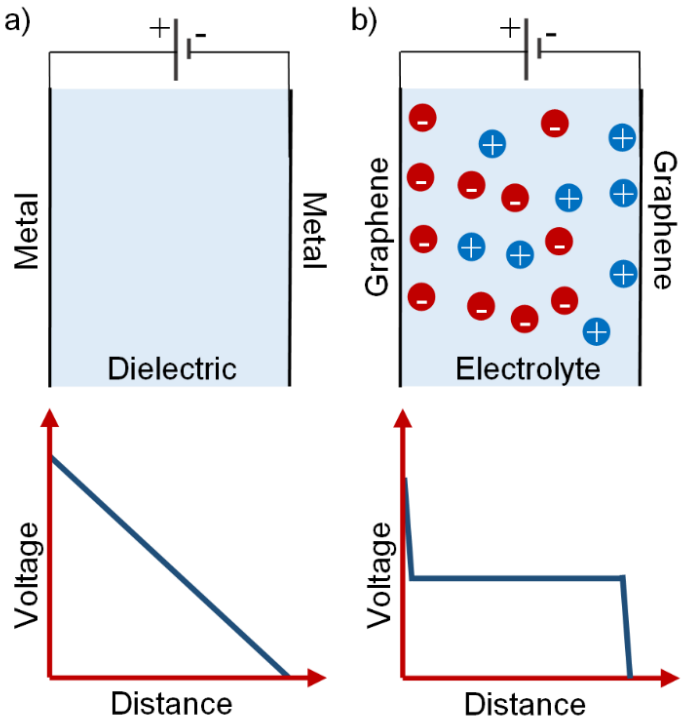

Figure 1.2 Comparison of (a) a dielectric capacitor and (b) a graphene supercapacitor.

Using graphene supercapacitors to control microwaves is the core idea of this thesis. Supercapacitor structure yields a self-gating scheme between two large area graphene. Self-gating with an ionic liquid electrolyte is the key parameter to achieve large and homogenous modulation of charge density over large area. Our group has been working on graphene supercapacitors based on single- and multi-layer graphene to control various wavelength (schematics in Figure 1.1). We would like to use graphene supercapacitors as a reconfigurable surface for microwave applications. We fabricated these supercapacitors (sometimes called electrical double layer capacitors) using large area graphene electrodes synthesized by chemical vapor deposition. A conventional dielectric-based capacitor uses two metal electrodes and a dielectric medium. Applied voltage between the electrodes generates homogeneous electric field between the plates and thus the voltage drops linearly on the dielectric.

Supercapacitors are different. Supercapacitors consist of two electrodes and electrolyte medium. Applied voltage polarizes the electrolyte and forms ionic double layers on the electrode surface. The thickness of these ionic double layers is very thin (a few nanometers limited by the diffusion of ions), therefore applied voltage drops sharply at the ionic double layer and generates very large electric field on the surface of electrodes (Figure 1.2(b)). We will use graphene supercapacitors where the electrodes are atomically thin graphene layers. As an electrolyte we will use ionic liquids which yield very good electrochemical stability with graphene electrodes up to 7 V electrochemical window. The electric field of the ionic double layers electrostatically dopes the graphene electrodes and accumulates charges. Unlike metallic electrodes, conductivity of atomically thin graphene electrodes varies with accumulated charges. The ability of tuning charge density on graphene electrodes yields a unique opportunity to control high mobility free charges on graphene surfaces. The maximum resistivity is reached at the Dirac point, where Fermi energy is the intersection point of the conduction and valance band. For the doped case, the charge density on graphene electrodes could be as large as 10^{14} cm^{-2} with associated Fermi energy of 1.5 eV. These charge densities cannot be achieved with conventional dielectric capacitor due to the dielectric breakdown. Another important property of the supercapacitors is that they store charges at the graphene-electrolyte interface. There is no electrochemical reaction (which is the case for batteries) that can yield detrimental effects on graphene electrodes.

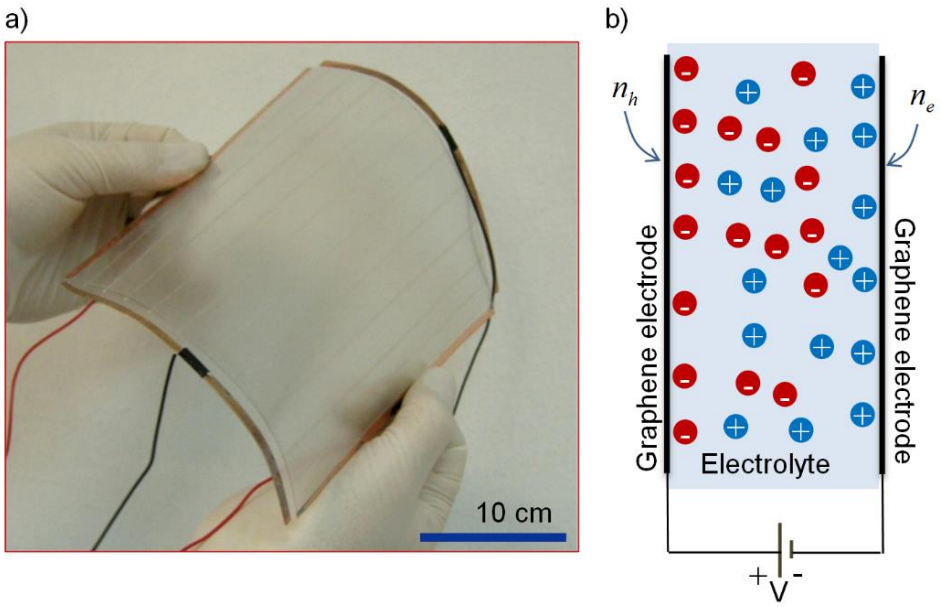

Figure 1.3 The photograph of large area graphene supercapacitor (a) and schematic explanation of ionic gating of graphene electrodes by an ionic liquid (b).

In this thesis, we use large area graphene supercapacitors (Figure 1.3) for the first time to control electromagnetic waves in the microwave frequencies. We have developed three different kinds of device structures. First one is a transmission type broadband microwave modulator fabricated by using two large area graphene electrodes with an ionic liquid between them. This device tunes the reflection, transmission, and absorption of microwaves from the surface of the device by applying bias voltage between two graphene electrodes. Second one is a reflection type radar absorbing surface. Here we use a large area graphene supercapacitor with a metal plate located at quarter wavelength distance below the device. This reflection type surface attenuates the reflected radiation at the resonance frequency. Our third device is achieved by integrating a large area graphene supercapacitor with a split ring resonator (SRR) array. Graphene capacitor is capacitively coupled with the SRR array, tuning the charge density on the graphene electrodes tunes the resonance amplitude and frequency of the hybrid metadevice.

Before going through the details of these active modulators, I will first introduce the fundamentals of graphene in this chapter which covers the electronic band structure and optical conductivity. In chapter 2, I calculate optical absorption of graphene in whole non-ionizing electromagnetic spectrum by solving Maxwell equations on graphene surface and I use a transfer matrix method for numerical calculation. In chapter 3, I explain the details of graphene synthesis and characterization and then we express the details for the fabrication of large area graphene capacitors with characterization processes. In chapter 4, I explain the performance and characteristics of transmission type adaptive microwave surfaces and reflection type switchable radar absorbing surfaces. In chapter 5, I report an application for our method. I integrated our active devices with microwave metamaterials and realized large area electrically switchable metadevices. I also provide electromagnetic modelling, fabrication and microwave measurements of these metadevices.

1.1.Electronic band structure of graphene

Graphene is the 2D crystal of carbon, each atom is bonded to three carbon atoms and forms a hexagonal atomic structure as shown in Figure 1.4. Carbon atom has different bonding mechanism when it is in a ground state[15]. In ground state, each carbon atom has six electrons and these electrons fill the energy levels of the carbon atom as $1s^2 2s^2 2p^2$ where the $2p^2$ state is partially filled as $2p_x^1 2p_y^1 2p_z^0$. The two electrons in $1s^2$ state are the core electrons and they do not contribute to chemical bonding or electronic properties of the carbon atom. The four electrons in $2s^2 2p^2$ states are called valance electrons and they define electronic properties of a carbon based materials. In its ground state a carbon atom can only make two bonds by using its two half-filled $2p$ orbitals as in CH_2. However, when a carbon atom is in the excited state, it can make four bonds by exiting one electron from $2s$ orbital to the a $2p$ orbital,

four half-filled electronic state give rise to more than two chemical bonds for a single carbon atom in a crystal. The energy difference between higher energy $2s$ orbitals and lower energy $2p$ orbitals is small compared to the chemical binding energies, therefore, the wave functions of electrons in these two energy orbitals are mixed. Hybridizations are when one electron from the $2s$ orbital hybridize with one(sp), two (sp^2) or three(sp^3) electrons from $2p$ orbitals. These hybridized electronic states forms σ bonds with hydrogen atom or carbon atom itself and remaining half-filled $2p$ orbitals form the π bonds between carbon atoms and they are perpendicular to the σ bonds.[15] This variety of hybridization results in a wide variety of carbon based materials.

In graphene, there is sp^2 hybridization, one of the electrons from $2s$ orbital and two$(2p_x 2p_y)$ of electrons from $2p$ orbital mix their wave functions and they hybridize in a new energy state as explained in Ref.[15] and Ref.[16]. These hybridized orbitals create strong σ bonds between a carbon atom and its three nearest neighbors, this strong bond gives rise to the stability of graphene in 2-dimension. Un-hybridized $2p_z$ orbital creates π orbitals which are perpendicular to the graphene plane. π Electrons are responsible for all transport and electronic structure of graphene and graphene based materials. Tight binding calculation of these π electrons gives the electronic band structure of graphene, which means that the interaction between these electrons creates an energy-band diagram where energy-momentum combination of any charge carrier is defined by the band structure. To calculate electronic band structure of graphene, we need to know the crystal structure of graphene drawn schematically in Figure 1.4. In this hexagonal crystal structure of graphene, blue and red dots represent the carbon atoms in hexagonal graphene lattice. It is assumed that the red dots are the lattice points and the blue dots are the sub-lattice points. The sub-lattice points are connected to the lattice points by any one of $\overrightarrow{b_{1,2,3}}$ vectors as in Ref.[16]. The vectors $\overrightarrow{a_1}$ and $\overrightarrow{a_2}$ are the lattice vectors of the triangular lattice and they can be written as

$$\overrightarrow{a_1} = \frac{a}{2}(3, \sqrt{3}) \quad , \quad \overrightarrow{a_2} = \frac{a}{2}(3, -\sqrt{3}) \tag{1.1}$$

Where $a \approx 1.42A^o$ is the distance between carbon atoms. The vectors $\overrightarrow{b_1}$, $\overrightarrow{b_2}$ and $\overrightarrow{b_3}$ show the first nearest neighbor position of the carbon atom at lattice point and they can be written in terms of lattice vectors as

$$\overrightarrow{b_1} = \frac{a}{2}(1, \sqrt{3}) \quad , \quad \overrightarrow{b_2} = \frac{a}{2}(1, -\sqrt{3}) \quad , \quad \overrightarrow{b_1} = -a(1,0) \tag{1.2}$$

It is possible to consider the second, third and higher order nearest neighbor interactions during calculation of the electronic band structure of graphene by tight binding method. However, it is not practical and necessary to consider higher order nearest neighbor interactions. Therefore, we calculated band structure of graphene by only considering the first nearest neighbor interactions as in Ref.[15].

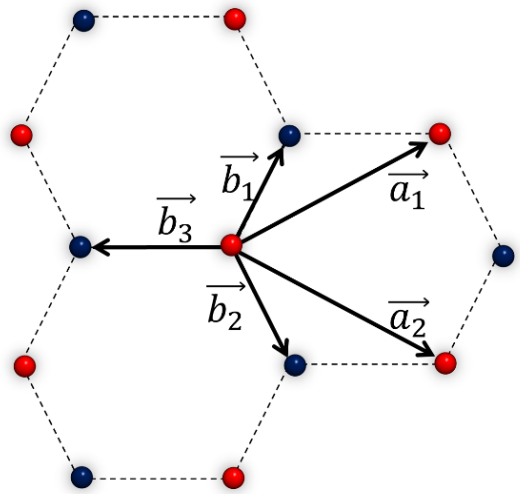

Figure 1.4: Schematic drawing of hexagonal lattice structure of graphene. Red and blue dots represent the carbon atoms in graphene structure and red dots are assumed to be the lattice points for a triangular lattice. Blue dots are sub-lattices which are connected to a lattice point with a basis vector. Here we assume any one of $\overrightarrow{b_{1,2,3}}$ vectors as a basis vector. The vectors $\overrightarrow{a_1}$ and $\overrightarrow{a_2}$ are lattice vectors and $\overrightarrow{b_1}$, $\overrightarrow{b_2}$ and $\overrightarrow{b_3}$ are the vectors showing the nearest neighbor position of a carbon atom relative to a lattice point. The side length of a hexagon is a.

Graphene has π electrons in its unit cell and the π electrons determine the extraordinary electrical, optical and mechanical properties of graphene. Tight binding calculation takes account π electrons to calculate band structure of graphene. In fact there are also σ electrons in the graphene unit cell but π electrons are more dominant in low energy regimes. Therefore we only considered π electrons during the calculation of band structure of graphene as in Ref.[15]. Graphene has a two dimensional atomic crystal structure and hence it has a unit cell. Therefore, graphene has a translational symmetry. The wave function in a unit cell satisfies the Bloch`s theorem;

$$T_{\overrightarrow{a_i}}\Psi = e^{i\vec{k}.\overrightarrow{a_i}}\Psi \ , \quad (i = 1,2,3) \tag{1.3}$$

Where $T_{\overrightarrow{a_i}}$ is the translation operator and, $\overrightarrow{a_i}$ is the lattice vector and $\overrightarrow{k_i}$ is the wave vectors. Ψ is the wave function in a unit cell and has the form as

$$\varphi_j(\vec{k},\vec{r}) = \frac{1}{\sqrt{N}}\sum_{\vec{R}}^{N} e^{i\vec{k}.\vec{r}}\,\varphi_j(\vec{r}-\vec{R}) \ , \ (j = 1,\dots,n) \tag{1.4}$$

Where φ_j denotes the atomic wave function in a unit cell and $\vec{R}$ is the position of the atom in a unit cell, n is the number of atoms in a unit cell. The eigenfunctions can be written as a linear combination of Bloch`s wave functions as

$$\Psi_j(\vec{k},\vec{r}) = \sum_{i}^{n} C_{ij}(\vec{k})\varphi_i(\vec{k},\vec{r}) \tag{1.5}$$

Eigenvalues of these eigenfunctions can be calculated by evaluating the expectation value of Hamiltonian as

$$E_j(\vec{k}) = \frac{\langle\Psi_j|H|\Psi_j\rangle}{\langle\Psi_j|\Psi_j\rangle} \tag{1.6}$$

By inserting the Bloch function from Eq.(1.4) in to Eq.(1.6), the transfer and overlap integral matrices can be calculated as

$$H_{ij}(\vec{k}) = \langle \varphi_i | H | \varphi_j \rangle , \quad S_{ij}(\vec{k}) = \langle \varphi_i | \varphi_j \rangle \quad (i,j = 1, \dots, n). \tag{1.7}$$

Here i, j show the number of atoms in the unit cell, for example, the number of atoms in a unit cell of graphene is two, one is at lattice point and the other one is at $\overrightarrow{b_1}$ position as shown in Figure 1.4 and Eq.(1.2). Let us assume that the atom at the lattice point is represented with A and the other atom in the unit cell is represented with B. The calculation over atoms A and B only gives the orbital energy of the $2p$ orbital as shown below

$$H_{AA} = H_{BB} = \varepsilon_{2P} \tag{1.8}$$

By considering only the first nearest neighbor interaction, we can calculate off-diagonal elements of Hamiltonian as

$$H_{AB} = t\left(e^{i\vec{k}.\overrightarrow{b_1}} + e^{i\vec{k}.\overrightarrow{b_2}} + e^{i\vec{k}.\overrightarrow{b_3}}\right) = tf(k) \tag{1.9}$$

Where $\overrightarrow{b_{1,2,3}}$ are the position vectors of first nearest neighbors as shown in Figure 1.4 and Eq.(1.2). Using coordinates from Eq.(1.2), $f(k)$ is calculated as

$$f(k) = e^{ik_x a} + 2e^{\frac{-ik_x a}{2}}\cos(\frac{k_y a\sqrt{3}}{2}) \tag{1.10}$$

The overlap integral values are calculated as $S_{AA} = S_{BB} = 1$ and the off-diagonal terms are $S_{AB} = S_{BA} = sf(k)$. Finally the transfer and overlap matrices become as

$$H = \begin{pmatrix} \varepsilon_{2p} & tf(k) \\ tf(k)^* & \varepsilon_{2p} \end{pmatrix} \quad , \quad S = \begin{pmatrix} 1 & sf(k) \\ sf(k)^* & 1 \end{pmatrix} \tag{1.11}$$

Eigen values are calculated by solving the secular equation $\det(H - ES) = 0$, which gives

$$E_{\pm}(\vec{k}) = \frac{\varepsilon_{2p} \pm tw(\vec{k})}{1 \pm sw(\vec{k})} \tag{1.12}$$

Where $\pm$ corresponds to the energy of conduction and valance bands, respectively. The function in Eq.(1.12) is

$$w(\vec{k}) = \sqrt{1 + 4\cos(\frac{3k_x a}{2})\cos\left(\frac{k_y a\sqrt{3}}{2}\right) + 4cos^2(\frac{k_y a\sqrt{3}}{2})} \quad (1.13)$$

Calculated electronic band structure of graphene in the first Brillouin zone is shown on the left plot in Figure 1.5. At high energies, conduction band and valance bands are not degenerate. However, at lower energies near the Dirac points, conduction and valance bands are nearly degenerate and band structure is linear near the Dirac point as shown on the right plot in Figure 1.5. Near the Dirac point, energy of the electrons are linear with wave vector as $\varepsilon_{cv}(k) = \pm vk$ and the electrons have a constant velocity $v = 10^6 m/s$. The velocity of electrons is 1% of the speed of light hence the electrons of graphene mimic as relativistic like Dirac fermions near the $\varepsilon = 0$ regime.

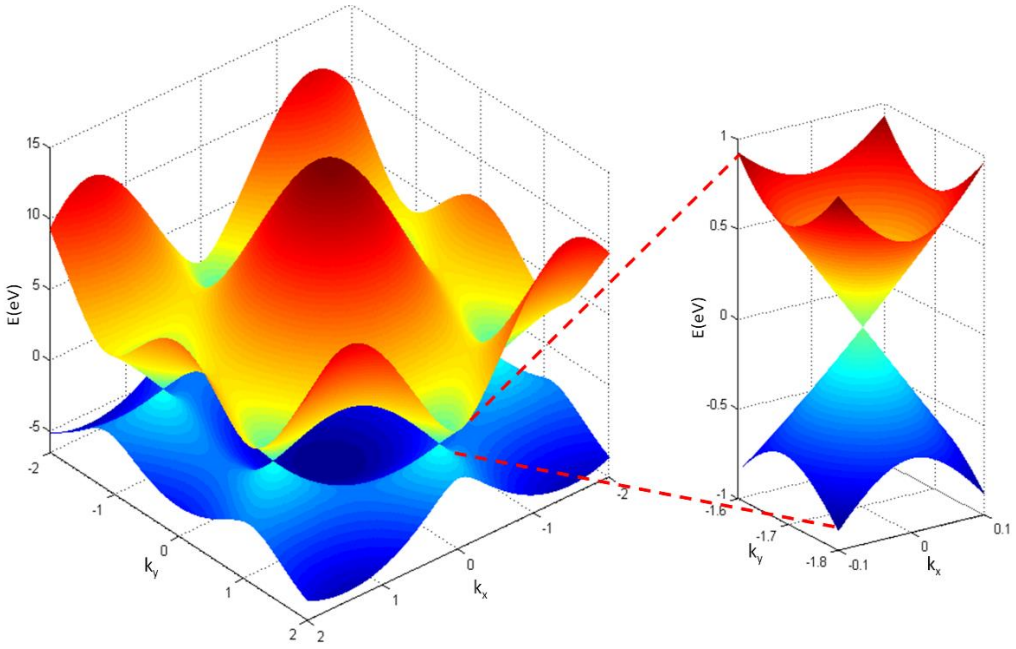

Figure 1.5 Electronic band structure of graphene calculated using the tight binding method. The figure on the left shows the energies of the bands in the first Brillouin zone of graphene. Conduction and valance bands are not symmetric at higher energies but they are symmetric at lower energies near Dirac point as shown in the right plot. Here we used $\varepsilon_{2p} = 0$, $t = -3.033eV$, and $s = 0.129$ for the parameters in Eq.(1.12).

1.2.Optical Conductivity of graphene

Graphene is a zero band gap 2D crystal of carbon atoms arranged in a hexagonal lattice. Its conduction and valance bands meet at Dirac point where the density of states is zero. Away from the Dirac point, the density of states increases and number of allowed energy states increases as well. By chemical or electrostatic doping of graphene, Fermi level of the graphene moves towards or away from the Dirac point. In this way, charge density and conductivity of graphene are tuned. Graphene has a frequency dependent AC (σ_{ac}) conductivity which converges to DC (σ_{dc}) conductivity at low frequencies. To calculate the DC conductivity of graphene in terms of its resistance, we first find the resistance of a 3D conductor. The resistance in 3D can be calculated from the 3D resistivity (ρ_{3D}) of the conductor as

$$R_{3D} = \rho_{3D}\frac{L}{A} = \rho_{3D}\frac{L}{wt} \tag{1.14}$$

Where A is the cross sectional area, w is the width, t is the thickness, L is the length of the conductor. To find the resistance of the conductor in 2D, the 3D resistivity is converted to a 2D resistivity;

$$\rho_{2D} = \frac{\rho_{3D}}{t} \tag{1.15}$$

Where the unit of 3D resistivity is $\Omega.cm$. The unit of the 2D resistivity is Ω, this is actually misinterpreted with a total resistance hence the unit of 2D resistivity is written as Ω/sq. Then the total resistance of the 2D conductor is

$$R_{2D} = \rho_{2D}\frac{L}{w} \tag{1.16}$$

where the unit is in ohm (Ω). For graphene, the resistance is represented mostly with the 2D resistivity as the sheet resistance R_s. The sheet resistance represents the resistance of a square with any dimension. The sheet resistance should be the same for different sizes of graphene sheet with a square dimensions if the graphene sheet

is uniform. Resistivity is the inverse of the conductivity hence the DC conductivity can be expressed as

$$\sigma_{dc} = \frac{1}{\rho_{2D}} = \frac{1}{R_s} \tag{1.17}$$

Graphene has frequency dependent ac conductivity (σ_{ac}) due to both interband and intraband transitions. Interband transitions are the transition of electrons from valance band to conduction band initiated by absorbed energy of a photon. Electrons are Fermions and any of two electrons cannot be at the same energy and momentum state at the same time. An electron can transit from conduction band to valance band if the energy of incident photon is enough. If the corresponding energy level is already filled, then the Pauli blocking does not allow the electron to go that state. Therefore the optical conductivity of graphene strongly depends on the frequency of incident electromagnetic wave. There are number of methods as shown in Ref.[17],[18],[19] to calculate the optical conductivity of graphene due to interband transitions. We follow the method developed by Stauber et.al [19] to calculate the optical conductivity of graphene in visible and near infrared region of the electromagnetic spectrum. The derivation starts with Kubo formula which relates the average surface current density $\langle j_x^D \rangle$, surface area A_s and a current correlation function β;

$$\sigma(\omega) = \frac{\langle j_x^D \rangle}{iA_s(\omega + i0^+)} + \frac{\beta(\omega + i0^+)}{i\hbar A_s(\omega + i0^+)} \tag{1.18}$$

After a long and detailed calculation as given in Ref.[19], the interband conductivity of graphene can be expressed as

$$\sigma^{inter}(\omega) = \frac{e^2}{8\hbar}\left[tanh\left(\frac{\hbar\omega + 2E_f}{4k_bT}\right) + tanh\left(\frac{\hbar\omega - 2E_f}{4k_bT}\right)\right] \tag{1.19}$$

Where E_f is the Fermi energy, k_b is the Boltzmann constant, T is the temperature. It should be noted here that the chemical potential is assumed to be equal to Fermi

energy. And a small contribution to interband conductivity of graphene from the second nearest neighbor atoms in graphene lattice is also neglected.

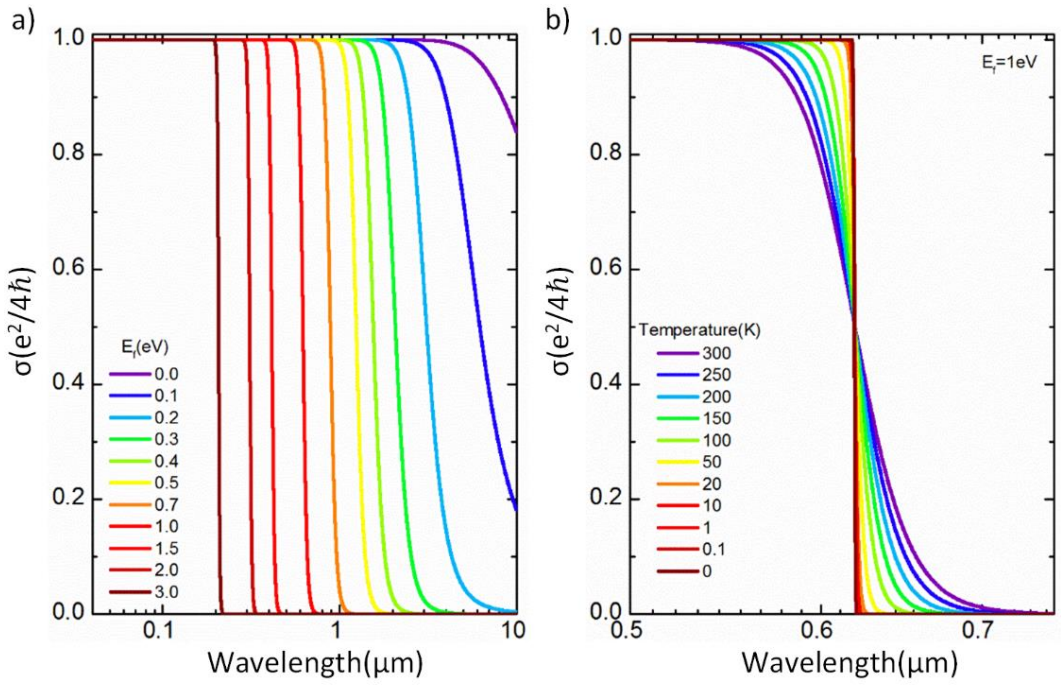

Figure 1.6 Optical conductivity of graphene due to interband transitions with varying Fermi energies (a) and with varying temperatures (b). Graphene has a constant optical conductivity in a broad spectrum when the Fermi energy coincides with Dirac point. If the Fermi energy is shifted up or down to the Dirac point by chemical or electrical doping, optical conductivity of graphene goes down to zero for energies lower than two times the Fermi energy due to Pauli blocking of transitions from valance band to conduction band. Optical conductivity of graphene depends on the temperature. Electrons obey Fermi-Dirac statistics, therefore the behavior of Pauli blocking is sharp at low temperatures. Due to thermal fluctuations, the step function due to Pauli blocking becomes broader as temperature increases.

The first term in Eq.(1.19) can be expressed in terms of the universal conductivity of graphene as[20],[21]

$$\sigma_0(\omega) = \frac{e^2}{4\hbar} = 60.8\mu S \tag{1.20}$$

This is the universal conductivity of an un-doped graphene due to interband transitions, and the conductivity does not depend on any microscopic parameters. As shown in Figure 1.6(a), if the Fermi level of graphene is at the Dirac point, optical conductivity of graphene is constant and corresponds to the universal optical conductivity of $e^2/4\hbar$ in a broad optical spectrum. When the Fermi level of graphene is shifted up or down to the Dirac point, optical transitions between valance and conduction bands are blocked due to the Pauli blocking. Therefore, optical conductivity of graphene goes down to zero for optical energies less than two times the Fermi energy of graphene. Interband conductivity of graphene also depends on the temperature as shown in Figure 1.6(b). At low temperatures, electrons of graphene strongly obey the Fermi-Dirac statistics. Therefore the transition from allowed energy states to the forbidden energy states is sharp at the optical energy that equals to two times the Fermi energy of graphene. At high temperatures, the transition from allowed energy states to the forbidden energy states is not very sharp due to thermal fluctuations.

In order to calculate the ac conductivity of graphene due to the intraband transitions, we follow the calculation performed in [17]. The intraband conductivity of graphene is given by the following equation

$$\sigma^{intra}(\omega) = \frac{e^2\omega}{i\pi\hbar}\int_{-\infty}^{+\infty} d\varepsilon \frac{|\varepsilon|}{\omega^2}\frac{df_0(\varepsilon)}{d\varepsilon} \tag{1.21}$$

Where $f_0(\varepsilon)$is the Fermi-Dirac distribution function given by

$$f_0(\varepsilon) = \left(e^{\frac{(\varepsilon-\mu)}{T}} + 1\right)^{-1} \tag{1.22}$$

Where μ is the chemical potential, T is the temperature. If we integrate (1.21) by inserting $f_0(\varepsilon)$ from (1.22), intraband conductivity can be calculated as

$$\sigma^{intra}(\omega) = \frac{2ie^2T}{\pi\hbar\omega} ln\left[2\cosh\left(\frac{\mu}{2T}\right)\right] \tag{1.23}$$

Electrons in the filled energy states of graphene behave like free electrons similar to electrons in metals, hence, intraband transitions of electrons in graphene can be explained by using the Drude model. It is assumed that an electrons move like a free electron between scattering events in Drude model. The average time between two scatterings of electron is called relaxation time to be τ and the scattering rate is $\Gamma = 1/\tau$. In order to insert scattering rate into Eq.(1.23), the frequency is expressed as $\omega = (\omega + i\Gamma)$, therefore,

$$\sigma^{intra}(\omega) = \frac{2ie^2T}{\pi\hbar(\omega + i\Gamma)} ln\left[2\cosh\left(\frac{\mu}{2T}\right)\right] \tag{1.24}$$

In the Fermi-Dirac statistics, it is assumed that for $\mu \gg T$, the last term in Eq.(1.24) becomes

$$ln\left[2\cosh\left(\frac{\mu}{2T}\right)\right] = \frac{|\mu|}{2T} \tag{1.25}$$

After inserting Eq.(1.25) in to Eq.(1.24), then

$$\sigma^{intra}(\omega) = \frac{ie^2|\mu|}{\pi\hbar(\omega + i\Gamma)} \tag{1.26}$$

If we assume $|\mu| \approx E_f$, then

$$\sigma^{intra}(\omega) = \frac{e^2E_f\tau}{\pi\hbar}\frac{1}{(1 - i\omega\tau)} \tag{1.27}$$

This is the same form of conductivity which is calculated for metals by using the Drude model. AC conductivity of a metal is given as $\sigma(\omega) = \sigma_0/(1 - i\omega\tau)$ where σ_0 is the DC conductivity of the metal. As a result, we can clearly determine that the first term in Eq.(1.27) is the DC conductivity of graphene.

$$\sigma_{DC} = {e^2 E_f \tau}\Big/{\pi\hbar}, \tag{1.28}$$

Then,

$$\sigma^{intra}(\omega) = \frac{\sigma_{DC}}{(1 - i\omega\tau)} \tag{1.29}$$

We have also calculated DC conductivity of graphene by using sheet resistance of graphene in Eq.(1.17). If we insert Eq.(1.17) into Eq.(1.29), then the intraband AC conductivity of graphene can be expressed in terms of DC conductivity as

$$\sigma^{intra}(\omega) = \frac{1}{R_s(1 - i\omega\tau)} \tag{1.30}$$

In addition, we can find a relation between the sheet resistance (R_s) of graphene and its Fermi energy by using Eq.(1.28) and Eq.(1.17) as

$$R_s E_f = \frac{\pi\hbar}{e^2\tau} \approx 0.334\ k\Omega.\, eV \tag{1.31}$$

Where we assume $\tau = 160fs$ which is experimentally measured scattering time of CVD grown graphene [22].

We plot the intraband conductivity of graphene from $1\mu m$ to $1m$ wavelength range in the unit of universal conductivity ($e^2/4\hbar$) of graphene (Figure 1.7). When the Fermi energy of graphene is at the Dirac point, the valance band is completely filled and the conduction band is empty. Therefore, there is no available intraband transition states for electrons to be excited. As a result, the intraband conductivity of graphene is zero for all wavelength for $0eV$ Fermi energies. When the Fermi level is shifted up or down of the Dirac point via electrostatic doping, there are available intraband energy states for electrons to be excited with a small amount of optical energies. When an electron in the conduction band of graphene is excited to an intraband energy state in the same band by a small optical energy, that electron transits to the available states above the Fermi level in the same band and relax back its initial energy level. Similar case happens for holes in the valance band, but in the opposite direction. Intraband conductivity of graphene is zero when $E_f = 0eV$ as

shown in Figure 1.7, however, it increases as the Fermi energy of graphene goes to $E_f = 3eV$. Experimentally accessible the highest Fermi level is $E_f \approx 1eV$ [5].

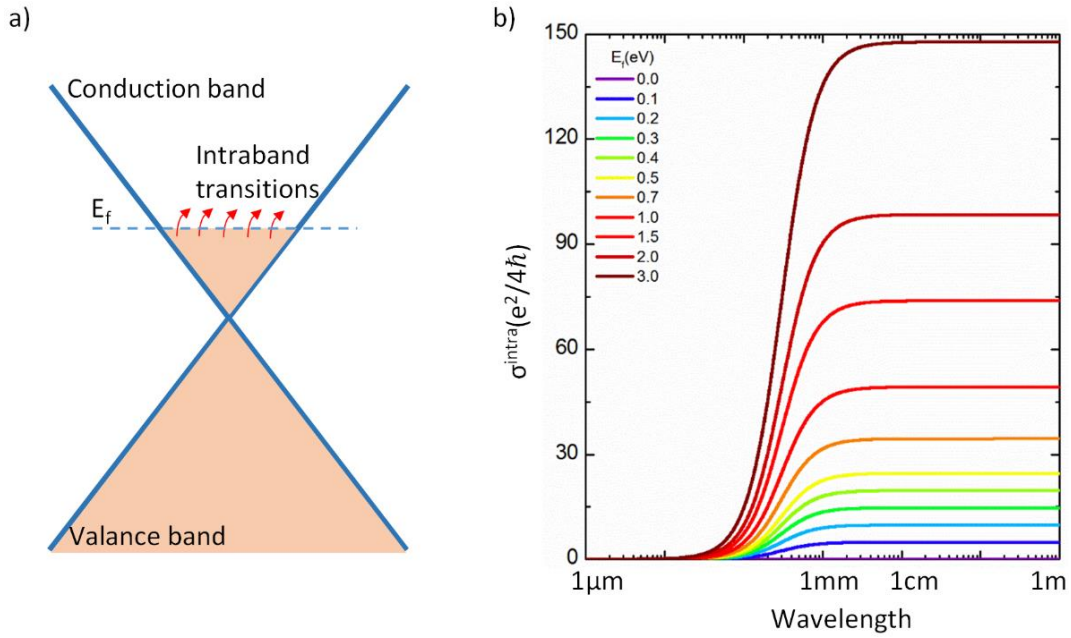

Figure 1.7 Intraband conductivity of graphene for various Fermi level energies of graphene in the unit of universal conductivity of graphene. When Fermi level of graphene is at Dirac point, there is no electron in the conduction and no holes in the valance bands, and therefore, intraband conductivity of graphene is zero. If the Fermi level of graphene is in the conduction or valance band, then there are filled energy levels in graphene and intraband conductivity of graphene is nonzero. Intraband conductivity of graphene increases with an increase in the Fermi energy of graphene.

Total conductivity of graphene is the addition of total interband and intraband conductivities. Each conductivity depends on the Fermi energy of graphene and can be expressed as a function of Fermi energy as in Eq.(1.19) and Eq.(1.27). If we add interband and intraband conductivities of graphene as

$$\sigma(\omega) = \sigma^{inter}(\omega) + \sigma^{intra}(\omega) \tag{1.32}$$

Total conductivity of graphene is plotted in Figure 1.8. In this plot, horizontal axis is the wavelength ranging from 10nm to 1m and vertical axis is the total conductivity of graphene in a unit of universal conductivity $e^2/4\hbar$. Both of the axes are expressed in log-scale. In short wavelengths, total conductivity of graphene is dominated by the interband conductivity of graphene due to the interband transitions. Here the conductivity of graphene is equal to the universal conductivity of graphene. When the Fermi level of graphene is increased, the contribution of interband conductivity to the total conductivity is suppressed up to the corresponding wavelength to two times the Fermi energy of graphene. Here the suppressed energy is expected to be two times the Fermi energy because the suppressed transition is the transition from the conduction band to the valance band and thus required energy is at least two times the Fermi energy. For example; as shown in Figure 1.8, if Fermi energy is $3eV$, interband transition is blocked after $\sim 207nm (\sim 2 * 3eV)$ and if Fermi energy is $1eV$, interband transition is blocked after $\sim 620nm (\sim 2 * 1eV)$. When the interband transition is suppressed due to Pauli blocking, the intraband conductivity starts to dominate. The contribution of intraband conductivity to the total conductivity in the short wavelength region is very low. In the long wavelength region, intraband conductivity is dominant. Its contribution is increasing with increasing Fermi energies opposite to the interband case. When Fermi level is $0eV$ which is practically impossible, there is no intraband contribution to total conductivity of graphene and interband conductivity dominates the whole spectrum. If the Fermi energy is shifted above $0eV$, then the intraband conductivity dominates and goes above the universal conductivity in long wavelength region. For example, if Fermi energy is $1eV$, the

maximum conductivity of graphene is $\sim 49e^2/4\hbar$, if Fermi energy is $3eV$, then the maximum conductivity of graphene is $\sim 147e^2/4\hbar$ (Figure 1.8). Therefore, graphene has much higher intraband conductivity in long wavelength region of electromagnetic spectrum than the interband conductivity in the short wavelength region of electromagnetic spectrum.

High and tunable optical conductivity of graphene in long wavelengths yields new ways of controlling electromagnetic waves. Tunable conductivity results in tunable charge density on graphene and thus boundary conditions for an incident electromagnetic wave can be tuned. To calculate the full optical response of graphene, we have solved Maxwell equations on graphene with appropriate boundary conditions in the following chapter. We calculated transmission, reflection and absorption of single layer graphene in a wide wavelength spectrum by using the previously calculated optical conductivity of graphene in Eq.(1.32).

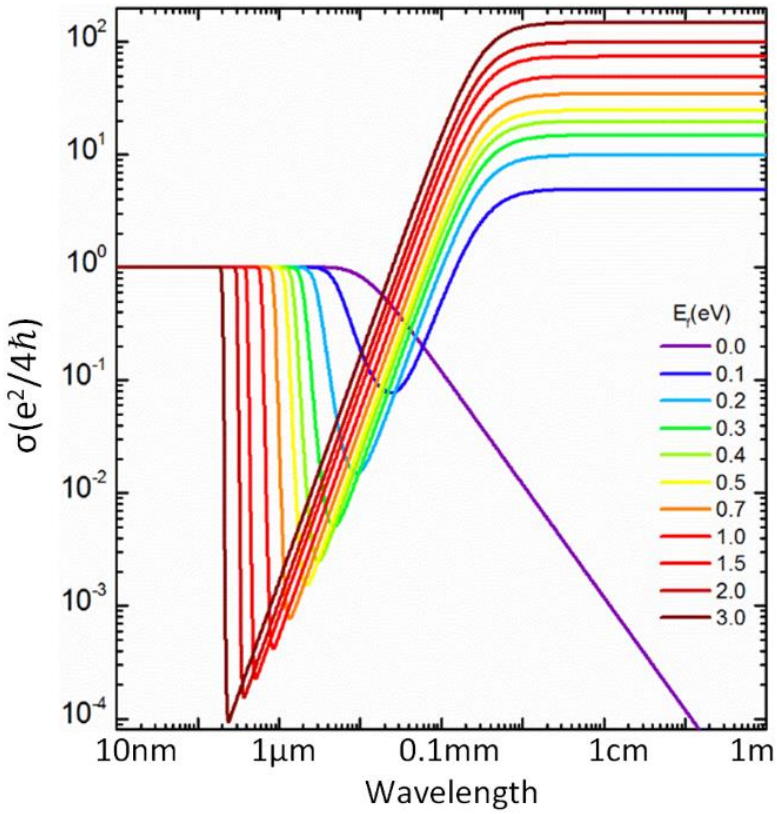

Figure 1.8 Total conductivity of graphene in the unit of universal conductivity $e^2/4\hbar$ for varying Fermi energies in a broad wavelength spectrum ranging from 10nm to 1m. Conductivity of graphene is dominated by the interband conductivity in short wavelengths. Interband contribution can be suppressed even for short wavelengths by increasing the Fermi level of graphene. For longer wavelengths, conductivity of graphene is dominated by the intraband conductivity of graphene. In this case, the intraband conductivity increases with an increase in the Fermi level energy of graphene opposite to the interband case.

Chapter 2

Interaction of light with Graphene

Graphene has a tunable optical conductivity in a large portion of electromagnetic spectrum. Intraband and interband transitions are the two main mechanisms, which drive the interband and intraband optical conductivities of graphene. By electrostatic gating, it is possible to control charge density and Fermi energy. Depending on the energy of the incident electromagnetic wave, electrons in the filled energy bands are excited to empty energy states and relax back. Interband transitions dominate in visible and near-infrared frequencies whereas intraband transitions dominate in mid-, far-infrared, terahertz, and microwave frequencies. During the excitation and relaxation of electrons, an AC current is generated on the graphene surface. Because of Joule heating, this current generates heat on graphene and, therefore, some portion of the incident radiation on graphene is absorbed by graphene. The amount of heat released is proportional to the square of the generated current, resistance, electric field, and time as expressed here as $\theta \sim I^2Rt = (j/A)^2Rt = (\sigma E/A)^2(1/\sigma)t = \sigma(E/A)^2t$. Generated heat is proportional with the conductivity of graphene and, therefore absorption of graphene is proportional to the conductivity of graphene. To calculate absorption of graphene, we will solve Maxwell equations on graphene surface with appropriate boundary conditions. We will use transfer matrix method to

calculate reflection and transmission of electromagnetic waves from graphene surface.

2.1.Transfer matrix method

Graphene is a single layer of carbon atoms and has $\sim 0.34nm$ thickness. The thickness of graphene is very short compared with the wavelength of concerned electromagnetic spectrum that is ranging from visible to microwave. Therefore, we will assume that graphene has a surface charge distribution without any thickness and with an optical conductivity calculated in the previous chapter. Optical response of graphene depends on its charge density thus doping level. When an electromagnetic wave incident on single layer graphene, it is reflected or transmitted or absorbed. The amount of reflected, transmitted, and absorbed intensities depend on the charge density on graphene. In order to calculate full optical response of graphene, we will use transfer matrix method which is developed by Zhan et.al [23]. First, we calculate the optical response of a single layer graphene sandwiched between two mediums, and then we will extend our calculations to two layers of graphene having three different mediums. Finally, we provide optical response of the n-layered graphene structure that divides whole space into n+1 different mediums.

2.1.1.Simulation of single layer graphene

In order to calculate optical response of a single layer graphene sandwiched between two dielectric mediums, Maxwell equations are solved on a graphene-dielectric boundary surface. The schematic of the geometry that is used during calculation is shown in Figure 2.1. A graphene layer with a conductivity of σ is surrounded by two different mediums possessing dielectric constants of ε_1 and ε_2. Graphene is assumed to be a charged layer having no thickness but having an optical conductivity σ as demonstrated in Chapter 1.

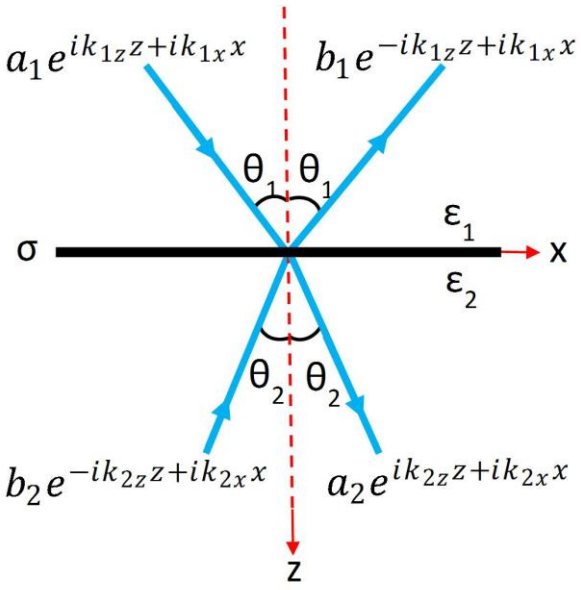

Figure 2.1 Schematic drawing of the geometry used for the calculation of optical response of a single layer graphene. A graphene layer with a conductivity of σ is surrounded by two different mediums having dielectric constants of ε_1 and ε_2. All of the incoming and outgoing electromagnetic waves are considered to have amplitudes of $a_1, a_{2,}\, b_1, b_2$ and angle of incidence of θ_1, θ_2.

In Figure 2.1, electromagnetic waves are incident in xz-plane and propagating in forward ($\hat{\mathbf{x}} + \hat{\mathbf{z}}$) and backward($\hat{\mathbf{x}} - \hat{\mathbf{z}}$) directions in both of these media. We consider both p and s polarizations. For a p polarized wave, magnetic field ($\vec{\mathbf{H}}_{\mathbf{1,2}}$) is along $\hat{\mathbf{y}}$ direction and can be written as

$$\vec{\mathbf{H}}_1^p = \left(a_1 e^{ik_{1z}z+ik_{1x}x} + b_1 e^{-ik_{1z}z+ik_{1x}x}\right)\hat{\mathbf{y}}, \quad z < 0 \tag{2.1}$$

$$\vec{\mathbf{H}}_2^p = \left(a_2 e^{ik_{2z}z+ik_{2x}x} + b_2 e^{-ik_{2z}z+ik_{2x}x}\right)\hat{\mathbf{y}}, \quad z > 0 \tag{2.2}$$

Where $a_{1,2}$ and $b_{1,2}$ are the field coefficients belong to forward and backward propagating waves, respectively. The electric field ($\vec{\mathbf{E}}_{1,2}^p$) can be calculated from $\vec{\mathbf{E}}_{1,2}^p = -v_{1,2}\mu_0(\hat{\mathbf{k}}_{1,2} \times \vec{\mathbf{H}}_{1,2}^p)$ and Eq.(2.1), Eq.(2.2) as

$$\vec{\mathbf{E}}_1^p = \frac{a_1}{\varepsilon_0\varepsilon_1\omega}(k_{1z}\hat{\mathbf{x}} - k_{1x}\hat{\mathbf{z}})e^{ik_{1z}z+ik_{1x}x} - \frac{b_1}{\varepsilon_0\varepsilon_1\omega}(k_{1z}\hat{\mathbf{x}} + k_{1x}\hat{\mathbf{z}})e^{-ik_{1z}z+ik_{1x}x}, \quad z<0 \tag{2.3}$$

$$\vec{\mathbf{E}}_2^p = \frac{a_2}{\varepsilon_0\varepsilon_2\omega}(k_{2z}\hat{\mathbf{x}} - k_{2x}\hat{\mathbf{z}})e^{ik_{2z}z+ik_{2x}x} - \frac{b_2}{\varepsilon_0\varepsilon_2\omega}(k_{2z}\hat{\mathbf{x}} + k_{2x}\hat{\mathbf{z}})e^{-ik_{2z}z+ik_{2x}x}, \quad z<0 \tag{2.4}$$

The boundary conditions for $\vec{\mathbf{H}}_{1,2}^p$ and $\vec{\mathbf{E}}_{1,2}^p$ fields at $z = 0$ are

$$\hat{\mathbf{n}} \times \left(\vec{\mathbf{H}}_2^p - \vec{\mathbf{H}}_1^p\right)\Big|_{Z=0} = \vec{\mathbf{J}} \tag{2.5}$$

$$\hat{\mathbf{n}} \times \left(\vec{\mathbf{E}}_2^p - \vec{\mathbf{E}}_1^p\right)\Big|_{Z=0} = 0 \tag{2.6}$$

Where $\hat{\mathbf{n}} = \hat{\mathbf{z}}$ is the surface normal and $\vec{\mathbf{J}}$ is the surface current density. If we apply these boundary conditions to the fields in Eq.(2.1), Eq.(2.2), Eq.(2.3) and Eq.(2.4), then

$$\frac{k_{2z}}{\varepsilon_2}(a_2 - b_2) - \frac{k_{1z}}{\varepsilon_1}(a_1 - b_1) = 0 \tag{2.7}$$

$$(a_1 + b_1) - (a_2 + b_2) = J = \sigma E_{2x}|_{z=0} = \frac{\sigma k_{2z}}{\varepsilon_0\varepsilon_2\omega}(a_2 - b_2) \tag{2.8}$$

By combining these two equations, we can find a transmission matrix D_{12}^p of incident p-polarized electromagnetic wave from a single layer of graphene between medium-1 and medium-2 by solving the following equation for D_{12}^p

$$\begin{bmatrix} a_1 \\ b_1 \end{bmatrix} = D_{12}^p \begin{bmatrix} a_2 \\ b_2 \end{bmatrix} \tag{2.9}$$

Where

$$D_{12}^p = \frac{1}{2}\begin{bmatrix} 1 + \alpha_{12}^p + \beta_{12}^p & 1 - \alpha_{12}^p - \beta_{12}^p \\ 1 - \alpha_{12}^p + \beta_{12}^p & 1 + \alpha_{12}^p - \beta_{12}^p \end{bmatrix} \tag{2.10}$$

Where

$$\alpha_{12}^p = \frac{\varepsilon_1 k_{2z}}{\varepsilon_2 k_{1z}} \quad , \qquad \beta_{12}^p = \frac{\sigma k_{2z}}{\varepsilon_0\varepsilon_2\omega} \tag{2.11}$$

For s-polarization, electric field is in $\hat{\mathbf{y}}$ direction as shown in Figure 2.5 and can be expressed as

$$\vec{\mathbf{E}}_1^s = \left(a_1 e^{ik_{1z}z+ik_{1x}x} + b_1 e^{-ik_{1z}z+ik_{1x}x}\right)\hat{\mathbf{y}}, \quad z < 0 \tag{2.12}$$

$$\vec{\mathbf{E}}_2^s = \left(a_2 e^{ik_{2z}z+ik_{2x}x} + b_2 e^{-ik_{2z}z+ik_{2x}x}\right)\hat{\mathbf{y}}, \quad z > 0 \tag{2.13}$$

Magnetic field can be calculated from $\vec{\mathbf{H}}_{1,2}^s = \frac{1}{v_{1,2}\mu_0}(\hat{\mathbf{k}}_{1,2} \times \vec{\mathbf{E}}_{1,2}^s)$ and Eq.(2.12), Eq.(2.13) as

$$\vec{\mathbf{H}}_1^s = \frac{a_1}{\mu_0\omega}(-k_{1z}\hat{\mathbf{x}} + k_{1x}\hat{\mathbf{z}})e^{ik_{1z}z+ik_{1x}x} + \frac{b_1}{\mu_0\omega}(k_{1z}\hat{\mathbf{x}} + k_{1x}\hat{\mathbf{z}})e^{-ik_{1z}z+ik_{1x}x}, \quad z < 0 \tag{2.14}$$

$$\vec{\mathbf{H}}_2^s = \frac{a_2}{\mu_0\omega}(-k_{2z}\hat{\mathbf{x}} + k_{2x}\hat{\mathbf{z}})e^{ik_{2z}z+ik_{2x}x} + \frac{b_2}{\mu_0\omega}(k_{2z}\hat{\mathbf{x}} + k_{2x}\hat{\mathbf{z}})e^{-ik_{2z}z+ik_{2x}x}, \quad z > 0 \tag{2.15}$$

If we apply boundary conditions from Eq.(2.5) and Eq.(2.6) to the fields in Eq.(2.12), Eq.(2.13), Eq.(2.14) and Eq.(2.15), we find that

$$(a_1 + b_1) - (a_2 + b_2) = 0, \tag{2.16}$$

$$\frac{k_{2z}}{\mu\omega}(b_2 - a_2) - \frac{k_{1z}}{\mu\omega}(b_1 - a_1) = J = \sigma E_{2y}\big|_{z=0} = \sigma(a_2 + b_2) \tag{2.17}$$

The transmission matrix for s-polarization D_{12}^s can be calculated by solving the following equation for D_{12}^s

$$\begin{bmatrix} a_1 \\ b_1 \end{bmatrix} = D_{12}^s \begin{bmatrix} a_2 \\ b_2 \end{bmatrix} \tag{2.18}$$

Where

$$D_{12}^s = \frac{1}{2}\begin{bmatrix} 1 + \alpha_{12}^s + \beta_{12}^s & 1 - \alpha_{12}^s + \beta_{12}^s \\ 1 - \alpha_{12}^s - \beta_{12}^s & 1 + \alpha_{12}^s - \beta_{12}^s \end{bmatrix} \tag{2.19}$$

Where

$$\alpha_{12}^{s} = \frac{k_{2z}}{k_{1z}} \quad , \quad \beta_{12}^{s} = \frac{\sigma\mu_0\omega}{k_{1z}} \tag{2.20}$$

So far, we only consider the interaction between a single layer of graphene surrounded by two different dielectric media and an incident electromagnetic wave. Therefore the transfer matrix is equal to the transmission matrix.

$$M_{1-layer}^{s,p} = D_{12}^{s,p} \tag{2.21}$$

The reflection ($r_{1-layer}^{s,p}$) and transmission ($t_{1-layer}^{s,p}$) coefficients for a single layer graphene can be calculated from the elements of transfer matrix $M_{1-layer}^{s,p}$ as

$$r_{1-layer}^{s,p} = \frac{M_{1-layer}^{s,p}(2,1)}{M_{1-layer}^{s,p}(1,1)} \tag{2.22}$$

$$t_{1-layer}^{s,p} = \frac{1}{M_{1-layer}^{s,p}(1,1)} \tag{2.23}$$

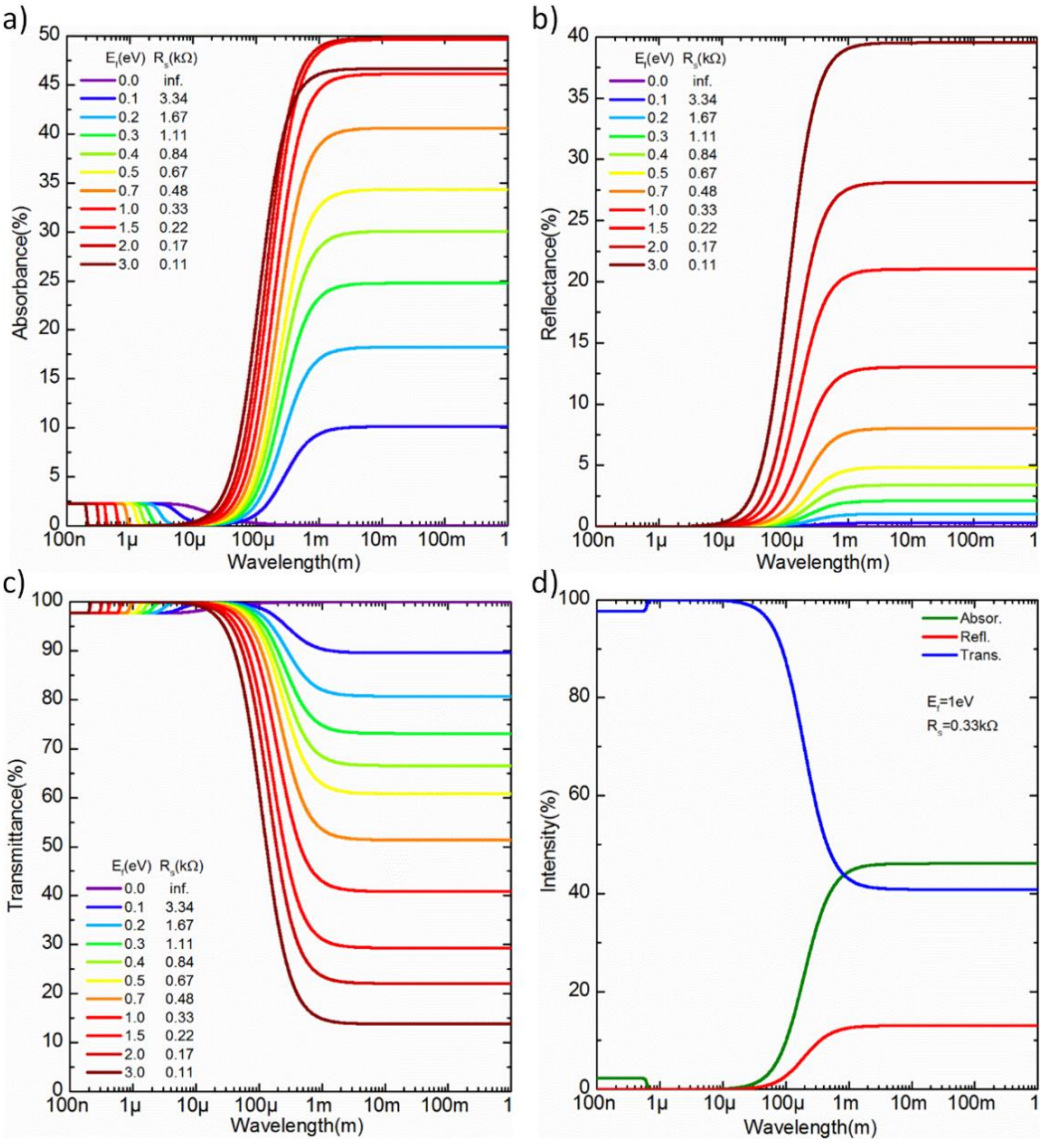

Figure 2.2 Calculated optical response of a single layer graphene in a broad wavelength range is demonstrated. Absorbance (a) of graphene depends on the incident wavelength. The maximum absorbance of a single layer graphene is $\sim\%2.24$ in the visible, and $\%50$ in the microwave. Absorbance of graphene varies with the Fermi energy of graphene. Reflectance (b) and transmittance (c) of graphene are due to the interband and intraband conductivity of graphene and it can be tuned by tuning the Fermi level of graphene. Absorbance, reflectance, and transmittance of graphene with a Fermi energy of $1eV$ is shown in (d).

By inserting transmission and reflection coefficients in Eq.(2.22) and Eq.(2.23), transmittance, reflectance, and absorbance of a single layer graphene can be calculated for an incident radiation by using the following equations

$$T^{s}_{1-layer} = \frac{k_{2z}}{k_{1z}} \left| t^{s}_{1-layer} \right|^{2} \tag{2.24}$$

$$T^{p}_{1-layer} = \frac{\varepsilon_1 k_{2z}}{\varepsilon_2 k_{1z}} \left| t^{p}_{1-layer} \right|^{2} \tag{2.25}$$

$$R^{s,p}_{1-layer} = \left| r^{s,p}_{1-layer} \right|^{2} \tag{2.26}$$

$$A^{s,p}_{1-layer} = 1 - T^{s,p}_{1-layer} - R^{s,p}_{1-layer} \tag{2.27}$$

For high energy of incident radiation such as in the ultraviolet, visible or near-infrared portion of electromagnetic spectrum, interband transitions between the valance and conduction bands of graphene drive the optical response of graphene. When electromagnetic radiation is incident on graphene, an electron from the conduction band absorbs energy of the incident radiation and it is excited to an available and allowed energy state in the conduction band. Subsequently, the excited electron falls back to the conduction band of the graphene by emitting energy. During the process of excitation and relaxation of an electron, a universally constant amount ($\sim\%2.24$) of incident radiation is absorbed due to the universal conductivity of graphene thanks to interband transitions. If there is no empty or allowed energy states available in the graphene conduction band, then the incident electromagnetic radiation pass through graphene without any absorption. When empty energy levels are filled, allowed interband transitions are blocked by Pauli Blocking and graphene is not further absorbing the energies below two times the Fermi energy. Pauli blocking is not sharp due to the thermal fluctuations in Fermi-Dirac distributions at high temperatures as shown in Figure 2.2(a).

The calculated absorbance, reflectance and transmittance values are plotted in Figure 2.2 for a broad optical spectrum ranging from $100nm$ to $1m$. In the UV, visible, and near-infrared part of the electromagnetic spectrum, absorbance of graphene is constant and reaches a value of around $\%2.24$ because of the universal optical conductivity of graphene (Figure 2.2). It should be emphasized here that the excitonic contributions to conductivity and absorbance of graphene are not considered for this calculation. Graphene is reflecting small amount of the incident radiation due to interband transitions, and it is absorbing or transmitting most of the incident electromagnetic radiation. When graphene is absorbing $\sim\%2.24$, its transmission is $\sim\%97.75$. When graphene is not absorbing, it is transmitting almost all of the incident radiation as shown in Figure 2.2(d). Thus, measuring transmission of a single layer graphene also gives the absorption of graphene in the UV, visible and near infrared region of electromagnetic spectrum on the condition that the excitonic contributions are neglected.

For low energies from mid-infrared to microwave portion of the electromagnetic spectrum, intraband transitions through the conduction and valance band drive the optical response of graphene. Low energy radiation excites the electrons in the conduction band and holes in valance band near the Fermi level and excite these electrons and holes to higher energy states. Afterwards, these excited electrons and holes relax back to the original energy state. Concurrently, some amount of current is generated on the surface of the graphene and hence some amount of the incident radiation is absorbed due to Joule heating as discussed in previous sections. If the Fermi level is near to the Dirac point of graphene than the number of available energy states is low hence absorption of graphene is low. By shifting the Fermi level of graphene far from the Dirac point, it is possible to increase optical response of graphene. Therefore, active control of Fermi level of graphene enables to control the optical response of graphene actively in the terahertz and microwave frequencies.

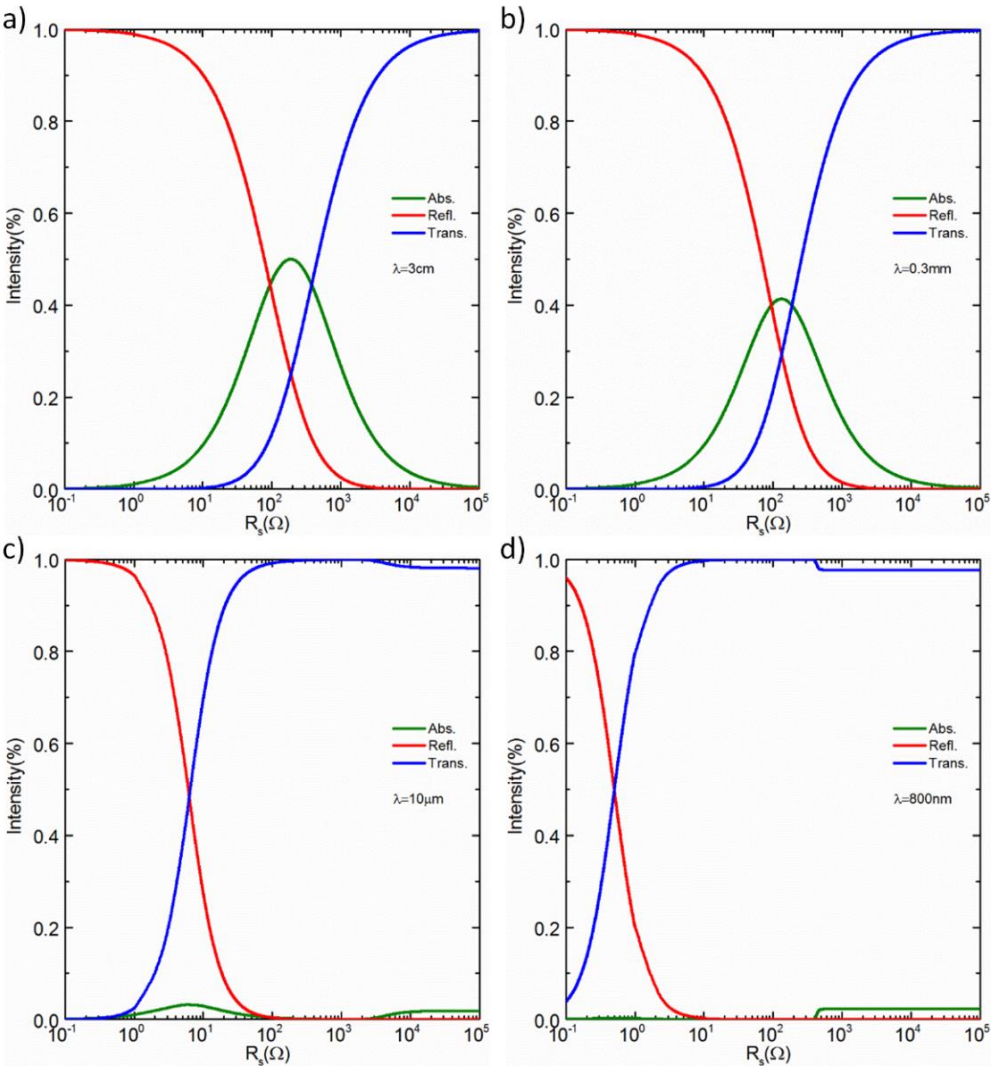

Figure 2.3 Absorbance (green), reflectance (red), and transmittance (blue) of a single layer graphene as a function of sheet resistance (R_s) are shown. The wavelength of the incident electromagnetic radiations is $3cm$(a), $0.3mm$(b), $10\mu m$(c), and $800nm$(d). In the microwave region, the maximum absorbance (%50) can be achieved when the impedance of single layer graphene is matched to half of the free space impedance, i.e. 186.5Ω (a). For the terahertz (b) and infrared (c) regions of electromagnetic spectrum, both the maximum absorbance and the required impedance are decreasing. In the visible spectrum, graphene absorbs $\sim 2.24\%$ for electromagnetic energies above two times the Fermi energy of graphene.

Absorbance, reflectance and transmittance of graphene can be tuned with varying sheet resistance and Fermi energy (Figure 2.2, Figure 2.3). Increasing the Femi energy of graphene by doping, conductivity of graphene always increases in microwave region of electromagnetic spectrum. However, the absorption of graphene does not always increase with increasing Fermi energy. In microwave region, free standing graphene can absorb at most 50% of the incident radiation when the impedance of graphene is matched with the half of free space impedance, i.e. 188.5Ω (Figure 2.2(a), Figure 2.3). If the impedance or sheet resistance of graphene exceeds or falls behind half of the free space impedance, the absorption of graphene decreases. Microwave is a low frequency regime and hence impedance of both free space and graphene are pure real and same with the DC impedance. However, impedance of both graphene and the free space has complex contributions in terahertz and infrared frequencies. Therefore the maximum absorbance of single layer graphene and the required impedance are decreasing as the frequency of incident radiation approaches to terahertz and far infrared frequencies. The calculated maximum absorbance is 41.3% and the required impedance is 132Ω for the wavelength of $0.3mm$ (Figure 2.3(b)). For 6.3Ω, the maximum absorbance is $\%3.2$ (Figure 2.3(c)).

Absorption of graphene is calculated by subtracting the reflection and transmission amplitudes from the total incident radiation. Similar to absorption amplitude, both reflection and the transmission amplitudes can be tuned by varying the Fermi energy of graphene. For instance, graphene is absorbing $\%46$, reflecting $\%13$ and transmitting $\%41$ of the incident radiation at $1eV$ Fermi energy at $1cm$ wavelength (Figure 2.2(d)).

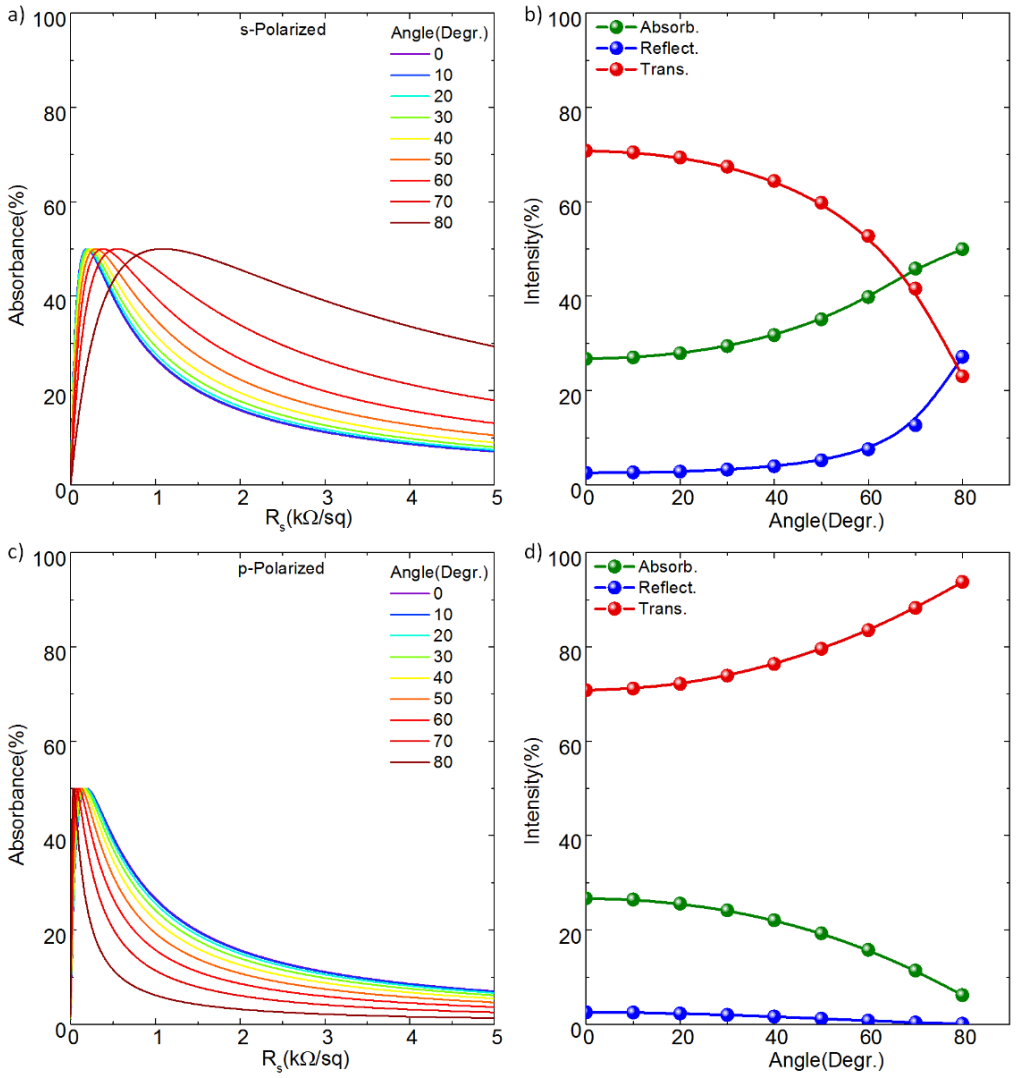

Figure 2.4 Calculated optical response of single layer graphene for various angle of incidences with the wavelength of $3cm$. (a) Absorbance as a function of sheet resistance of graphene is shown for s-polarized incident radiation. Colored lines specify the different angle of incidences. (b) Absorbance, reflectance and transmittance of one layer graphene as a function of incident angle for s-polarized radiation at the sheet resistance of $1k\Omega$ are designated. (c) Absorbance of p-polarized radiation with a wavelength of $3cm$ as a function of sheet resistance of graphene for various incidence angles is shown. (d) Absorbance, reflectance and transmittance of graphene at $1k\Omega$ sheet resistance as a function of angle is displayed.

Figure 2.4 shows the calculated optical parameters of a single layer graphene for both s- and p-polarized incident radiations. Free standing graphene can absorb at most $\%50$ when the sheet resistance of graphene equals to the half of the free space impedance, i.e. 377Ω. At this critical sheet resistance of graphene, absorbance at $3cm$ wavelength is the maximum value for the normal incidence of the incoming radiation. As the angle of incidence is varied from 0^o to 80^o, the sheet resistance value at which the absorbance reaches its maximum value shifts to higher values for s-polarized radiation (Figure 2.4(a)). However, the shift goes towards smaller sheet resistance values for a p-polarized radiation as the angle of incidence increases (Figure 2.4(d)). Incident radiation experiences higher surface impedance values for s-polarized wave and smaller impedance values for p-polarized wave as the angle of incidence increases. We calculated absorbance, reflectance, and transmittance values from a single layer graphene for s- and p-polarized wave (Figure 2.4(b), Figure 2.4(d)).

2.1.2.Simulation of two layer graphene stack

For two layers of graphene, there are three mediums with permittivity of ε_1, ε_2 and ε_3 as shown in Figure 2.5. The distance between the two graphene layers is L_2. The transmission matrix of the first graphene layer is $D_{12}^{s,p}$ which is calculated in the previous section. In addition, the propagation matrix for the propagated wave in medium-2 is needed to be calculated. Propagation along a distance L_2 in $\hat{\mathbf{z}}$ direction is calculated by the propagation matrix $P_2(L_2)$ which is given by

$$P_2(L_2) = \begin{bmatrix} e^{-ik_z L_2} & 0 \\ 0 & e^{ik_z L_2} \end{bmatrix} \tag{2.28}$$

The transmission matrix for the second graphene layer for p- and s-polarization can be calculated similar to the first graphene layer as shown in Eq.(2.19) as

$$D_{23}^{p} = \frac{1}{2}\begin{bmatrix} 1+\alpha_{23}^{p}+\beta_{23}^{p} & 1-\alpha_{23}^{p}-\beta_{23}^{p} \\ 1-\alpha_{23}^{p}+\beta_{23}^{p} & 1+\alpha_{23}^{p}-\beta_{23}^{p} \end{bmatrix} \tag{2.29}$$

Where

$$\alpha_{23}^{p} = \frac{\varepsilon_2 k_{3z}}{\varepsilon_3 k_{2z}}, \quad \beta_{23}^{p} = \frac{\sigma k_{3z}}{\varepsilon_0 \varepsilon_3 \omega} \tag{2.30}$$

And

$$D_{23}^{s} = \frac{1}{2}\begin{bmatrix} 1 + \alpha_{23}^{s} + \beta_{23}^{s} & 1 - \alpha_{23}^{s} + \beta_{23}^{s} \\ 1 - \alpha_{23}^{s} - \beta_{23}^{s} & 1 + \alpha_{23}^{s} - \beta_{23}^{s} \end{bmatrix} \tag{2.31}$$

Where

$$\alpha_{23}^{s} = \frac{k_{3z}}{k_{2z}}, \qquad \beta_{23}^{s} = \frac{\sigma \mu_0 \omega}{k_{2z}} \tag{2.32}$$

The transfer matrix for the 2-layer graphene $M_{2-layer}^{s,p}$ is calculated by multiplying the transmission matrix of the first graphene D_{12}^{s}, the propagation matrix in medium-2 $P_2(L_2)$ and the transmission matrix of the second graphene layer $M_{2-layer}^{s,p}$ as

$$M_{2-layer}^{s,p} = D_{12}^{s,p} P_2(L_2) D_{23}^{s,p} \tag{2.33}$$

Moreover, the transmission and reflection coefficients are calculated from indices of the transfer matrix from Eq.(2.33) as

$$r_{2-layer}^{s,p} = \frac{M_{2-layer}^{s,p}(2,1)}{M_{2-layer}^{s,p}(1,1)} \tag{2.34}$$

$$t_{2-layer}^{s,p} = \frac{1}{M_{2-layer}^{s,p}(1,1)} \tag{2.35}$$

The transmittance, reflectance, and absorbance of 2-layer graphene for both s- and p-polarizations are calculated from Eq.(2.34) and Eq.(2.35) as

$$T_{2-layer}^{s} = \frac{k_{3z}}{k_{2z}} \left| t_{2-layer}^{s} \right|^2 \tag{2.36}$$

$$T_{2-layer}^{p} = \frac{\varepsilon_2 k_{3z}}{\varepsilon_3 k_{2z}} \left| t_{2-layer}^{p} \right|^2 \tag{2.37}$$

$$R_{2-layer}^{s,p} = \left| r_{2-layer}^{s,p} \right|^2 \tag{2.38}$$

$$A_{2-layer}^{s,p} = 1 - T_{2-layer}^{s,p} - R_{2-layer}^{s,p} \tag{2.39}$$

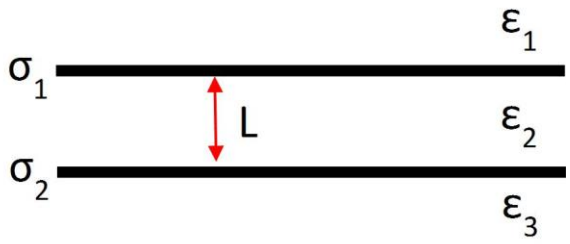

Figure 2.5 Schematic drawing of a single layer graphene in two different layers is shown. There are three different dielectric mediums possessing dielectric constants of $\varepsilon_1, \varepsilon_2, \varepsilon_3$. Two different graphene layers are between these three mediums. Second medium is between two layers of graphene and has a thickness of L_2.

Two stacks of free standing graphene layers are simulated, and these two graphene layers are separated by air with a thickness of $50\mu m$ as indicated in Figure 2.5. Two graphene layers are assumed to be identical and ideal without an unintentional doping. We calculate optical absorbance spectrum of two stacks of graphene layers (Figure 2.6(a)) for varying Fermi energies of graphene layers from $0eV$ to $3eV$. Varying Fermi energy of graphene layers tunes the absorbance of graphene below $\%50$ in microwave. However, absorbance of graphene can go over $\%75$ in terahertz region due to Fabry-Perot resonance between two graphene layers. Transmittance and reflectance spectrum of the two graphene structure have some resonance peaks and deeps in the far infrared and terahertz region as shown in Figure 2.6(b). Shifting the Fermi energy of each graphene layer modulates the absorbance, transmittance and reflectance of two graphene layers structure for the wavelength of $3cm$ (Figure 2.6(c)) and $0.3mm$ (Figure 2.6(d)).

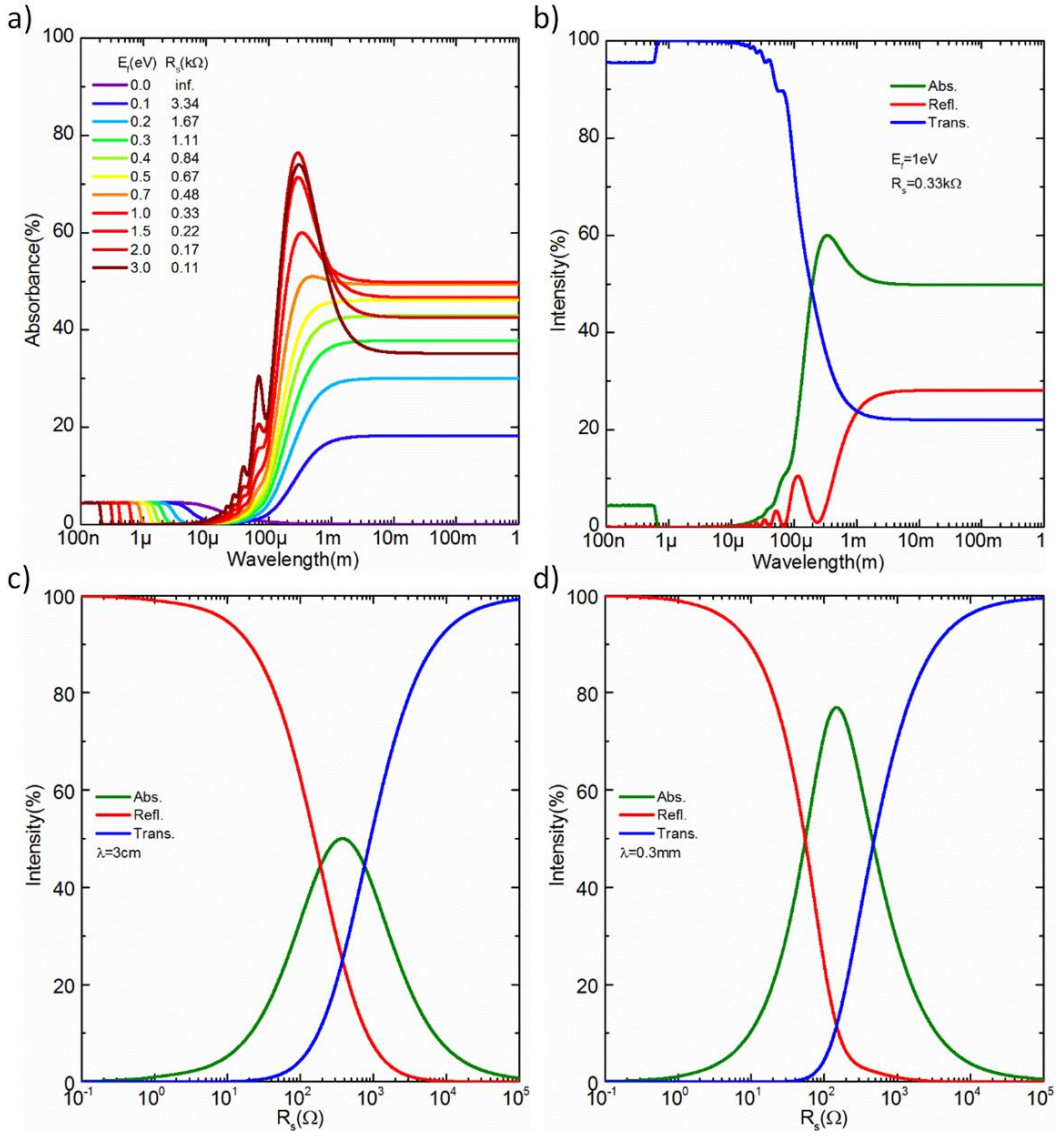

Figure 2.6 Simulated optical response of two stacks of graphene layers. The distance between two graphene layers is assumed to be $50\mu m$ and they are assumed to be in the free space. Due to the separation between two graphene layers, there are Fabry-Perot resonance peaks in the absorbance spectrum and absorbance goes over $\%70$ in the THz frequencies (a, b). Varying the sheet resistance of graphene layers tunes the absorbance, reflectance, and transmittance of two graphene layers for the wavelength of $3cm$ (c) and $0.3mm$ (d). The calculated maximum absorbance value in this condition is still $\%50$ in the microwave region.

2.1.3.Simulation of multiple graphene layers stack

To generalize transfer matrix calculation of graphene layers, we calculated optical response of single layer graphene in an *n*-layer structure. There are *n* layers of graphene between *n+1* mediums. The transmission matrix for i^{th} layer of graphene is $D_{i\,i+1}^{s,p}$ and the propagation matrix in the i^{th} media is $P_i(L_i)$ where L_i is the thickness of i^{th} layer. We calculated the transfer matrix for the *n*-layer of graphene by multiplying each transmission and propagation matrices in order as

$$M_{1-layer}^{s,p} = D_{12}^{s,p} \tag{2.40}$$

$$M_{2-layer}^{s,p} = D_{12}^{s,p} P_2 D_{23}^{s,p} \tag{2.41}$$

$$M_{3-layer}^{s,p} = D_{12}^{s,p} P_2 D_{23}^{s,p} P_3 D_{34}^{s,p} \tag{2.42}$$

$$M_{4-layer}^{s,p} = D_{12}^{s,p} P_2 D_{23}^{s,p} P_3 D_{34}^{s,p} P_4 D_{45}^{s,p} \tag{2.43}$$

$$M_{5-layer}^{s,p} = D_{12}^{s,p} P_2 D_{23}^{s,p} P_3 D_{34}^{s,p} P_4 D_{45}^{s,p} P_5 D_{56}^{s,p} \tag{2.44}$$

$$M_{n-layer}^{s,p} = D_{12}^{s,p} P_2 D_{23}^{s,p} \dots\dots\dots\dots\dots\dots P_n D_{nn+1}^{s,p} \tag{2.45}$$

$$\tag{2.46}$$

As calculated for single and two layer graphene structures in Eq.(2.22), Eq.(2.23) and Eq.(2.34), Eq.(2.35), the transmission and reflection coefficients are calculated from the transfer matrix elements as

$$r_{n-layer}^{s,p} = \frac{M_{n-layer}^{s,p}(2,1)}{M_{n-layer}^{s,p}(1,1)} \tag{2.47}$$

$$t_{n-layer}^{s,p} = \frac{1}{M_{n-layer}^{s,p}(1,1)} \tag{2.48}$$

The transmittance, reflectance and absorbance of incident radiation on multi-layer graphene structure are calculated as

$$T_{n-layer}^{s} = \frac{k_{n+1z}}{k_{nz}} \left| t_{n-layer}^{s} \right|^2 \tag{2.49}$$

$$T_{n-layer}^{p} = \frac{\varepsilon_n k_{n+1z}}{\varepsilon_{n+1} k_{nz}} \left| t_{n-layer}^{p} \right|^2 \tag{2.50}$$

$$R_{n-layer}^{s,p} = \left| r_{n-layer}^{s,p} \right|^2 \tag{2.51}$$

$$A_{n-layer}^{s,p} = 1 - T_{n-layer}^{s,p} - R_{n-layer}^{s,p} \tag{2.52}$$

Optical response of 10 stacks of graphene layers is shown in Figure 2.7. The calculated absorbance, reflectance, and transmittance of 10 stacks of graphene layers are potted by using Eq.(2.50), Eq.(2.51) and Eq.(2.52). It is noteworthy to indicate here that all graphene layers are assumed to be identical and they are separated with the free space with a thickness of $50\mu m$. A Fabry-Perot resonance absorbance peaks appear in the broad absorbance spectrum of 10 stacks of graphene layers due to the free space thickness as shown in Figure 2.7(a). Optical response of 10 stacks of graphene depends on the wavelength of the incident radiation thanks to the interband and intraband conductivity of each graphene layer as shown in Figure 2.7(b). Varying the Fermi energy of each graphene layer tunes the absorbance, reflectance, and transmittance of graphene layers in the microwave and terahertz frequencies (Figure 2.7(c, d)).

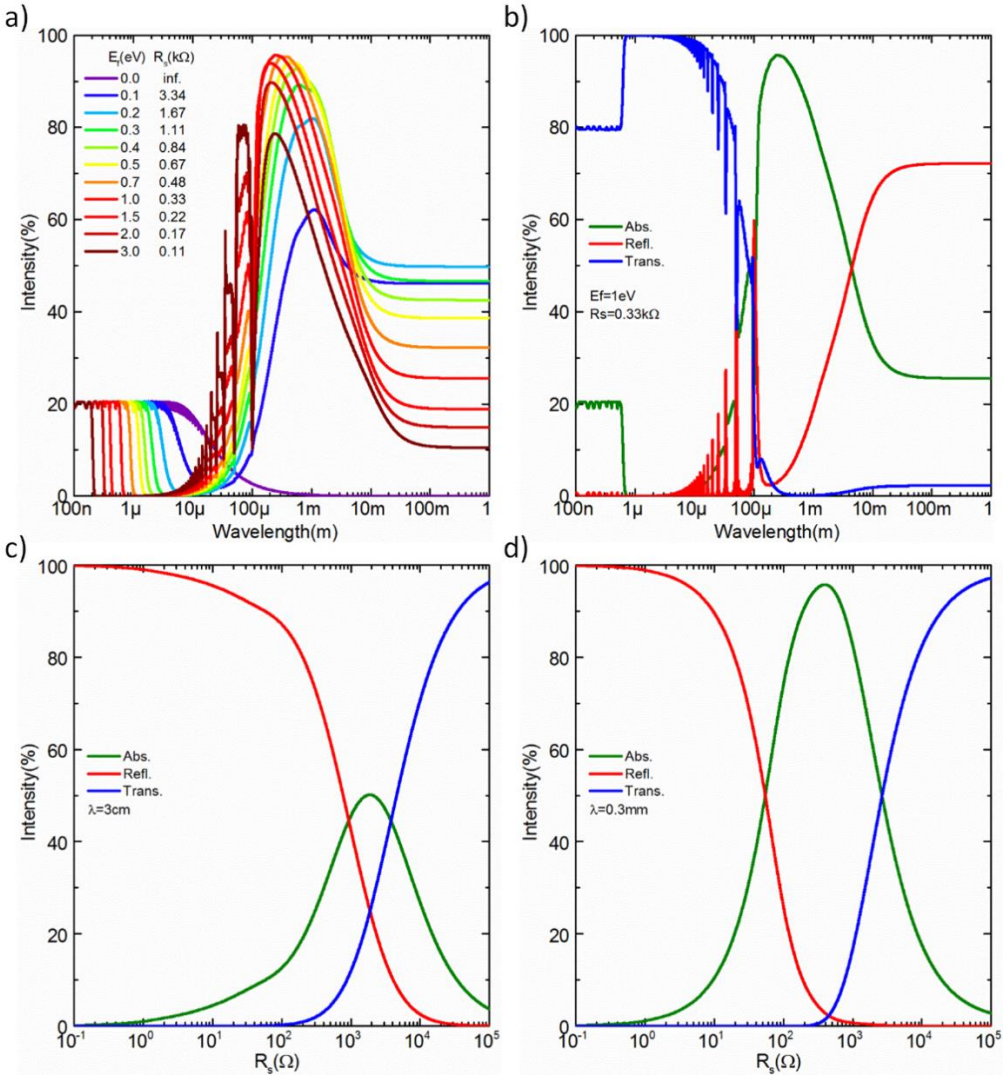

Figure 2.7 Simulated optical response of 10 stacks of graphene layers is shown. All graphene layers are assumed to be identical and they are separated with a distance of $50\mu m$. They are all assumed to be in the free space. Absorbance spectrum of 10 graphene stacks is shown in (a) for varying Fermi energies. Absorbance, transmittance, and reflectance spectra are shown in (b) for $1eV$ Fermi energy from $10nm$ to $1m$. Varying the sheet resistance of graphene layers tunes the optical response of the 10 stacks of graphene layers in the microwave frequencies with the wavelength of $3cm$ as shown in (c) and for terahertz frequencies with the wavelength of $0.3mm$ as shown in (d)

2.2.Transmission line model

Transmission line model has been used to understand the microwave absorption of ultrathin conducting films. Here we implemented the same model for graphene surfaces. Calculations for the model is followed from the article written by Bosman et.al in [24]. The microwave reflectivity R, from a surface is proportional with the mismatch between the characteristic impedance of air and the surface impedance and can be written as

$$R = \frac{Z_R - 1}{Z_R + 1} \tag{2.53}$$

And transmission is given as

$$T = (1 + R)\cos(kL) - i(Z/Z_0)(1 - R)\sin(kL) \tag{2.54}$$

Where

$$Z_R = \frac{1 + i(Z/Z_0)\tan(kL)}{1 + i(Z_0/Z)\tan(kL)} \tag{2.55}$$

Where $Z_0 = \sqrt{\mu_0/\varepsilon_0} = 377\Omega$ is the free space impedance and Z is the characteristic impedance of the thin film and given as

$$Z = \sqrt{\frac{\mu_0}{\varepsilon + \frac{\sigma}{i\omega}}} \tag{2.56}$$

And k is the complex wavenumber and given as

$$k = \omega\sqrt{\mu_0(\varepsilon + \frac{\sigma}{i\omega})} \tag{2.57}$$

Where ω is the frequency, ε is dielectric constant, μ_0 is permeability of free space, ε_0 is the permittivity of free space, and σ is the bulk conductivity of graphene layer. Bulk conductivity σ is inversely proportional with the sheet resistance of graphene layer as $\sigma = 1/R_s$. We plot optical response (absorbance, reflectance, and

transmittance) of single layer graphene for a normal incidence with transmission line model in Figure 2.8. Calculated results are the same as with the results obtained by transfer matrix method in Figure 2.2 and Figure 2.3.

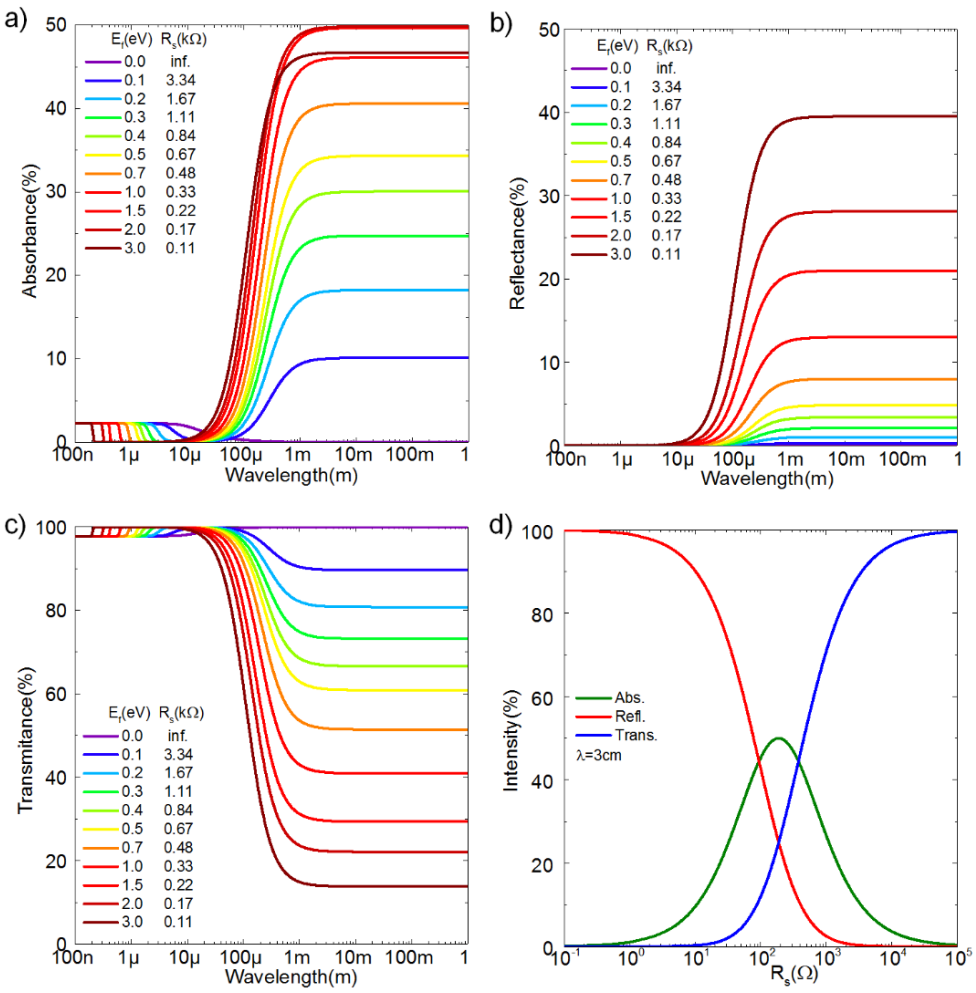

Figure 2.8 Optical response of a single layer graphene calculated with transmission line model for normal incidence. Absorbance (a), reflectance (b) and transmittance (c) as a function of incident wavelength for various Fermi energies are plotted. Absorbance (green), reflectance (red), and transmittance (blue) as a function of sheet resistance of single layer graphene for the incident wavelength of $3cm$ are shown in (d).

2.3.Simulation of graphene supercapacitor

In order to simulate optical response of graphene supercapacitors we have used transfer matrix method, i.e. extensively discussed for single and multi-stacks of graphene layers in previous sections. In the previous calculations, graphene layers are assumed to be standing in the free space. However, graphene needs a substrate and each substrate has frequency dependent optical response. Therefore, optical response of each different layers is needed to be calculated in the simulation. Graphene supercapacitor is constructed with 5-layers having a frequency dependent dielectric constants of $\varepsilon_1, \varepsilon_2, \varepsilon_3, \varepsilon_4, \varepsilon_5$ as shown in Figure 2.9. Graphene layers are on top of the substrates and they are located as they facing to each other. An ionic liquid and a spacer fill the gap between two graphene layers. There is an incident radiation with an angle of incidence θ_1. The simulation gives the reflected, transmitted, and absorbed ratio of the incident radiation.

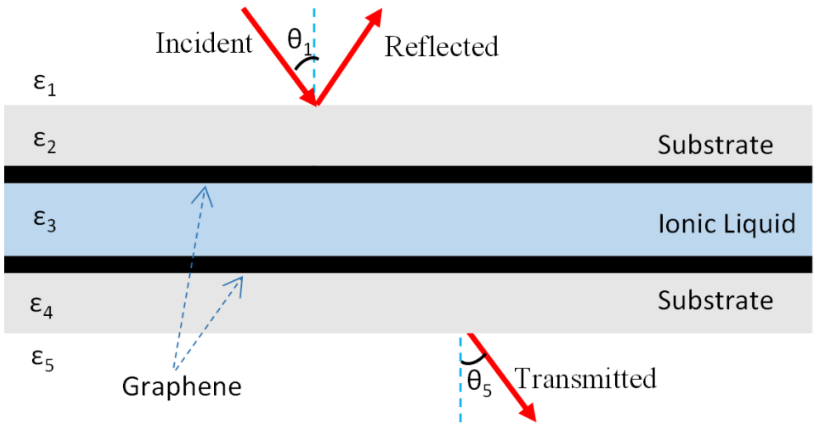

Figure 2.9 Schematic representation of a drawn graphene supercapacitor which used in the transfer matrix calculations.

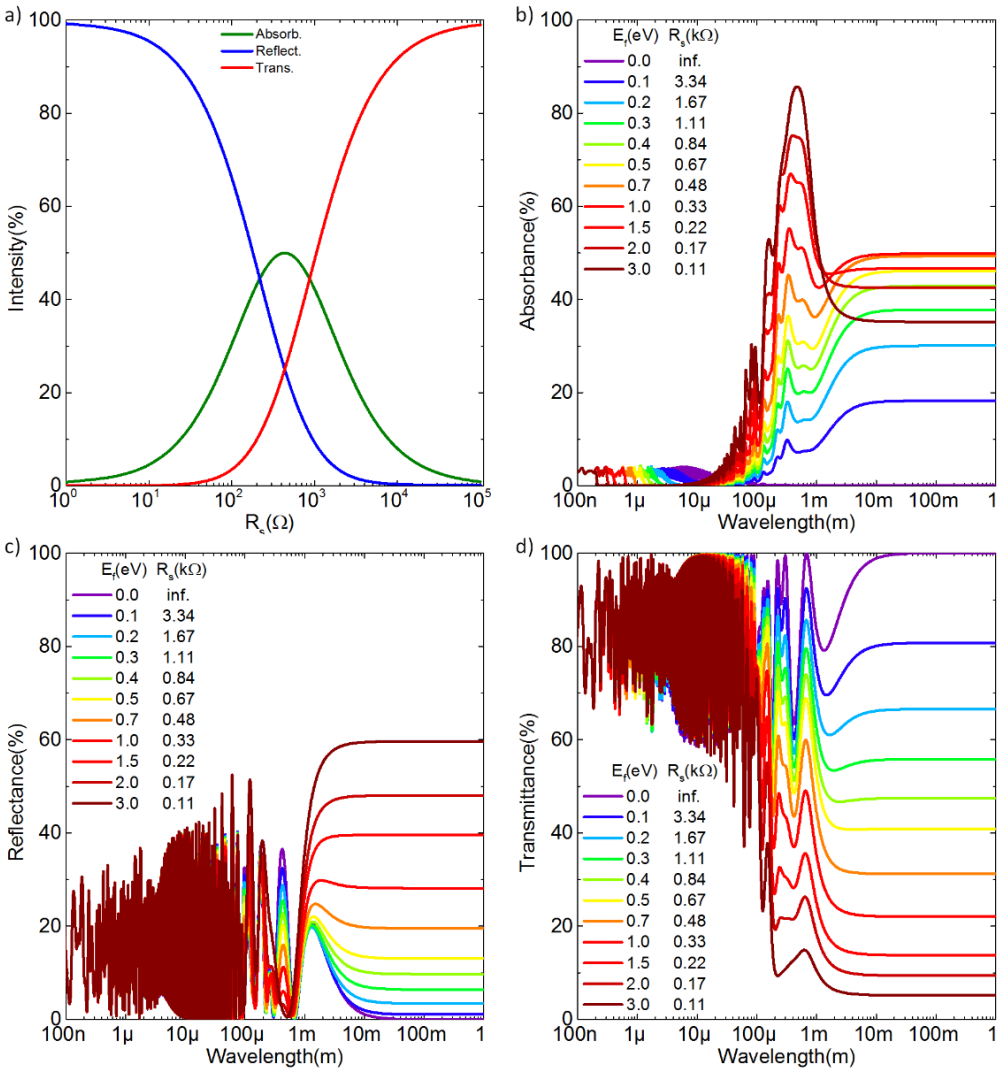

Figure 2.10 Simulated optical response of graphene supercapacitor including the dielectric constants of supporting substrates and ionic liquid. (a) Absorbance, reflectance, and transmittance of incident radiation with $3cm$ wavelength. It is assumed that the angle of incidence is 30^o. Absorbance (b), reflectance (c), and transmittance (d) as function of wavelength ranging from $100nm$ to $1m$ for various Fermi energies and sheet resistances of one layer graphene in a graphene supercapacitor. At short wavelengths, there are interference effects especially in the far-infrared and terahertz frequencies due to the comparable length scales between thicknesses of layers and wavelengths.

Simulated optical response of a graphene super capacitor is shown in Figure 2.10. Here the angle of incidence is 30^o and wavelength of the incident radiation is $3cm$. Dielectric constant of substrates and ionic liquid are assumed to be 3 and 2, respectively, for the wavelength of $3cm$ [25]. First and fifth layers are a free space having a large thickness. Second and fourth layers having the thickness of $80\mu m$ are the supporting substrates for graphene layers. The third layer is the ionic liquid and the spacer possessing a thickness of $40\mu m$ between two graphene layers. The incident electric field is assumed to be in-plane, therefore, incident radiation is s-polarized. Absorbance, reflectance, and transmittance of single layer graphene are calculated as a function of the sheet resistance (Figure 2.10(a)). Absorbance has a maximum value at $0.43k\Omega$ sheet resistance of single layer graphene. Reflectance decreases and transmittance increases as the sheet resistance of graphene decreases. Graphene layers become less metallic as the sheet resistance decreases. If the total impedance of all layers of the device is added, the total impedance is found to be half of the free space impedance i.e. 188.5Ω. For various Fermi energies, absorbance, reflectance, and transmittance are calculated in a broad wavelengths ranging from $100nm$ to $1m$ (Figure 2.10(b, c, d)). Absorbance of graphene increases as the intraband conductivity of graphene increases in terahertz and microwave frequencies. At shorter wavelengths, there are Fabry Perot resonances between the layers of the device due to the comparable thicknesses of the layers with the wavelength of incident radiation. In addition, the angle of incidence dependence of optical parameters for graphene supercapacitors is simulated for s- and p-polarized incident radiations. For an s-polarized radiation, electric field is in the device plane and magnetic field is in the incidence plane. Simulated optical parameters for graphene capacitor are shown in Figure 2.11 for $3cm$ wavelength. The maximum absorbance value being 50% is constant for various angles of incidences but the peak position shifts to higher sheet resistance values. While the angle of incidence increases, incident radiation experiences less surface impedance.

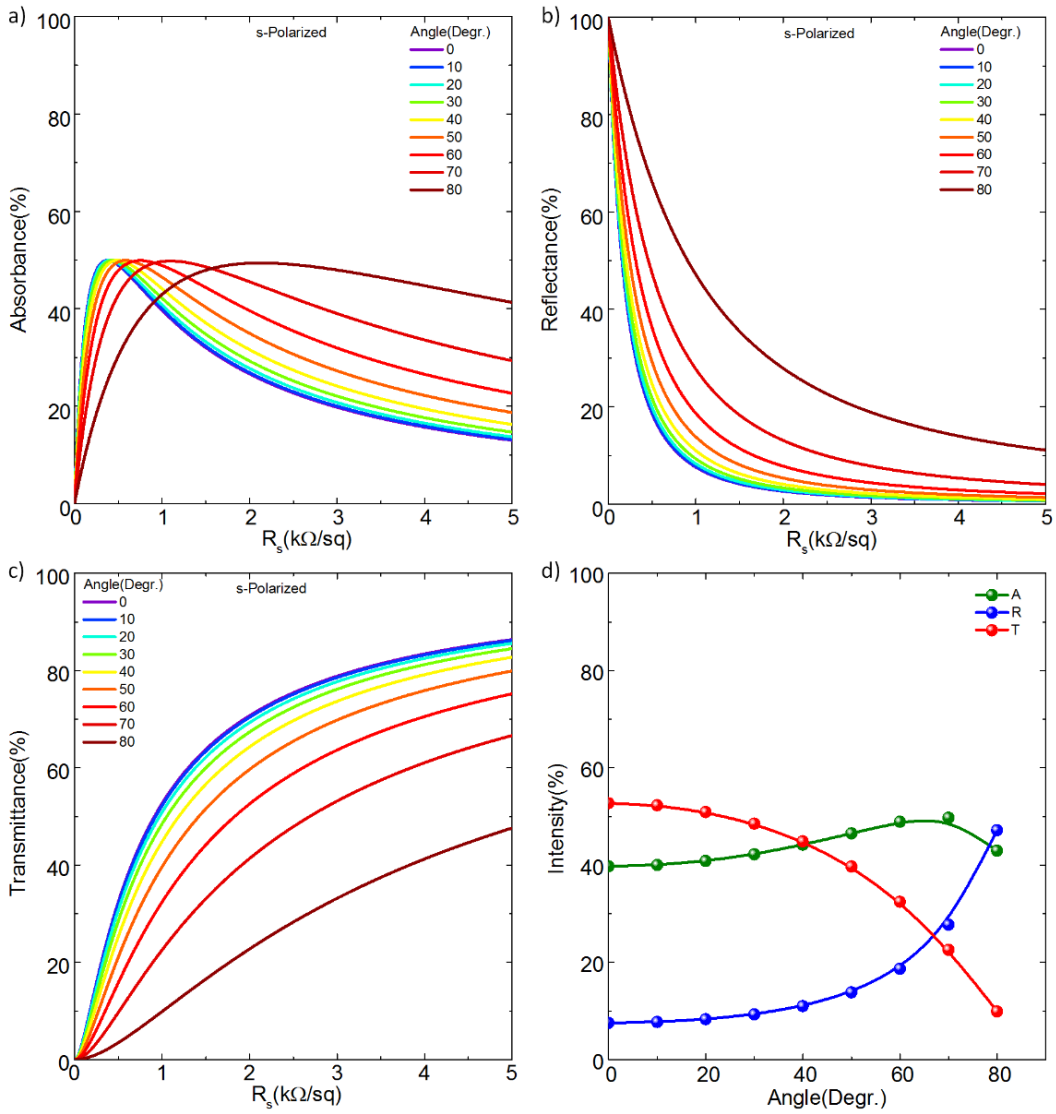

Figure 2.11 Optical response of a graphene supercapacitor for various angle of incidences for an s-polarized radiation. Absorbance (a), reflectance (b), and transmittance (c) of the device as function of sheet resistance are graphed. As the angle of incidence increases, incident radiation experiences more impedance. Absorbance reaches its maximum value at high sheet resistance of single layer graphene. (a) Absorbance, reflectance, and transmittance of the device at $1k\Omega$ sheet resistance are shown.

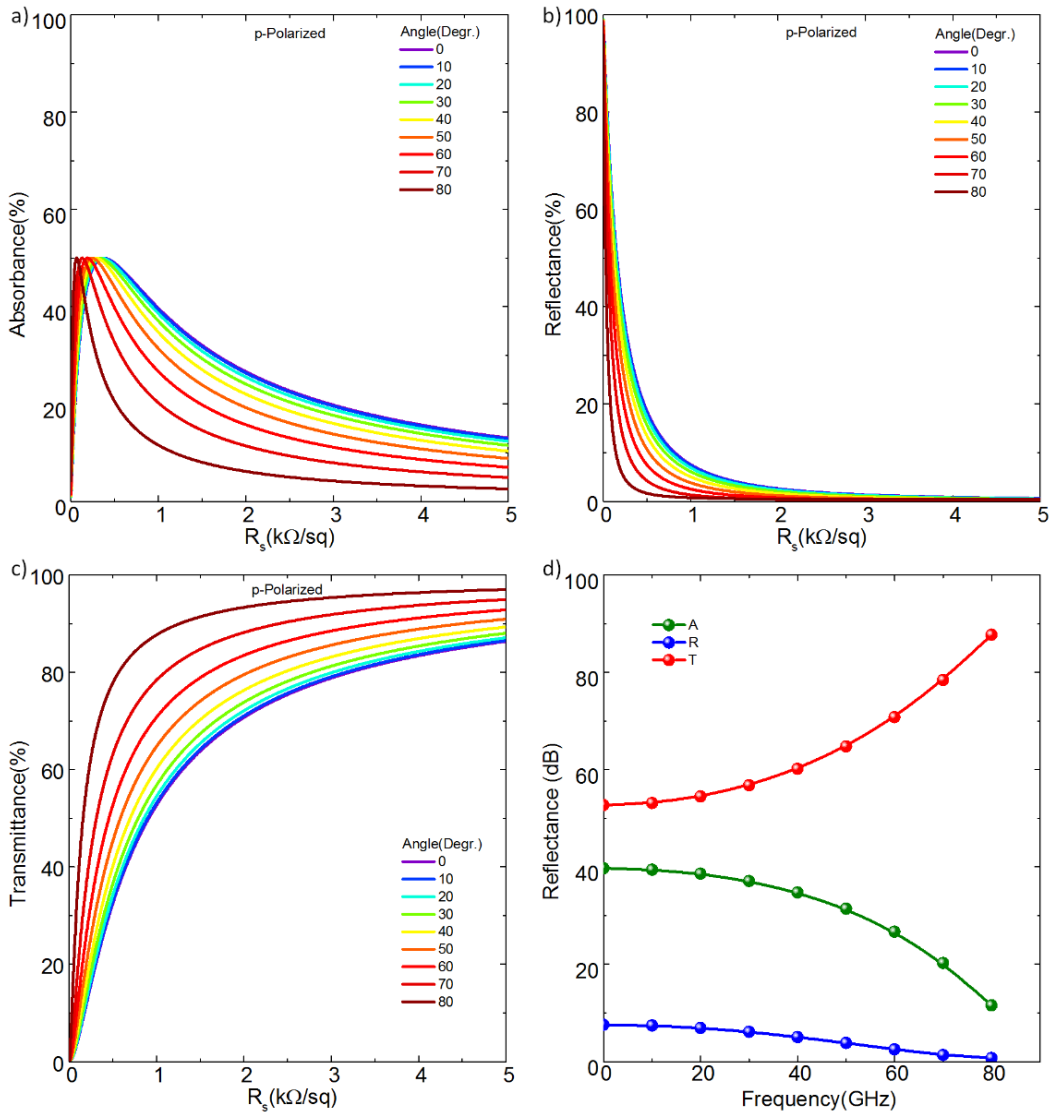

Figure 2.12 Optical response of graphene capacitor is shown for p-polarized radiation. Absorbance (a), reflectance (b), and transmittance (c) are plotted as a function of sheet resistance of graphene layers. For p-polarization, peak position of the absorbance shifts to smaller resistances as the angle of incidence increases. Absorbance and reflectance decrease and transmittance increases as the angle of incidence increases, (d).

Therefore the reflected intensity increases but transmitted intensity decreases as the angle of incidence is increased (Figure 2.11(d)). For a p-polarized incident radiation, electric field is in the incidence plane and magnetic field is on the device plane. The optical response of graphene capacitor has been calculated for p-polarized incident radiation on the graphene capacitor (Figure 2.12). As the incidence angle is increased, the maximum value of absorbance is not varying. Peak position of absorbance shifts to the smaller sheet resistance values (Figure 2.12(a)). We plot the reflectance and transmittance as a function of sheet resistance for various angle of incidence (Figure 2.12(b, c)). As the angle of incidence is increased, absorbance and reflectance decrease and transmittance increases (Figure 2.12(d)) for $1k\Omega$ sheet resistance of graphene. Incident electromagnetic wave experiences less total impedance as the angle of incidence increases and hence graphene capacitor behaves more transparent at higher incidence angels.

Chapter 3

Fabrication of large area graphene supercapacitors

A supercapacitor can hold more electrical charges and store much more energy when compared to standard commercially available dielectric based electrolytic capacitors. There are two electrodes in a supercapacitor as in the electrolytic capacitor but supercapacitors use electrolyte instead of a dielectric between the electrodes. Graphene supercapacitors use two graphene layers as the electrodes of the supercapacitor and an electrolyte in between them. Applied bias is linearly distributed between two electrodes of the standard dielectric capacitor hence the created electric field is constant and weak (Figure 1.2). However, applied bias drops sharply in the electrical double layer of graphene supercapacitors hence created electric field is very high (Figure 1.2).When a bias is applied to the two electrodes of a graphene supercapacitor, the electrolyte is polarized and electrical charges are collected on two electrical double layers (EDL) at electrode-electrolyte interface. The graphene based supercapacitors are also used for high performance energy storage purposes, multilayer or porous single layer graphene layers are used to achieve large surface area for the capacitor. Increasing the surface area of the capacitor increases the charge

storage capacity of the capacitor. Our device is not appropriate for high energy storage applications due to its insufficient surface area. Our aim is to change the optical properties of single layer graphene by collecting large number of electrical charges on graphene surface. High charge density on graphene surface dopes graphene and shifts the Fermi energy level up or down. Therefore, the optical conductivity and absorbance of graphene can be tuned by tuning the Fermi level of single layer graphene. For this purpose, we will first explain the synthesis and transfer of graphene on PVC substrate, then we will explain the fabrication and characterization of large area graphene supercapacitors in the next two sections.

3.1.Synthesis of graphene

We synthesized large area graphene by using chemical vapor deposition (CVD) on ultra-smooth copper foils having $0.1\mu m$ surface roughness purchased from Mitsui mining and smelting company (LTD, B1-SBS). A quartz chamber having a diameter of $8cm$ was used in a double zone split furnace having a zone length of 60cm as shown in Figure 3.1(b). Large area graphene growth starts by cutting smooth copper foils with an appropriate dimensions and locating copper foils on a flat quartz holder as shown in Figure 3.1(a). The quartz holder has $30cm$ length and $7cm$ width. Copper foils are heated in the furnace until 1035^oC under $100sccm\ H_2$ flow; here hydrogen is used for removal of the oxide layer on the surface of the copper foils. When the temperature of the furnace is at 1035^oC, graphene growth starts by sending $10sccm\ CH_4$ to the chamber. The growth temperature and duration are 1035^oC and $45s$, respectively. After terminating the growth by stopping the flow of CH_4, the copper foils are cooled down to the room temperature under again $100sccm\ H_2$ flow. At room temperature, H_2 flow and vacuum pump are stopped, and the chamber is opened to the atmospheric pressure. Subsequently, the copper foils are removed from the furnace as shown in Figure 3.1(c). Maximum size

of graphene that can be grown is the same size with the quartz holder ($30cm$ by $7cm$). The width and length of the holder cannot be increased further because of the restricted diameter of quartz chamber and length of the furnace. The size of the quartz chamber and the furnace limit the growth of large area graphene in one growth. If the sizes of the chamber and the furnace are increased, than it is possible to grow large area graphene layers on copper foils in a single growth. However, one of the problems is the cost of growth system. The cost increases with the size of the furnace and the quartz chamber for ordinary and standard sizes as expected. However, the cost increases incredibly for special, rare, and large furnaces and quartz chambers. Another problem is the non-uniformity of the temperature distribution in a large chamber, a uniform temperature distribution is required for a high quality and uniform graphene growth. Therefore, growing large area and high quality of graphene is a very big challenge. The approach used here to fabricate large area uniform graphene is based on welding of grown graphene samples to each other rather than growing a large area graphene in one step. This approach is unique and developed in this research and in this way large area graphene samples can be easily fabricated at lower cost. A number of graphene samples are grown on copper foils and then these graphene grown copper foils are welded to each other during the transfer process as explained in detail in the next section. Graphene is grown on two pieces of copper foils having the dimensions of $14cm$ length and $7cm$ width in one growth to be able to obtain a graphene sample with dimensions of $14cm$ length and $14cm$ width as pictured in Figure 3.1.

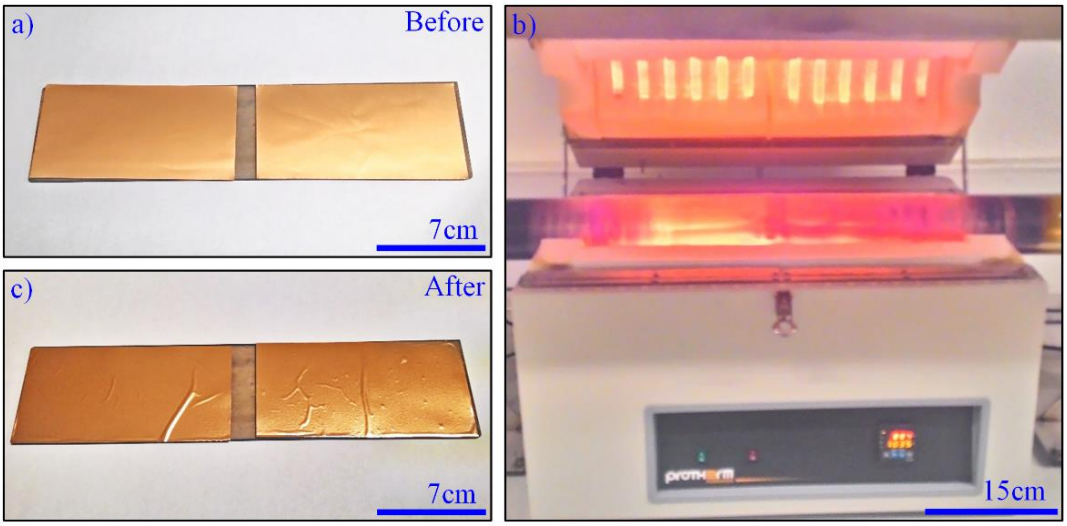

Figure 3.1 Photographs of the smooth copper and the high temperature furnace. Before starting growth process, the smooth copper foils are cut according to the size of the flat quartz holder and then the copper foils are located on the holder as shown in a). Quartz holder has $30cm$ length and $7cm$ width, the diameter of the quartz chamber is $8cm$. The holder is located at the center of the quartz chamber and the chamber is vacuumed with an oil pump. Then the foils are heated until 1035^oC under $100sccm\ H_2$ flow by using a double zone high temperature split furnace with a width of $60cm$ shown in b). Graphene is grown by sending $10sccm$ of CH_4 with $100sccm\ H_2$ for $10s$. After growth of graphene, copper foils are removed from the furnace after cooling furnace down to the room temperature under $100sccm\ H_2$ as shown in c).

3.1.1.Transfer of graphene

After growing graphene on copper foils, it is transferred to polyvinyl chloride (PVC) substrate. Two pieces of graphene are grown with a size of $14cm$ length and $7cm$ width, Figure 3.1. In order to fabricate larger area graphene samples, a new transfer method called here as graphene welding has been used. Two graphene grown copper foils are welded to each other instead of increasing the chamber and furnace size. The

graphene welding process is shown in Figure 3.2. Two graphene layers grown on copper foils are laid on the fusible side of a PVC substrate with a short overlap. It should be clarified here that the graphene to be transferred is located between the copper foils and the PVC substrate. There is a gap between two overlapping graphene layers grown on copper foils and PVC substrate before lamination. When the PVC is heated to $\sim 120^{o}C$ by a lamination machine, the gap is filled with the PVC polymer. Two graphene layers are electrically connected to each other after etching the copper foils. There is no contact resistance between two graphene layers after the welding process. In other words, the sheet resistance of graphene is the same when measured along the welding line or perpendicular to the welding line. Welding of two different graphene layers is similar to the growth process of graphene. In the growth process of graphene, graphene starts to grow from a nucleation center on the surface of a polycrystalline copper foil. There are number of nucleation centers on copper surface and each nucleation center drives the growth of one grain of graphene. During the graphene growth process, the grains become larger size and meet on the grain boundaries. Although each graphene grains are different, they are physically connected to each other through grain boundaries. On the other hand, during the graphene welding process, two different graphene layers are connected by welding process. It can be concluded that the graphene welding is a physical connection of graphene layers similar to the connections between two grains of graphene during the graphene growth. Graphene grown on copper foils is transferred onto the PVC substrate as indicated in Figure 3.3. Two graphene layers grown on copper foils are inserted between PVC and an ordinary A4 paper with a short overlap between two copper foils as shown in Figure 3.3 (a) and (b). Afterwards, paper-copper-PVC stack is laminated by a laminating machine as shown in Figure 3.3 (c), (d), (e). Laminating machine heats and melts the PVC polymer at the graphene-PVC interface and two rollers press melted polymer to conformably coat graphene surface. Melted PVC physically sticks to the graphene surface when it is cooled down to the room temperature. Before the lamination process, graphene grown on the copper foils is

free and it has some surface roughness as shown in Figure 3.3 (a) and (b). After laminating copper foils, graphene layers perfectly stick to PVC support as shown in Figure 3.3 (f). There is a short step having a height of $\sim 10\mu m$ between the laminated graphene layers at the welding point due to the welding process shown in Figure 3.2. The height of the step is negligible for long wavelength applications.

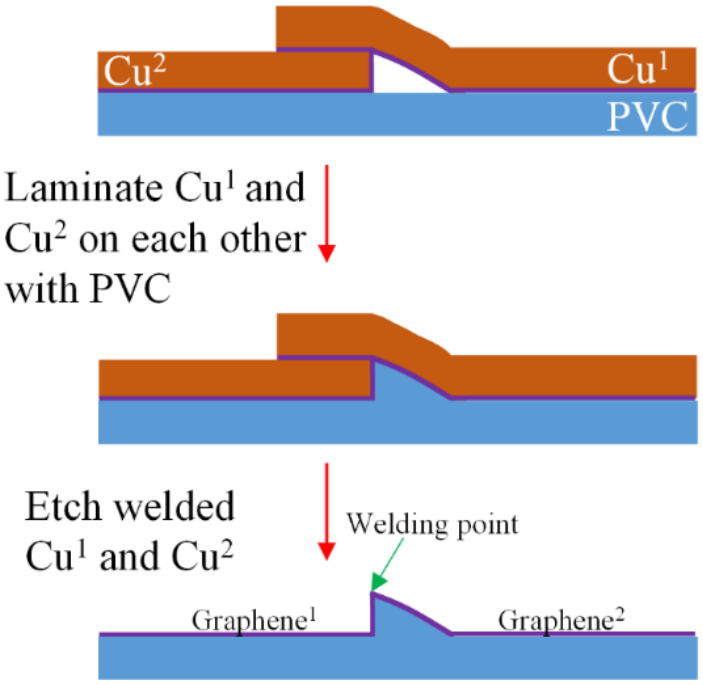

Figure 3.2 Schematic demonstration of the graphene welding process of two pieces of graphene grown copper foils. After synthesis of graphene on copper foils, copper foils are located on the fusible side of a PVC substrate with a short overlap as the graphene grown sides are on the PVC substrate. Subsequently, an A4 paper sheet was laid on the overlapping copper foils as a back support and the whole sample is laminated by using a hot lamination machine. Before laminating process, there is a gap between two copper foils and PVC substrate at the intersection area. When two copper foils are laminated, the gap between the two copper foils is filled with melted PVC and thus two graphene layers are welded to each other at the intersection point. After etching copper foils, welded and electrically contacted graphene layers on PVC remain on the surface of PVC.

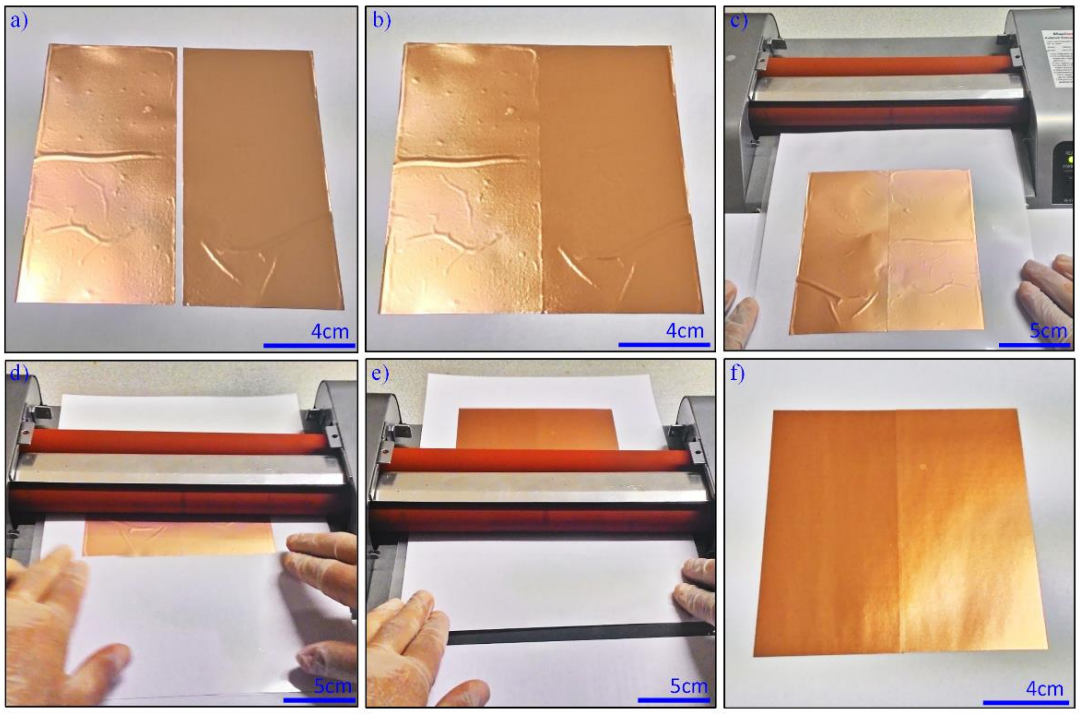

Figure 3.3 Transfer process of graphene on copper foils to the PVC substrate by using a hot laminating machine is shown. Graphene grown on copper foils are located between a paper and a PVC film as in a). Then two graphene layers are welded as explained in Figure 3.2 and shown in b). Graphene grown on the top surface of the copper foils is transferred and therefore the fusible side of the PVC film is put on top of the copper foils as shown in a) and b). Finally, paper-copper-PVC stack is laminated in a hot laminating machine as shown in c), d) and e). The temperature of the laminating machine is $\sim 120^{o}C$. Laminated and welded graphene grown copper foils are shown in f).

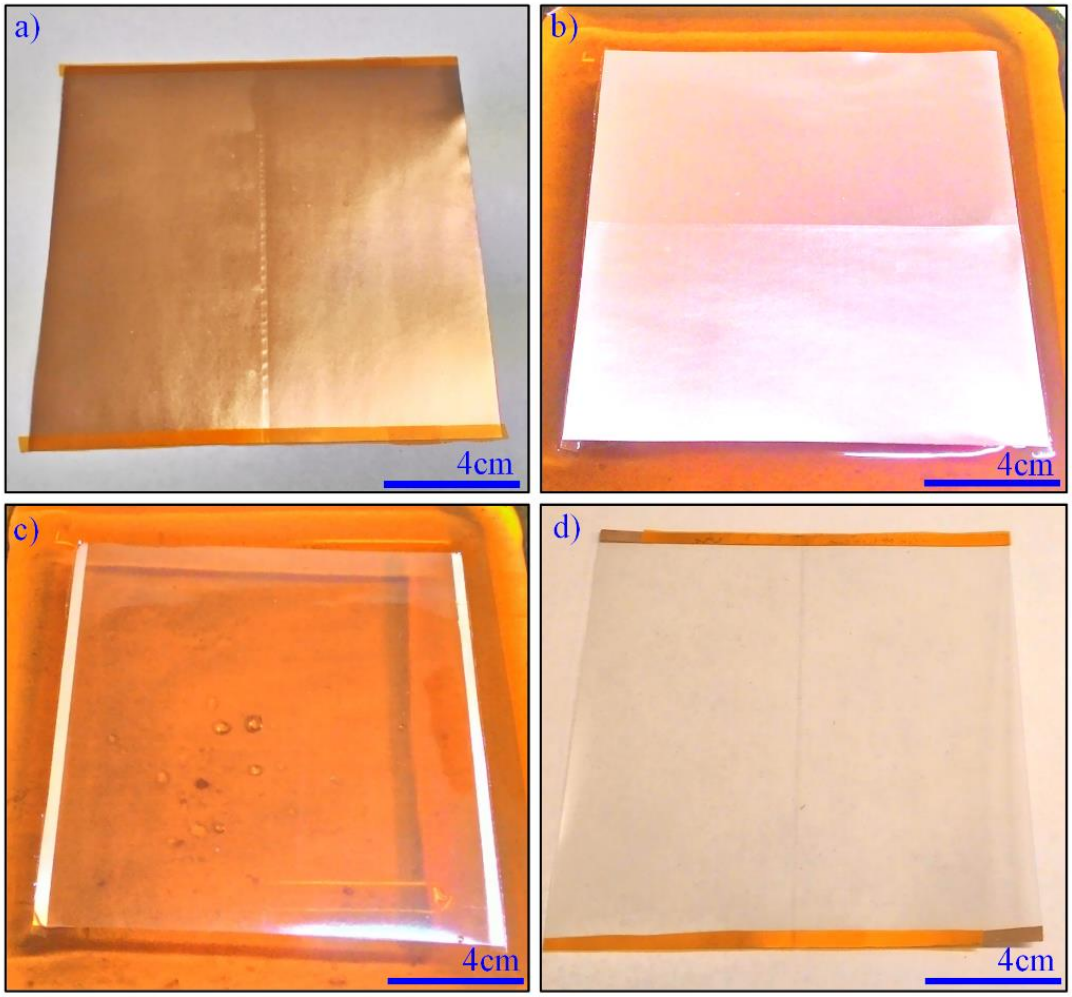

Figure 3.4 Chemical etching process of laminated graphene layers grown on copper is shown. Two tapes are used to cover the two ends of laminated copper foils in order not to etch copper foils under the tape, a). Electrical contact from the transferred graphene layers are taken by using copper foils that are used for graphene growth. The copper foils are chemically etched in $\sim 5mM$ aqueous solution of FCl_3 in $\sim 10min.$ as shown in b) and c). After washing in a clean DI water and drying, graphene layers on the PVC having two copper contacts is obtained as in d).

After laminating graphene layers to the PVC polymer, the copper foils have to be etched to be able to obtain single layer graphene on PVC substrate. $\sim 5mM\ FCl_3$ In an aqueous solution is used to etch $10\mu m$ thick copper foil in $10min$. Two pieces of tapes are used to cover the two ends of laminated copper foils as shown in Figure 3.4 (a). These tapes do not let tape covered parts of the copper foils to be etched, uncovered parts of copper foil is etched by FCl_3 aqueous solution as shown in Figure 3.4 (b) and (c). Un-etched copper foils are used to take electrical contact from graphene samples.

3.1.2.Electrical and optical characterization of single layer graphene

Graphene needs to be characterized to determine the number of layers and continuity of graphene after growth and transfer processes. We have optically and electrically characterized transferred graphene samples. For optical characterization, FTIR and Raman microscopes have been employed. We measured the transmission of single layer graphene on PVC substrate in the visible and near-IR frequencies by using FTIR (Figure 3.5). Firstly, we measured the optical transmission of PVC substrate without graphene layer. Then we measured the optical transmission of PVC substrate with graphene and the transmission measurements were normalized to PVC substrate. As a result, graphene absorbs $\sim\%2.5$ of the incident radiation at near-IR region but absorption of the graphene increases in the UV frequencies to$\sim$ %4 (Figure 3.5 (b)). The reason behind the constant absorption of $\sim\%2.5$ is due to the interband transition of graphene as it has been extensively discussed in the previous chapter. Theoretical value of the constant absorption of graphene in the visible region of the electromagnetic spectrum is $\sim\%2.24$ that is smaller than the experimentally measured value. During the calculation, we assume that graphene is in free space. The difference between experimentally measured and theoretical calculations is mainly due to the excitonic effects that is not considered during the simulation.

Highly energetic incident photons excite an electron from the valance band to the conduction band and hence a hole is created in the valance band. Then these electrons and holes lowers their energies by going from higher to lower energy states by radiating most of the absorbed energies. As a result, graphene transmits most of the incident radiation. Remaining energy is consumed by the generated electron hole pair called exciton and universal absorbance of graphene. The conductivity of graphene goes over the universal conductivity in the visible and UV frequencies due to excitonic contributions and thus the absorbance of the graphene goes beyond the universally constant interband absorbance of $\sim\%2.24$. The large increment in the absorption of graphene from near-IR to UV from $\sim\%2.5$ to $\sim\%4$ is due to the excitonic contribution to the interband conductivity of graphene. Another reason for the difference between experimentally measured and theoretically calculated absorbance is the optical scattering due to the surface roughness of PVC substrate. The reference measurement have been performed but the reference PVC and the graphene transferred PVC are not identical. Another reason for the difference is the dielectric constant of the PVC substrate in the visible and near-IR frequencies, graphene is assumed to be in free space during calculations.

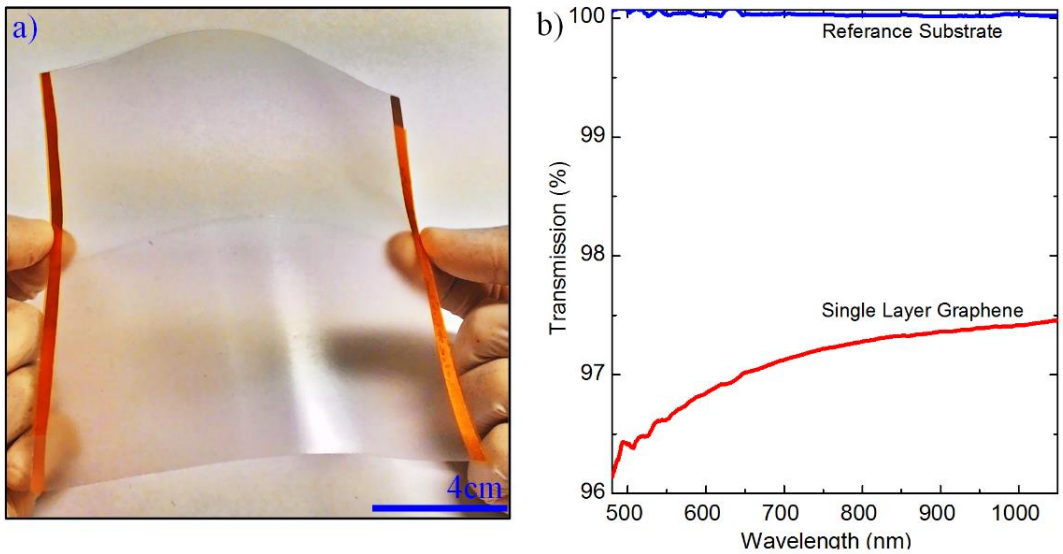

Figure 3.5 Transmission measurement of large area graphene transferred on PVC substrate. The photograph of a single layer graphene on a PVC substrate having two copper contact lines is shown in (a). FTIR spectrometer is used for the transmission measurements, where the transmission of graphene transferred on PVC substrate has been taken and normalized to a reference signal from a PVC substrate without graphene, (b). Due to the excitonic contribution to the absorbance of graphene, transmission decreases for higher energies as shown in (b).

Another method used for the optical characterization of single layer graphene is Raman spectroscopy. Graphene transferred to PVC substrate has a rough surface; therefore, it is not easy to observe a Raman excitation on PVC substrate. Instead, we use graphene transferred to a glass substrate which has a better surface roughness than the PVC substrate. We transferred graphene to a glass substrate by using Shipley 1813 photoresist. We drop few droplets of the resist on graphene grown copper and then the resist solvent was evaporated in the furnace at 80^oC overnight. When the resist solvent evaporates, the resist on the copper foil becomes hard and, then we etched the copper foils in $FeCl_3$ aqueous solution. Then we put the

graphene-resist stack on a glass substrate and then we anneal the glass at 80^oC on a hot plate for few minutes. Immediately after annealing at 80^oC, we anneal the glass at 120^oC on another hot plate approximately for 1 minute. Then the resist-graphene stack adhered to the glass surface and then we dissolve the resist in acetone organic solvent. After washing and drying the glass, single layer graphene on glass substrate is ready for the measurement as shown in Figure 3.6 (a).

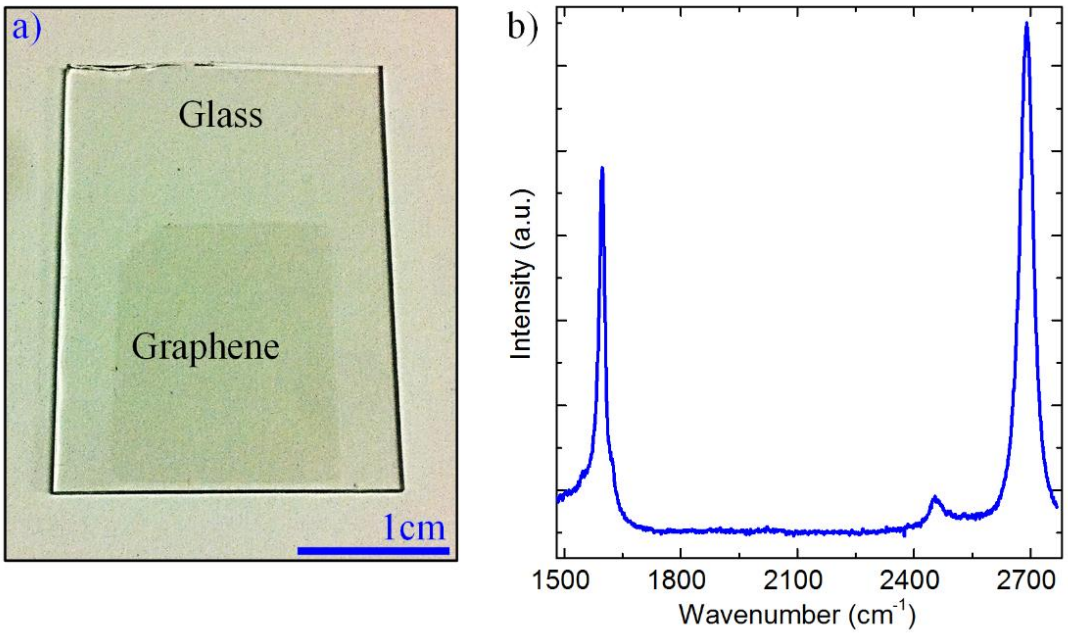

Figure 3.6 Optical Raman spectroscopy spectrum of single layer graphene transferred to a glass substrate. The photograph of the graphene on glass is shown in (a). Thanks to the absorption of single layer graphene absorbing ~%2.24 in the visible spectrum, graphene is darker than glass in the photograph. Typical Raman peaks of single layer graphene are shown, a laser with a wavelength of $632nm$ is used. 2D band is at $2700cm^{-1}$ and G band is at $1600cm^{-1}$ wavenumber. The intensity ratio of G band to the 2D band is 1.36.

A laser with a wavelength of $632nm$ is used to measure the Raman scattering from graphene surface. Measured Raman signals of graphene on glass are indicated in Figure 3.6 (b). Shifted energy peaks in Raman spectrum represent some energy bands and these bands give key information about the quality and the number of graphene layers of the investigated sample. The G band shows the in-plane vibrational modes of sp^2 hybridized carbon atoms. Expected position of this band is at $1587cm^{-1}$ for a single layer of graphene. Doping of graphene and the number of graphene layers determine the position and intensity of the G band. As the number of layer increases, G band shifts to lower energies. This shows that the $C-C$ bond energies decrease as the number of graphene layers increase. Moreover, the intensity of the G band increases with the number of graphene layers. If doping of graphene is increased than the G band energy shifts to higher wavenumbers. Intensity of the G band does not vary too much with doping. In the measurements, it is obvious that G band is located at $1595cm^{-1}$, Figure 3.6(b). This value is higher than the pristine graphene G band position because the graphene used here is p-type doped after chemical etching. Another interesting band in the graphene Raman spectrum is the D band showing the radial breathing mode of carbon rings in the graphene lattice. In pristine graphene and in graphite, D band is quite negligible. If there are defects in the carbon lattice of graphene, then D band intensity increases due to the defect increasing the scattering of the incoming laser light. The D band is expected to be at $1350\ cm^{-1}$, consistently it is located at $\sim 1350\ cm^{-1}$ in the experimental measurements. Another interesting band in the Raman spectrum of graphene is the $2D$ band showing two phonon double resonant intervalley scattering energies. This band does not need a defect to be activated; it strongly exists in pristine graphene and graphite samples. For single layer graphene, it is expected that $2D$ band is very symmetric and has FWHM of $30cm^{-1}$ and centered at $2590cm^{-1}$. For multilayer graphene, $2D$ band has a non-symmetric and wide peak and the peak intensity is larger than the single graphene layer. In addition, the peak center is at the lower energies in the case of multilayer graphene. Here in the experimental measurements,

$2D$ band has a symmetric peak with FWHM of $40cm^{-1}$ at $2588cm^{-1}$. Another analysis parameter is the ratio of $2D$ band intensity to the G band intensity; the expected ratio is 2 for pristine graphene. In the measurements, that ratio found to be around 1.35 thanks to the doped graphene layers. Therefore, analysis of $2D$ band also indicates that the graphene used in this study is single layer and has a high quality.

For electrical characterization of fabricated large area graphene on PVC substrate, the sheet resistance of the graphene is measured by using transfer line method. A multimeter is used to measure the resistance of graphene layers possessing varying lengths and the same width as shown in Figure 3.7(a). Then the measured total resistance is multiplied with the width of graphene samples $(R_t.w)$ to be able to calculate the normalized resistance. Then the normalized resistance is plotted as a function of the graphene sample length as shown in Figure 3.7(b). Then the measured data is fitted linearly and the slope of the fitted line is calculated. The slope gives the sheet resistance as $R_s = 3.32k\Omega/sq$; this value of sheet resistance corresponds to the resistance of the slightly doped graphene layers. Another important parameter that can be retrieved from the transmission line plot is the contact resistance of graphene to the copper foil contacts. As demonstrated in the small signal circuit model of graphene in Figure 3.7(c), there are two contact resistances R_c at each graphene-copper contact and there is the sheet resistance R_s of graphene in the circuit model. After assuming the graphene length to be zero, then $2xR_c$ is measured. Therefore, the contact resistance can be calculated from the intersection of the fitted line at the zero length position where the resistance gives two times the contact resistance $2xR_c$. Double contact resistance is due to the two contact resistances in the small signal circuit model of graphene in Figure 3.7(c). The contact resistance is measured here as $\sim R_c = 0.7k\Omega.cm$ which is normalized with a width of the graphene sample. For a graphene sheet having $14cm$ width, the contact resistance per each contact is calculated as $\sim R_c = 0.05k\Omega$. This low contact resistance is quite negligible when compared with the few $k\Omega$ sheet resistance of graphene.

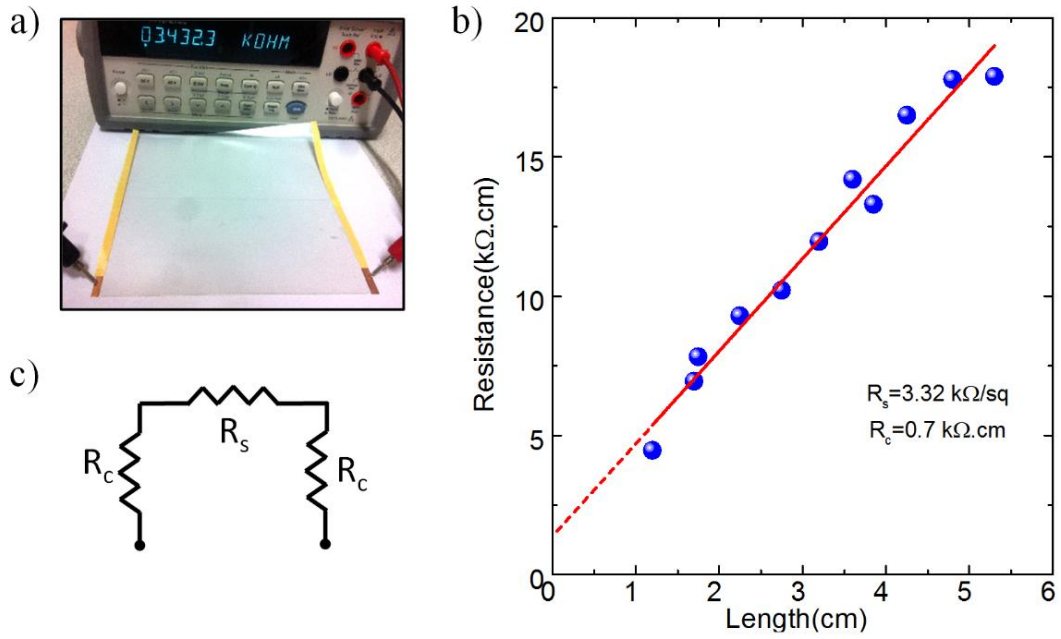

Figure 3.7 Electrical characterization of single layer graphene on PVC substrate is shown. Total resistances of the graphene on PVC substrates with different lengths are measured as in (a). Then the measured resistance is multiplied with the width of the graphene on PVC substrate and plotted as a function of graphene length as shown in (b). The slope of the fitted line gives the sheet resistance of graphene, which is $R_s = 3.32k\Omega/sq$. The resistance value at which the fitted line intersects at zero length is two times the contact resistance of graphene to copper foil contacts having the width of $1cm$. Here the contact resistance is calculated as $\sim R_c = 0.7k\Omega.cm$. The circuit diagram of a graphene layer on PVC substrate with two copper contacts is drawn in (c). There are two contact resistances due to two copper foil contacts and also one sheet resistance which is the sheet resistance of graphene sheet.

3.2.Large area graphene supercapacitors

Large are graphene supercapacitors are fabricated by using two layers of graphene transferred on PVC substrates. Schematic representation of the device is shown in Figure 3.8(a); two graphene layers are used as the electrodes of the capacitor, and an ionic liquid (Diethyl methyl (2-methoxyethyl) ammonium bis (trifluoromethylsulfonyl)imide, [deme][Tf2N]) is used between these two graphene electrodes. The ionic liquid has positively and negatively charged ions and the net charge density is zero. When a bias voltage is applied between these two graphene electrodes, the ionic liquid is polarized and plus and minus charged ions are collected at the ionic liquid-graphene interface. The ions create electrical double layer (EDL) with a thickness of $\sim 1nm$ at that interface. The positively charged ions are collected at negatively charged graphene surface whereas the negatively charged ions are collected at positively charged graphene surface, Figure 3.8(a). If applied potential difference is V, one half of the applied potential is consumed in one EDL and the other half is consumed in the other EDL. The change in the applied potential in such a thin EDL creates a high electric field at the graphene-ionic liquid interface. Due to the high charge density and high electric field at graphene-ionic liquid interface, Fermi energy of graphene is shifted above $1eV$.

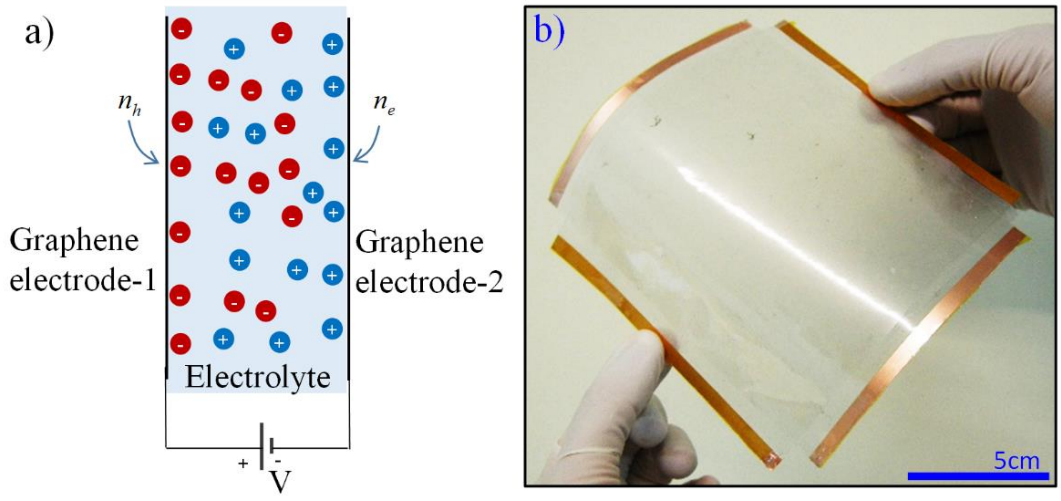

Figure 3.8 Large area graphene supercapacitor is shown. a) Schematic representation of graphene supercapacitor; there are two graphene electrodes and there is an ionic liquid between these two graphene electrodes. A bias voltage is applied between these two graphene electrodes and the ionic liquid is polarized. Negative ions are collected at positive bias applied graphene electrode and positive ions are collected at negative bias applied graphene electrode. Collected ions create $\sim 1nm$ thick electrical double layer (EDL) at graphene-ionic liquid interface. Photograph of the fabricated graphene supercapacitor is shown in b).

3.2.1.Electrical characterization of graphene supercapacitors

Graphene electrodes used in the graphene supercapacitors have electrically tunable Fermi energy. Applying a bias voltage to graphene electrodes create high electric field at graphene ionic liquid interface and that high electric field shifts the Fermi level of graphene from Dirac point to a higher energy level. Tuning the Fermi level energy of graphene with an applied electric field enables tuning the sheet resistance R_s and the quantum capacitance C_q of the graphene layers as well. The

drawn circuit model of the graphene supercapacitor is shown in Figure 3.9(a). Graphene electrodes are represented by a tunable sheet resistance R_s and a tunable quantum capacitance C_q. Two graphene electrodes are connected with an ionic liquid and the ionic liquid is represented by a resistances R_e and a capacitance C_e. C_e Is the electrostatic capacitance of the ionic liquid, it is constant having the value in the order of $\sim 1mF$ and does not vary with a varying bias voltage. R_{e2} Is the resistance due to the electrostatic capacitance of the ionic liquid, this resistance is high and constant for the bias voltages less than $3V$. However, R_e decreases for the voltage values beyond $3V$ which is the limiting voltage value for the stability of ionic liquid. All the experiments are performed for a bias voltages less than $3V$ hence R_e is not considered during the calculations below. Total impedance of the graphene supercapacitor circuit for an AC signal with an amplitude less than or equal to $3V$ can be expressed as

$$Z_{total} = Z_{graphene1} + Z_{electrolyte} + Z_{graphene2} \tag{3.1}$$

If we write contribution of each layer explicitly;

$$Z_{total} = R_{s1} + \frac{1}{iwC_{q1}} + \frac{1}{iwC_e} + R_{s2} + \frac{1}{iwC_{q2}} \tag{3.2}$$

Where, w is the frequency of AC signal. If the two graphene electrodes are assumed to be identical, then

$$Z_{total} = 2R_s + \frac{2}{iwC_{q1}} + \frac{1}{iwC_e} \tag{3.3}$$

If the resistance and capacitance terms are written together

$$Z_{total} = (2R_s) + \frac{1}{iw}\left[\frac{2C_e + C_{q1}}{C_e C_{q1}}\right] \tag{3.4}$$

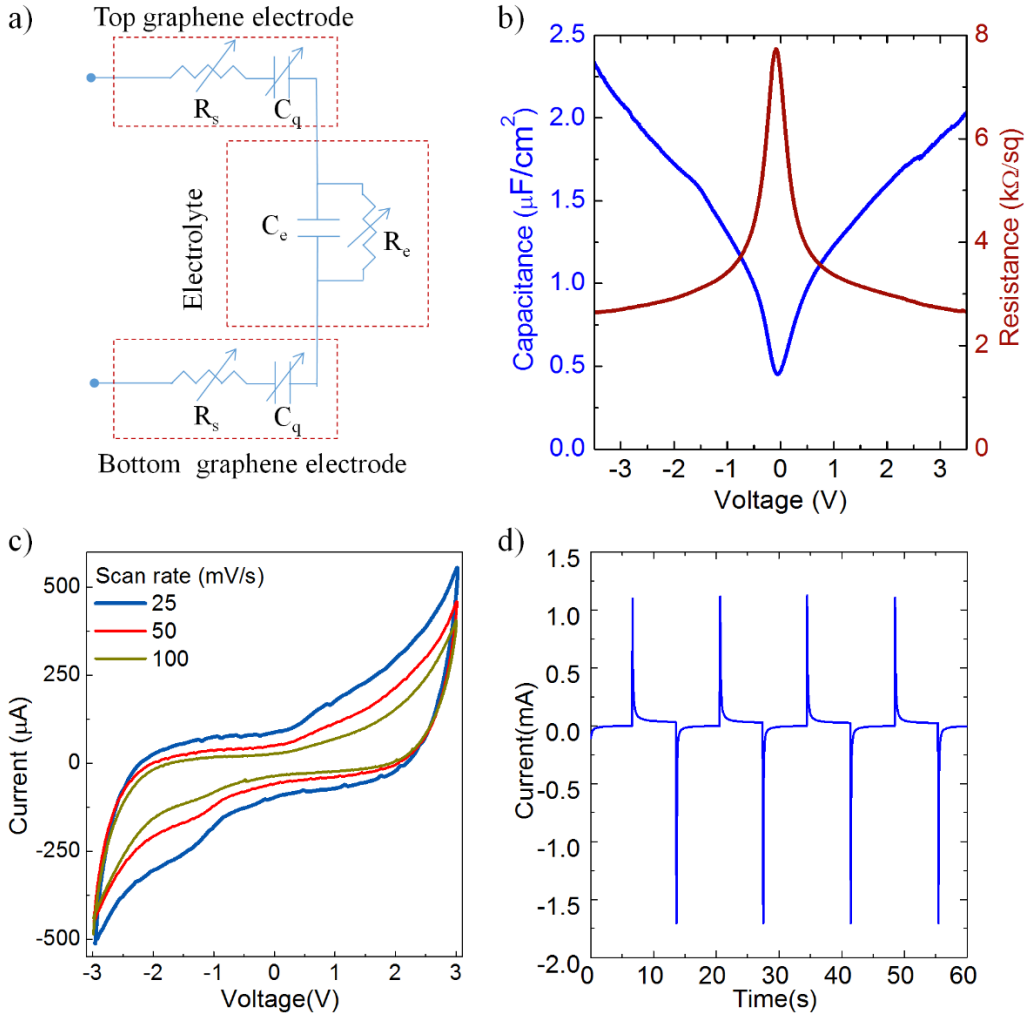

Figure 3.9 Electrical characterization of fabricated large area graphene supercapacitors. (a) Circuit diagram of graphene supercapacitor is shown, graphene electrodes are represented with a tunable capacitance C_q and resistance R_s and electrolyte is represented with a resistance R_e and a capacitance C_e. (b) Modulation of C_q and R_s as a function of voltage is shown. (c) Cyclic voltammetry of graphene supercapacitor is shown, charging and discharging of the capacitor at various scan rates is plotted. (d) We measured time response for charging and discharging of graphene supercapacitor. We apply $3V$ for charging and $0V$ for discharging and record current for the time trace. Time response of both charging and discharging is $\sim 1s$.

Electrostatic capacitance of the ionic liquid is in the order of $1mF$ and quantum capacitance of graphene layer is in the order of $1\mu F$. Therefore the contribution from the ionic liquid to the total capacitance of the device can be safely neglected. Finally, the total impedance can be expressed as

$$Z_{total} = 2R_s + \frac{2}{iwC_{q1}} \tag{3.5}$$

When the total resistance and capacitance of graphene supercapacitor are measured, the resistance and capacitance of graphene layers are measured. HP 4284A precision LCR meter is used to measure capacitance and resistance of the graphene capacitors as a function of the bias voltage. An AC signal with amplitude of 100 mV is applied together with a variable DC voltage to the device. The serial resistance and capacitance were obtained by using serial capacitance and resistance (Rs-Cs) model. By using the measured total resistance and capacitance, the sheet resistance and quantum capacitance of graphene are extracted and then plotted in Figure 3.9(b). At zero voltage, the Fermi level is close to the Dirac point of graphene layers and hence the resistance is at the maximum value ($\sim 8k\Omega/sq$) and the capacitance is at the minimum value ($\sim 0.5\mu F/cm^2$). As the applied bias voltage increases, the resistance decreases down to $\sim 0.8k\Omega/sq$ and the capacitance increases to $\sim 2.3\mu F/cm^2$ as demonstrated in Figure 3.9(b). The cyclic voltammetry of graphene supercapacitors is measured as indicated in Figure 3.9(c). The graphene capacitor is charged and discharged with three scan rates ($25,50,100mV/s$), increasing scan rate decreases the amount of hysteresis of the capacitor. Electrical double layer creates the hysteresis for the graphene supercapacitor. To further characterize time response of charging and discharging of the device, $0V$ and $3V$ are applied to the graphene capacitor in a sequence and the time trace of the charging and discharging current is recorded, Figure 3.9(d). Charging and discharging times are $\sim 1s$, here the time is limited with *RC* time constant of the graphene supercapacitor.

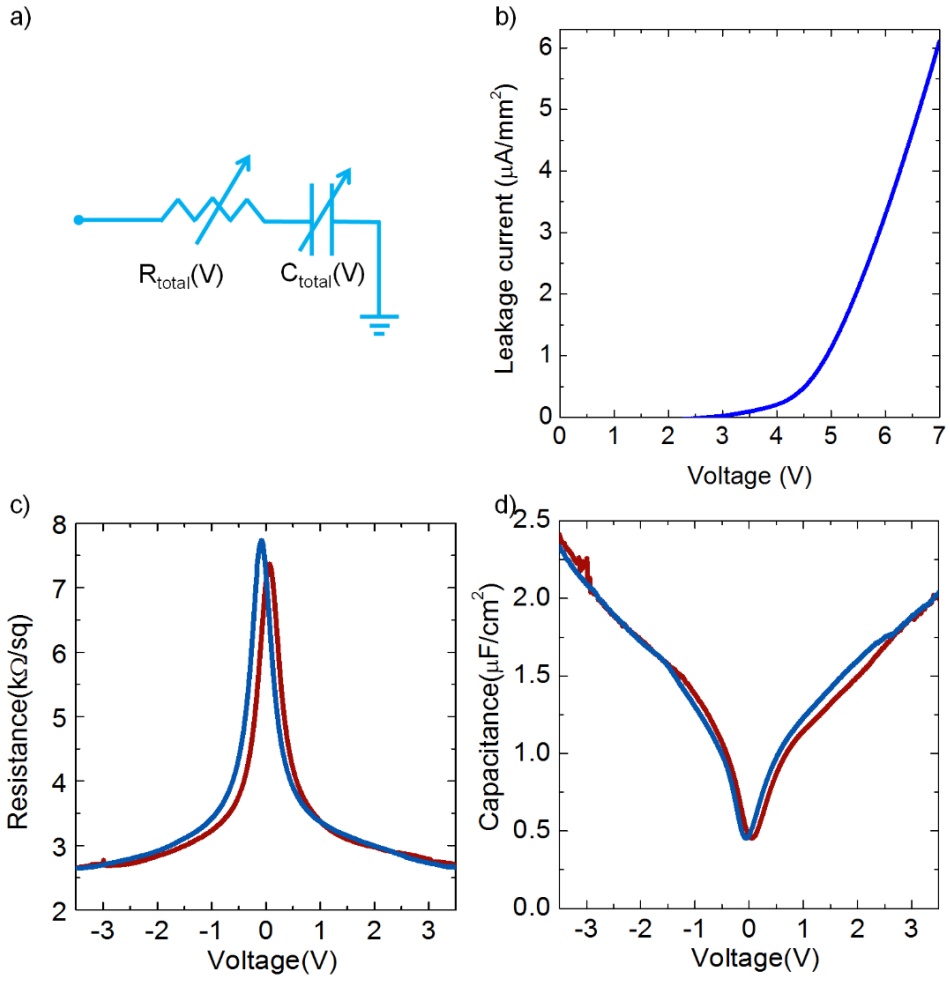

Figure 3.10 Leakage current and hysteresis observed in the transport measurements. (a) Nonlinear RC circuit model used to characterize the leakage current of the graphene super capacitor. (b) Leakage current of the graphene capacitor as a function of bias voltage between the graphene electrodes. (c) Variation of the resistance of graphene electrodes with bias voltage. (d) Variation of the total capacitance of the graphene supercapacitor. In the transport measurements we observed a slight hysteresis.

In order to understand the working range of the graphene supercapacitor device, graphene capacitor is modelled in series connection of a total resistance $R_{total}(V)$ and a total capacitance $C_{total}(V)$ for an applied DC bias as illustrated in Figure 3.10(a). The leakage current of the capacitor is measured as in Figure 3.10(b). Total capacitance has high DC field resistance at bias voltages lower than $3V$ hence leakage current is extremely small at that bias range. When the bias voltages are higher than $3V$, graphene capacitor starts to leak current due to the exceeding of the electrochemical window of the electrolyte as shown in Figure 3.10(b). To further characterize the graphene supercapacitor device, the resistance and capacitance of graphene capacitor are measured during forward bias scan from $-3V$ to $3V$ and reverse bias scan from $3V$ to $-3V$. There is a small hysteresis both in the resistance and the capacitance values as a function of bias voltage as shown in Figure 3.10(c, d).

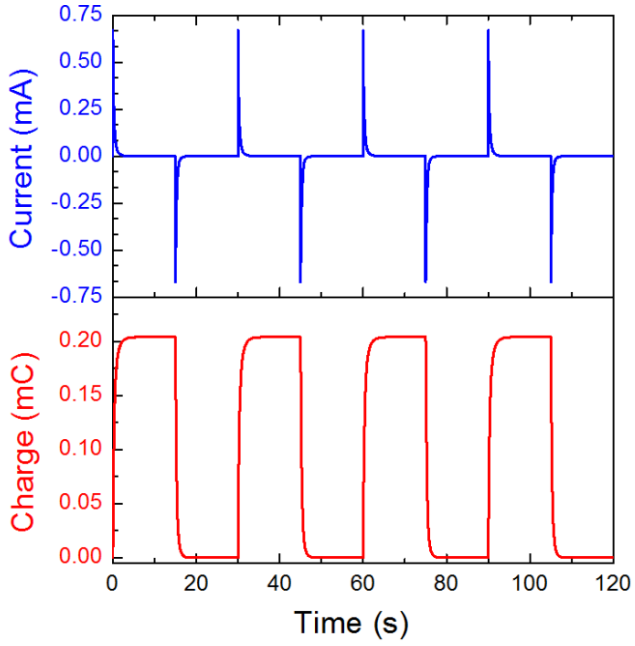

Figure 3.11 Simulated charging and discharging behavior of graphene supercapacitor obtained from the circuit simulator (Advanced Design System (ADS), Agilent). The total charge on the graphene capacitor derived by a square pulse with 30s period and 50% duty cycle.

3.2.2.Optical spectroscopy of graphene supercapacitors

Graphene has a universal optical conductivity in visible and near-IR region of optical spectrum due to interband transitions between the valance and the conduction bands of single layer graphene. Thanks to this constant optical conductivity, graphene absorbs $\sim\%2.24$ of the incident radiation in visible and near-IR frequencies as calculated in the previous chapters. Energy of the absorbed photons depends on the doping level of graphene; if the energy of the incident radiation is lower than $2E_f$, the incident radiation transmits through graphene without absorbing. If the energy of incident photons is larger than $2E_f$, $\sim\%2.24$ of the incident radiation is absorbed by single layer graphene theoretically. Therefore, it is possible to tune absorption of graphene by tuning the Fermi energy of graphene. The transmission modulation of graphene supercapacitor is measured by using Fourier transform infrared spectrometer (FTIR). Schematic of the measurement set up is shown in Figure 3.12(a).There is a broad band light source in the FTIR and a Michelson interferometer. Each time a different spectral decomposition of light beams is exposed to the sample and the transmitted intensity is measured. After taking Fourier transform of the time domain measurement to obtain frequency domain transmission, the spectral transmission response of graphene supercapacitors is obtained. Measured percent change in the transmission of a device is shown in Figure 3.12(b). At the zero voltage, graphene is not fully transparent in the given spectrum. Upon increasing the bias voltage, transmission of the device increases for the energy values lower than the $2E_f$. There are two steps change in the transmission spectrum of the device, these steps correspond to the two graphene layers in the capacitor. By using transmission data, the corresponding Fermi energy of each graphene layers are calculated and shown in Figure 3.12(c). Due to Stefan-Boltzmann like distribution of electrons in the graphene bands at room temperature, absorption variation is not sharp as explained in the chapter 1.

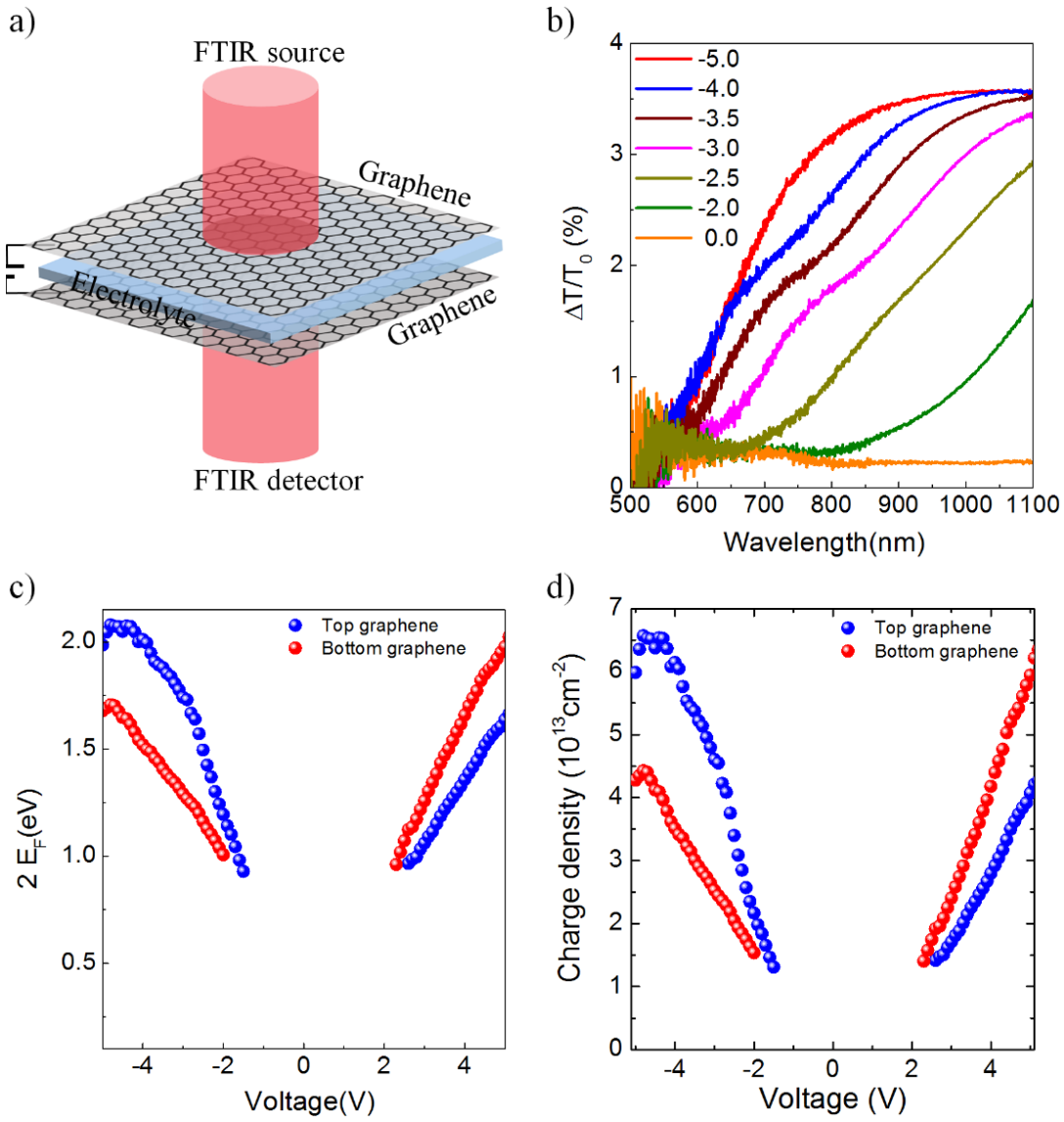

Figure 3.12 Optical characterization of graphene supercapacitors. (a) Schematic drawing of the graphene capacitor and FTIR beam are shown. (b) Modulation of the optical transmission at various bias voltages. Modulation shows a step like spectra with a cutoff at $2E_f$. Two overlapped step-like modulation associated with the bottom and top graphene electrodes are observed. (c) The extracted Fermi energies of the top and bottom graphene electrodes from the optical transmission modulation spectra. (d) The calculated charge densities on the top and bottom graphene electrodes from the extracted Fermi energies.

Therefore the Fermi energy of graphene layers is found at the intersection of half of the absorption and the energy of incident photon. Total absorbance is ~%3.6 and hence each layer absorbs ~%1.8. Corresponding energy at ~%0.9 and ~%2.7 absorption levels for each bias voltages is found. $2E_f$ is obtained as a function of the applied voltage for two graphene layers in graphene capacitor as shown in Figure 3.12(c). Fermi energy of graphene layers is quite linear with the applied bias voltage and each layer have different Fermi energy levels for the same bias voltage. There is no transmission change for the low bias voltages due to the un-intentional doping of graphene. Therefore the Fermi energies cannot be calculated for low bias voltages. The charge density on graphene layers is calculated by using extracted Fermi energy data from the following relation;

$$E_f = \hbar|v_f|\sqrt{n\pi} \tag{3.6}$$

where $\hbar$ is the Planck constant, $v_f = 10^6 m/s$ is the Fermi velocity, n is the charge density of graphene. Charge density of the pristine graphene is in the order of $10^{12} e/cm^2$. The graphene supercapacitor device can increase the charge density of graphene to the level of $0.65x10^{14} e/cm^2$ as shown in Figure 3.12(d).

In Figure 3.9(b) and Figure 3.12(c), sheet resistance and Fermi energy of one graphene layer are measured in graphene supercapacitor as a function of voltage, respectively. Combining these data, the Fermi energy as a function of the sheet resistance is extracted in Figure 3.13(a). The relation between E_f and R_s in Eq.(1.31) is $E_f R_s = 0.334 k\Omega eV$. According to the measurements that multiplication $E_f R_s$ is varying between $0.7 k\Omega eV$ and $1.2 k\Omega eV$. The charge density is calculated as a function of R_s from Figure 3.13(a) by using Eq.(3.6). The charge density versus sheet resistance is plotted in Figure 3.13(b).

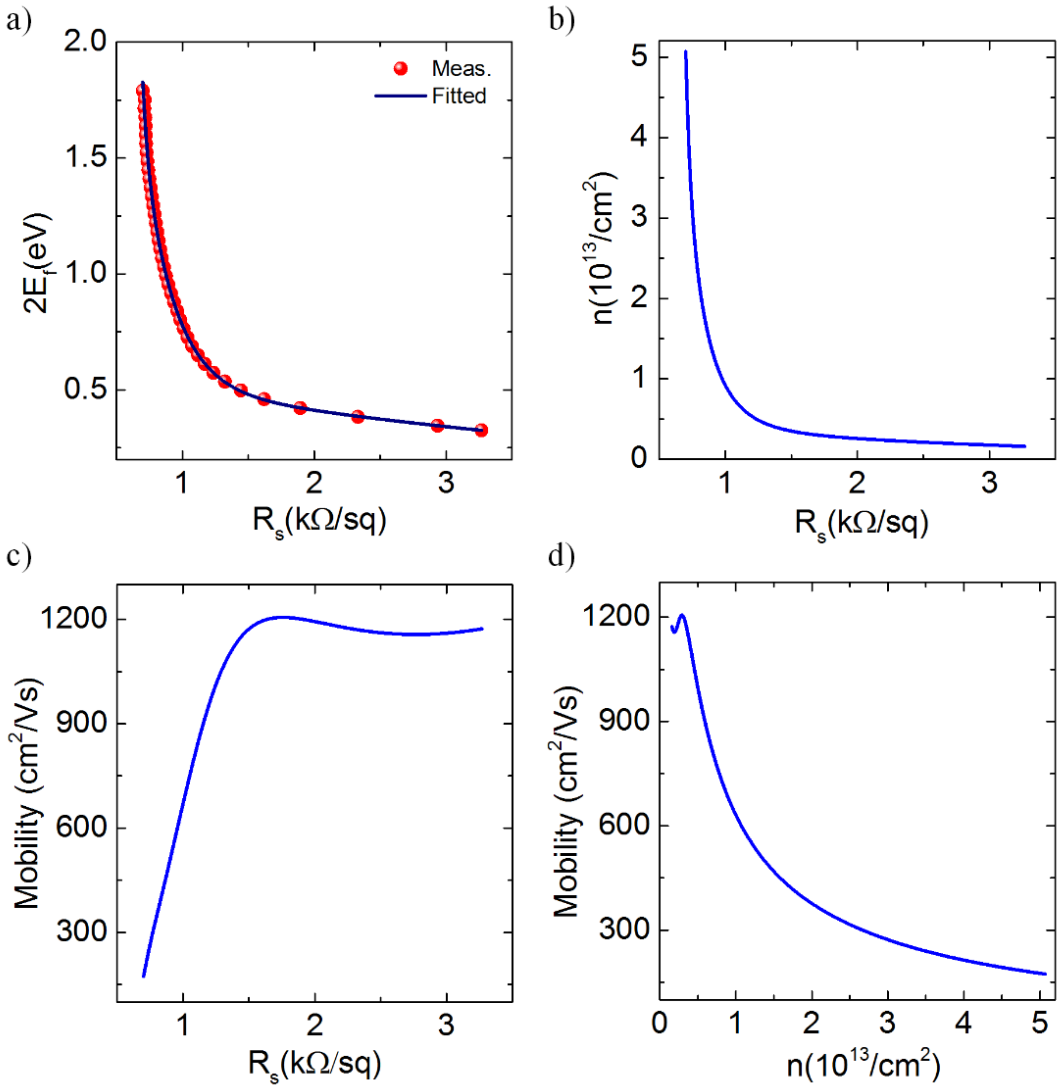

Figure 3.13 Electrical parameters extracted from the transport and optical measurements. (a) Correlation of the Fermi energy with the sheet resistance of the graphene electrode. (b) Charge density vs. Sheet resistance, (c), Extracted charge mobility vs. sheet resistance and (d), Extracted mobility vs. charge density.

The mobility of graphene is calculated by using extracted charge density in Figure 3.13(b) as a function of sheet resistance. *DC* conductivity of graphene can be written as

$$\sigma_{DC} = ne\mu \tag{3.7}$$

Where n is the charge density, e is the electronic charge, and μ is the mobility of graphene. Since the σ_{DC} is the inverse of R_s and then the mobility is written as

$$\mu = \frac{1}{R_s ne} \tag{3.8}$$

By using the data from Figure 3.13(b) in (3.8), I calculate and plot mobility μ as a function of the sheet resistance R_s, Figure 3.13(c) and as a function of charge density n in Figure 3.13(d). Here, calculated mobility of graphene is electro-optical mobility of graphene rather than pure electronic mobility used in transistor technology. The sheet resistance vs. bias voltage is measured in the LCR meter and then we use transmission vs. wavelength for various bias voltages measured in FTIR to calculate the mobility of graphene. Data of both electrical and optical measurements are used to extract mobility of graphene so it is call as electro-optical mobility.

Chapter 4

Graphene-enabled electrically switchable radar absorbing surfaces

Microwaves are part of the electromagnetic spectrum with wavelengths that range from one millimeter to a meter. Radar and communication technologies use passive metallic surfaces to guide microwaves in the free space and resistive surfaces to absorb them [26, 27]. Although the source of microwaves can be controlled by electrical means, active control of microwaves in the free space has been a challenge due to the requirement of large area adaptive surfaces in microwave frequencies[28-33]. Microwave analogues of smart optical windows that enable electrically-tunable microwave reflection and transmission have been the subject of active research for many decades [28, 32, 34]. The key challenge is the ability to tune the interaction between microwaves and matter by electrical means. These interactions are mainly governed by dielectric response of the materials. Materials with tunable conductivity

[34, 35], permittivity [36] or permeability [37, 38] have been exploited for adaptive surfaces. Instead of controlling the bulk material properties, here we propose to control microwaves by tuning the density of free charges on a surface. Large area the two-dimensional crystal of carbon, graphene, allows us to test this approach and fabricate a new class of adaptive microwave surfaces [39, 40]. One can confidently argue that an atomically thin coating has negligible effects on the reflection of microwaves from a surface unless there are abundant free charges on it. Through electrostatic doping, we show that atomically thin layers can be used as a switchable radar absorbing surfaces. Graphene and carbon nanotube based composite materials have been used as resistive materials to absorb microwaves, however, to our knowledge they have not been used for active microwave surfaces [41-52].

Metals do not yield tunable electrical conductivity via external electric fields. This drawback prevents the uses of metals for adaptive microwave surfaces. Semiconductors can yield tunable surface charge density by means of metal-oxide semiconductor (MOS) structures [53], however, the metallic gate electrode covers the surface of semiconductor and screens the accumulated charges. Heating or illuminating a bare semiconductor surface with a light source can generate free carriers; but, these techniques are not practical for realistic device configurations. Electrically tunable materials such as ferroelectric materials [54, 55] and composite polymers [56, 57] have been studied for possible active microwave surfaces. Inability to fabricate these materials over large area and weak modulation of dielectric properties prevent realization of adaptive microwave surfaces. Another approach is to use distributed active circuit elements (diodes, transistors or photo-switches) integrated with passive metallic structures [58, 59]. External bias voltage or light source applied on these distributed circuit elements changes the effective length of metallic structures which yield limited control over the reflectivity of the surface. Moreover, micro-electro-mechanical devices and mechanical actuator have been used to control microwaves by mechanical means [60, 61]. Recently, graphene

provides new perspective to realize adaptive surfaces. The ability to control charge density on graphene enables new active terahertz devices for various applications such as switches [12], modulators [7, 8, 62-64], metamaterials [10, 65, 66], plasmonics [10, 67] and cloaking [65, 68]. A review by Sensale-Rodrigues et.al. [69] summarizes these recent developments in reconfigurable terahertz optoelectronics. The physical mechanism of these active THz devices is based on controlling intraband transitions of graphene.

In this paper, we implement the same idea to microwave frequencies to realize switchable radar absorbing surfaces. Due to the centimeter scale wavelength, adaptive microwave surfaces require challenging growth and device considerations. We show that, large area graphene capacitors, eliminate these challenges and provide electrically reconfigurable surfaces which would function as electrically switchable radar absorbing surfaces. Monoatomic thickness, tunable high mobility charged carriers together with the large area synthesis of graphene provide unique configuration for the realization of the adaptive microwave surfaces.

4.1.Adaptive Microwave Surfaces

Figure 4.1(a) shows a schematic representation of the device which functions as an adaptive microwave surface. The working principle of the device is based on the electrostatic tuning of high mobility carriers on graphene electrodes without using metallic structures. The device consists of two large area graphene electrodes on flexible polymer support and electrolyte medium between them. The cross sectional view of the device is shown in Figure 4.1(b). Application of a bias voltage between the graphene electrodes polarizes the electrolyte and forms ionic double layers on the graphene-electrolyte interface with opposite polarizations. These ionic double layers generate tunable high mobility free carriers (electrons and holes) on the graphene electrodes which can respond to microwaves. Reflection due to the electrolyte is

negligible, because the ions of the electrolyte have very low mobility, therefore they cannot influence the electric field of microwaves (Table 4-1).

	T%	R%	A%
PVC with tissue (without electrolyte)	99.47	0.02	0.51
1-Butyl-3-methylimidazolium hexafluorophosphate (soaked in tissue with PVC support)	95.72	0.11	4.17
1-Ethyl-3-methylimidazolium tetrafluoroborate (soaked in tissue with PVC support)	87.76	0.19	12.05
Methyl-trioctylammonium bis(trifluoromethysulfonyl) imide (soaked in tissue with PVC support)	99.20	0.02	0.78
H_2O (soaked in tissue with PVC support)	22.13	6.07	41.80
LiBOB in propylene carbonate (soaked in tissue with PVC support)	77.23	0.31	22.46
Undoped Si	37.71	25.47	36.82
Doped Si (5-10 Ω.cm)	29.80	19.38	50.82
Highly doped Si	0.03	73.29	26.68
Glass	39.53	48.41	12.06
ITO on glass	1.32	77.23	21.45
Multilayer graphene (~50 layers)	3.38	87.56	9.06

Table 4-1 Comparative microwave characterization of various electrolytes and substrate materials. Measured microwave (at 10.5GHz) transmission, reflection and absorption of various electrolytes and substrate materials.

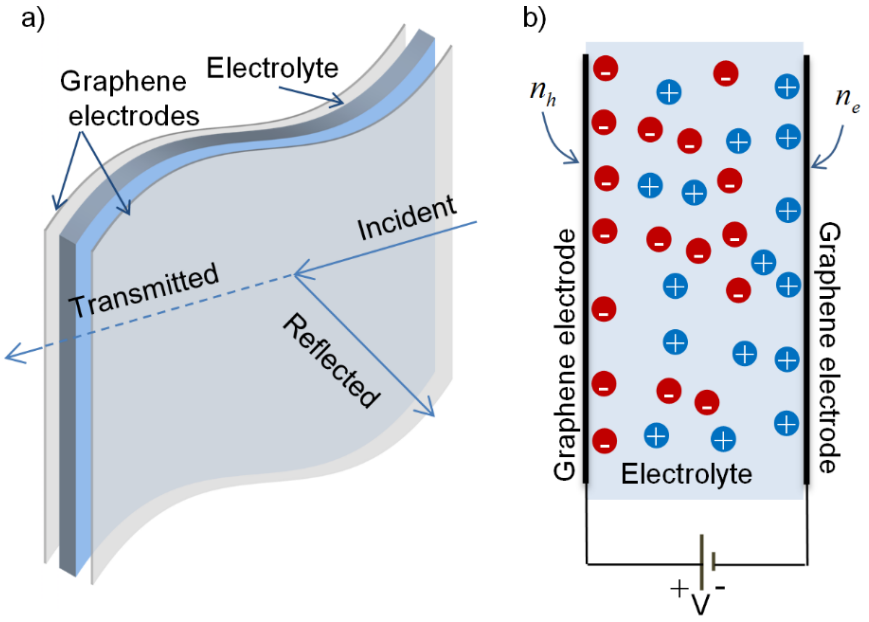

Figure 4.1(a) Schematic representation of the graphene-based adaptive microwave surfaces. The device consists of two large-area graphene electrodes transfer printed on a microwave-transparent PVC support and electrolyte between them. (b) Cross-sectional view of the device. Application of a voltage bias polarizes the electrolyte (ionic liquid) and forms ionic double layers on the graphene–electrolyte interface.

To fabricate this device, we synthesized large area graphene (20cm x 20cm) by chemical vapor deposition on ultra-smooth copper foils and then we transferred graphene on a microwave-transparent and flexible polyvinyl chloride substrate (PVC, thickness of 70µm, see Figure 3.1, Figure 3.2, Figure 3.3, Figure 3.4). We attached two graphene coated PVC films (graphene coated sides are facing to each other and separated by 50µm thick spacer) and filled the gap between graphene electrodes with ionic liquid (Diethylmethyl(2-methoxyethyl)ammoniumbis(trifluoromethylsulfonyl) imide, [deme] [Tf2N]) which works as an electrolyte with a wide electrochemical window of ±3.5V. Figure 4.2(a) shows the fabricated device with dimensions of 20cm x 20cm. This simple device architecture yields an unprecedented ability to

control charge density on large area graphene electrode which operates as a tunable metal. Electrostatic and electrochemical mechanisms are used to store charges at the electrode of the supercapacitors. In our devices, we used only electrostatic storage to prevent detrimental effects on single layer graphene. Redox reactions can damage the electrical continuity of the single layer graphene. Electrochemical storage can be used for multilayer graphene electrodes; however, multilayer graphene is not suitable for our purpose due to the lack of efficient modulation.

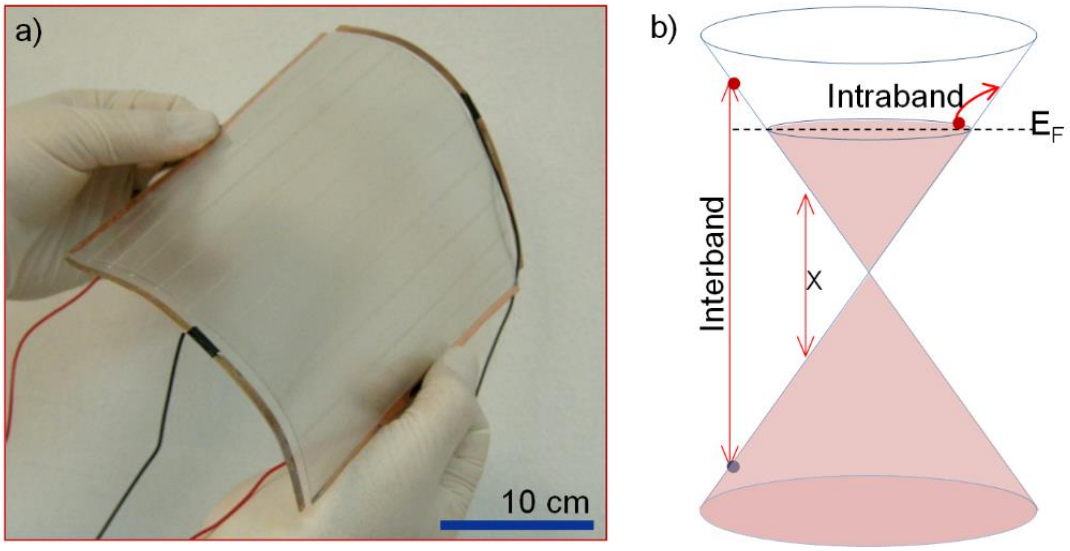

Figure 4.2 (a) Photograph of the fabricated device. (b) Representation of the electronic band structure of graphene and electronic transitions that defines the broadband optical response.

Notably, tunable charge density on large scale graphene enables us to control light-matter interaction in a very broad spectrum ranging from the visible to microwave frequencies [4, 5, 7, 69, 70]. Figure 4.2(b) illustrates the interband and intraband electronic transitions of graphene that define this broadband optical response. We calculated the optical absorption of single layer graphene with different

charge densities over a very broad spectrum covering from the visible to microwave (Figure 4.3). We can classify this spectrum into two sections based on interband and intraband transitions.

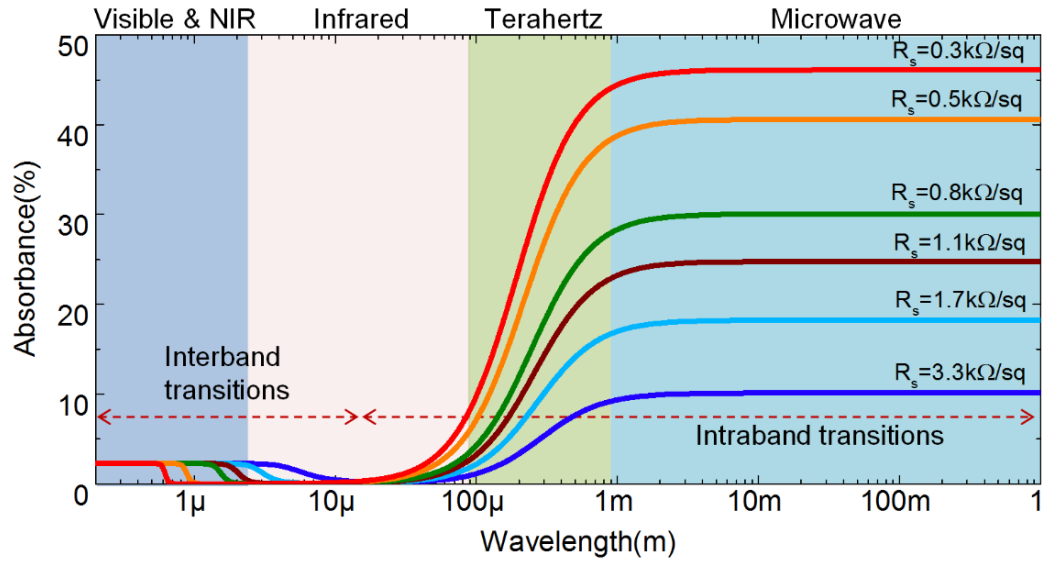

Figure 4.3 Calculated broadband absorption of a single layer graphene with different sheet resistance for the electromagnetic spectrum covering from the visible to microwave frequencies.

The optical response in the visible and near infrared is defined by the interband transitions which provide a constant optical conductivity which yield 2.3% broadband optical absorption and negligible reflection. This small absorption can be blocked via Pauli blocking that yields step like optical transmission spectra with a cut-off at $2E_f$. To obtain the charge density on graphene electrodes we measured the Fermi energy from the optical transmission spectra ($500 - 1100nm$ range, Figure 3.12 and Figure 3.13). Fermi energy of graphene electrodes scales with the charge density as $E_f = \hbar v_f \sqrt{\pi n}$ where v_f is the Fermi velocity ($1.1x10^8\ cm/s$) [71] and n is the charge density. Since ionic liquid electrolyte yields very efficient

electrostatic doping, the Fermi energies increase up to $1eV$ (Figure 3.12) at a bias voltage of $5V$. The extracted charge density on graphene electrodes varies between $0.5x10^{13}$ to $5.5x10^{13}$ $charge/cm^2$. The associated Fermi energies vary between $0.2eV$ to $1eV$. For longer wavelengths, however, interband transitions are blocked due to unintentional doping therefore, the long-wavelength optical response is due to intraband transitions which yield frequency dependent Drude like optical conductivity[70] of $\sigma(\omega) = \sigma_{DC}/(1 - i\omega\tau)$, where σ_{DC} is the low frequency conductivity, ω is the angular frequency of electromagnetic wave and τ is the electron scattering time. By tuning the low-frequency conductivity of graphene through electrostatic doping, we can obtain significant change in the absorption (as large as 50%) in the microwave frequency. This large broadband absorption has been predicted for ultrathin conducting films [24] and graphene [7]. The absorption due to intraband transitions rolls down at terahertz frequencies ($f_t \approx 1/\tau$) due to the electron scattering time of graphene. The electron relation time for CVD graphene is around $0.2ps$ [72] which corresponds a cut-off frequency of 5 THz. Therefore, we expect that the response of graphene supercapacitors should be flat in the microwave frequencies and rolls down in the THz frequencies [7, 8].

We measured the microwave reflection and transmission from our device at a frequency of $10.5GHz$ (wavelength of $2.8cm$). We used TE-polarized microwave transmitter with a power of $15mW$ and two receivers (Figure 4.4(a)). We applied an external voltage bias and measured the variation of the reflected (Figure 4.4(b)) and transmitted (Figure 4.4(c)) microwave power. At a bias voltage of $0V$, only 1.8% of the incident beam is reflected from the device. This small reflection is due to the residual charges and/or unintentional doping on the graphene electrodes. The PVC substrate and the ionic liquid have negligible microwave reflection ($< 0.1\%$, Table 4-1). As we increase the bias voltage, the reflection increases up to 20% at a bias voltage of $3.5V$. As the charge density on the capacitor increases, the transmitted power decreases from 76 to 36% because of enhanced reflection and absorption. The

extracted microwave absorption due to Joule heating ($A = 1 - T - R$ where T and R refers transmitted and reflected power) is given in Figure 4.4(d).

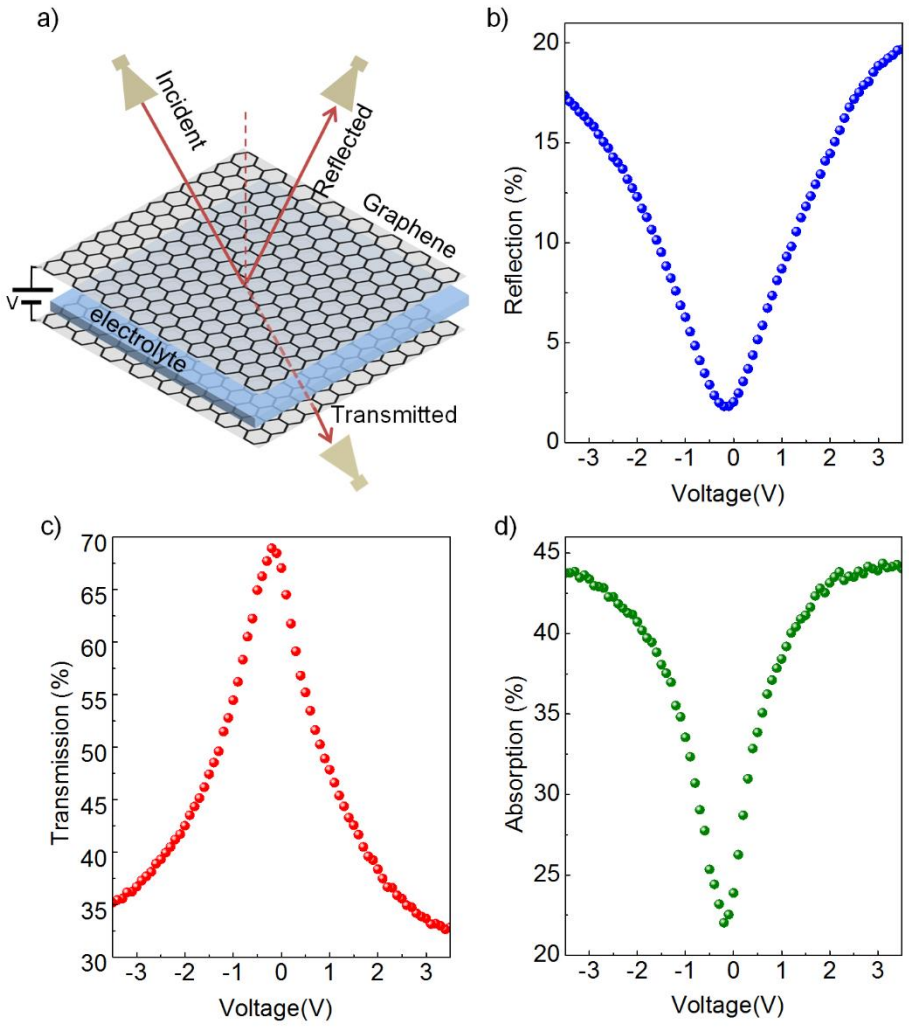

Figure 4.4 Microwave characterization of the adaptive microwave surfaces. (a) Experimental setup used for the microwave measurements. A microwave transmitter with a power of 15mW at 10.5 GHz and two receivers were used to measure the reflected and transmitted microwave power. (b, c) Measured intensity of the reflected and transmitted microwaves plotted against the bias voltage. (d) The extracted microwave absorption of the graphene capacitor as a function of bias voltage.

The microwave absorption of the graphene capacitor can be tuned between 21 to 45% of the incoming microwaves for the bias voltage range of 0 to $3.5V$. We observed a slight asymmetry in modulation of microwave at positive and negative voltages likely due to different ionic strength of anions and cations of the electrolyte. The sheet resistance of the graphene electrodes is a practical parameter to understand the microwave response of this device. Figure 4.5(a) shows the variation of the total resistance of the device as a function of bias voltage. The total resistance ($R^T + R^B$, T and B represents the top and bottom electrodes) reaches the peak value of $8k\Omega$ at the charge neutral point ($-0.1V$) and decrease down to $2.7k\Omega$ at a bias voltages of $3.5V$. After extracting the contact resistance ($R_c \sim 0.7k\Omega.cm$, Figure 3.7), we plot the measured values of the reflection, transmission and absorption of microwaves at $10.5GHz$ frequency, against the sheet resistance of the graphene electrode (Figure 4.5(b)). There are two mechanisms that cause the observed hysteresis in our devices. The first mechanism is the formation of electrical double layers and slow response of the electrolyte due to low mobility of the ions in the electrolyte. Hysteresis during charging and discharging is a common phenomenon in supercapacitors. The second mechanism is the electrochemical doping of graphene electrodes. When we apply relatively large voltage, which is close to the electrochemical window, the small leakage current (Figure 3.10) is inducing chemical doping on graphene which shifts the Dirac point. The shift in Dirac point during the voltage scan appears as a hysteresis in the microwave measurements. To get more insight, we calculated the coefficient of reflection and transmission of graphene electrodes for TE polarized electromagnetic waves by solving the Maxwell's equations for the capacitor geometry (two graphene electrodes and ionic liquid between them, see Chapter 2). We modeled graphene as a Drude metal with a frequency dependent conductivity $\sigma(\omega) = \sigma_{DC}/(1 - i\omega\tau)$, where σ_{DC} is the low frequency conductivity, ω is the angular frequency of electromagnetic wave and τ is the electron scattering time ($150fs$) [22].

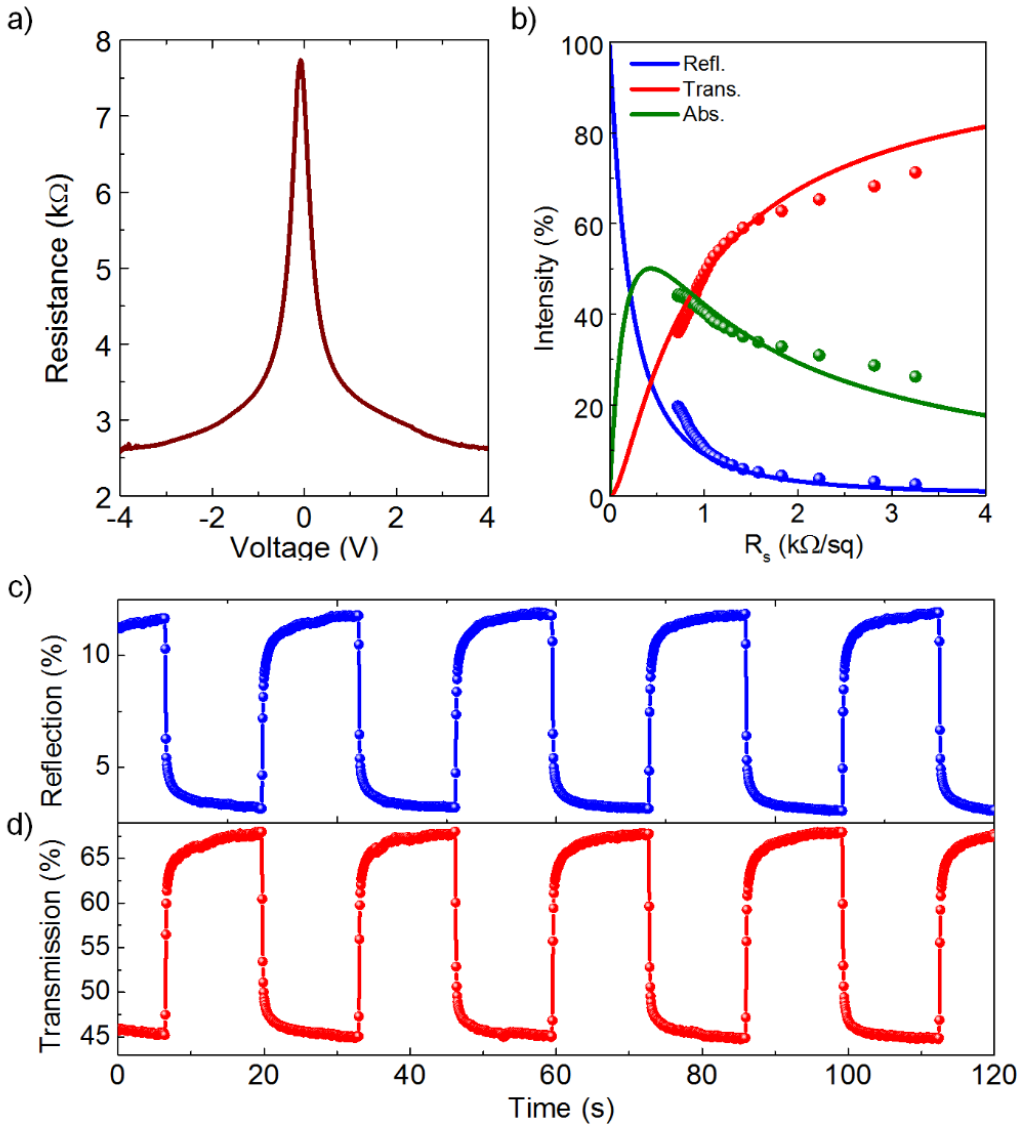

Figure 4.5 (a) Measured resistance of graphene electrodes (including contact resistance) as a function of bias voltage. (b) The experimental (scattered plot) and calculated (solid lines) microwave reflection, transmission and absorption are plotted against sheet resistance. (c, d) Real-time microwave reflection, and transmission, through the graphene capacitor during periodic charging and discharging. The RC response time of the capacitor is determined by the varying resistance of the graphene electrodes and the total capacitance of the device. The extracted response time of graphene capacitor with dimensions of 8x8cm^2 is around 300ms.

	Dielectric Constant	Dielectric Strength (V/mil)	Loss Tangent	Volume resistivity (Ohm/cm)
Polyvinylchloride (PVC)	3.2	725	0.00033 @ 3 GHz	$5.4\ 10^{15}$

Table 4-2 Electrical properties of the PVC substrate. [25]

At $10.5GHz$, the conductivity is very close to σ_{DC} obtained from the transport measurements. The results of the electromagnetic model is plotted in Figure 4.5(b) (line plot) against the sheet resistance of the graphene layers. As the sheet resistance of graphene increases, the microwave reflection drops sharply whereas the microwave transmission increases. Interestingly, the microwave absorption reaches a maximum of 50% at the sheet resistance of 430Ω and drops gradually as the sheet resistance increases further. We observed a good agreement between the experiment and the electromagnetic model. The slight deviation at large sheet resistance (around Dirac point) is likely because of inhomogeneous charge density on large area graphene owing to the charge puddle formation [73]. The variation of the microwave reflection can be understood by a simple transmission line model (see section 2.2 and Figure 2.8). As the sheet resistance of graphene varies, the characteristic impedance of the surface changes. The dynamic range of the microwave surface is limited by the two main effects: (1) the electrochemical window of the electrolyte which limits the maximum charge density on graphene electrodes, (2) the unintentional doping on the graphene which limits minimum charge density. However, due to the lack of a band gap, there is always some degree of charges on graphene electrodes at unbiased case. A graphene like material with electronic band gap (carbon nanotube networks, MoS_2 or other 2D materials) could provide better control of the minimum charge density. Thermal effects due to the absorbed microwaves on graphene electrodes, is another

limiting factor for high microwave powers. The thermal effects can be optimized by controlling the substrate material and the geometry.

To probe the switching characteristics of the active microwave surface, we monitored the reflected and transmitted microwave power as the bias voltage varies repeatedly between 3 and $0V$. Figure 4.5(c) and Figure 4.5(d) shows the time trace of the reflected and transmitted power, respectively. The graphene capacitor behaves like a nonlinear RC circuit (Figure 3.9, Figure 3.10, Figure 3.11). The response time of the device is characterized by the resistance of graphene electrodes and the capacitance of the device. We extracted the response time of $300ms$ for a device with dimensions of $8x8cm^2$. This number agrees well with averaged time constant $\tau = RC = 330ms$ calculated from the average capacitance $(\sim 100\mu F)$ and resistance $(\sim 3.3k\Omega/sq)$ obtained from the transport measurements. The time constant of the device can be reduced by increasing the charge mobility of graphene electrodes (i.e. increasing the grain size of graphene flakes) or ionic mobility of the electrolyte. Using an electrolyte with high ionic conductivity can improve the response time, however, there is a trade of between the ionic mobility and electrochemical stability. The ionic liquid electrolyte [deme][Tf2N], provides the optimum performance (see Table 4-1) [74].

4.2.Switchable radar absorbing surfaces

After studying the microwave response of the graphene capacitors, we would like to demonstrate electrically switchable radar absorbing surfaces. The maximum microwave absorption of single layer graphene is limited to 50% defined by the Maxwell's equations [7, 24]. To reduce the microwave reflection from the surface, we demonstrated a resonant device architecture (Figure 4.6(a)) which includes the graphene capacitor and a flat metallic surface, place at a distance of quarter of the wavelength ($d = \frac{\lambda}{4}\cos(\theta)$, where, λ is the wavelength and θ is the incidence angle).

This configuration is knows as Salisbury screen previously used for enhancing microwave absorption of resistive materials [30] and graphene at infrared and terahertz frequencies [8, 75]. Figure 4.6(b) and Figure 4.6(c) show the pictures of the front and back side of the resonant device.

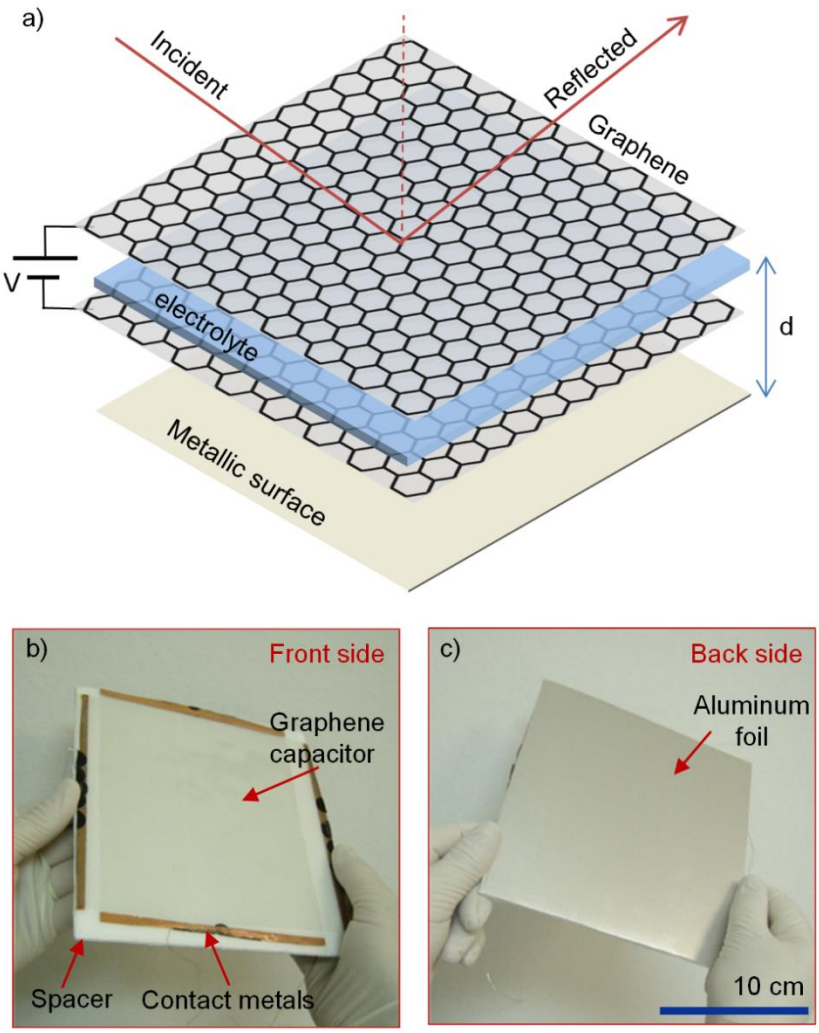

Figure 4.6 Graphene based switchable radar absorbing surfaces. (a) Schematic representation of the resonant device including the graphene capacitor and metallic surface placed at a distance of quarter-wavelength. (b, c) Photographs of the front and the back side of the fabricated device.

Surprisingly, locating a flat metal at a quarter wavelngth distance yields very high reflection suppression at high doping concentration on graphene. The variation of the microwave reflection of this device is shown in Figure 3d. At 0V, the reflection is maximum at 60% (-3 dB) and as we increase the bias voltage, the reflection diminishes entirely (< - 45 dB, Figure 4.7(a)). At 3V, the Fermi energy and charge density on graphene electrodes are around 0.95eV and $5.5 \times 10^{13} cm^2$, respectively. The time traces of the reflection (Figure 4.7(b)) show a remarkable reflection suppression ratio of around 50dB which is limited by our detector. When the gap between the graphene electrodes and the metallic surface is a quarter of the wavelength, the reflection from the metallic surface forms a standing wave with the antinodal plane (maximum lateral electric field) which is on graphene electrode. Therefore, the distance between the graphene electrodes and the metallic surface defines the modulation depth $M = (R_{on} - R_{off})/R_{on}$, R_{on} and R_{off} represents the reflected power at the on- and off-state). Figure 4.9(b) shows the variation of the modulation depth with the distance. Interestingly, when the distance is half-wavelength (graphene electrodes are at the nodes of the standing wave), we do not observe any modulation in the reflectivity, because the electric field on the graphene is zero (Figure 4.9(a), Figure 4.10). Although the resonance behavior varies with the incidence angle, this device yield reasonably large modulation for broad incidence angles (Figure 2.11, Figure 2.12, Figure 4.11).

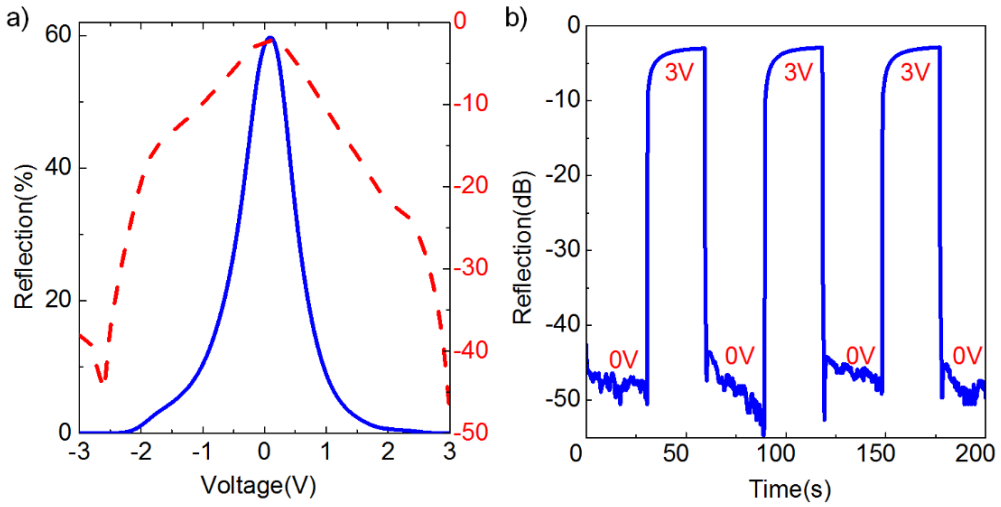

Figure 4.7 (a) Measured microwave reflection at 10.5 GHz plotted against the bias voltage. The red curve shows the reflection in decibel. (b) Real time reflection from the device during periodic charging and discharging. The device yields around 50 dB reflection suppression ration.

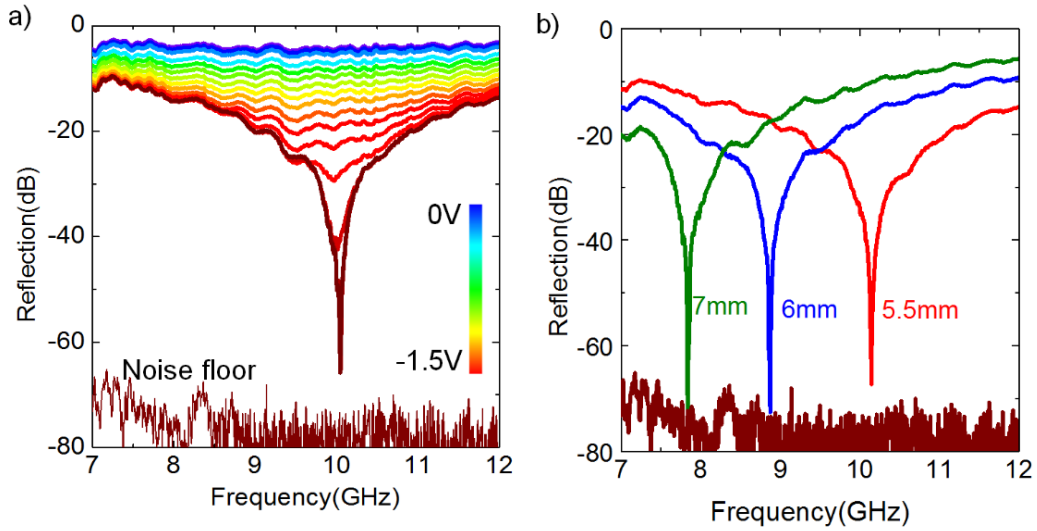

Figure 4.8 (a) Broad–band reflection spectrum from the device at various bias voltages. The noise floor is at -80dB. (b) Microwave reflection from the device plotted against the bias voltage and the spacer thickness which defines the distance between the graphene electrodes and metallic surface.

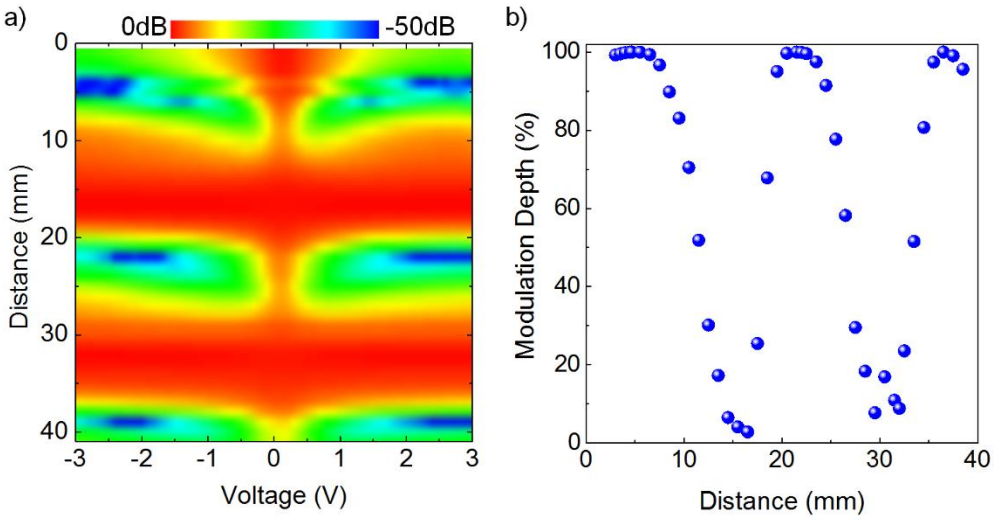

Figure 4.9 (a) Variation of the modulation depth of the resonant device with the spacer thickness. When the graphene is at the antinodes, the modulation is around 100% whereas, at the nodes the modulation is close to zero. (b) Broadband reflection spectra from the device for three different spacer thickness.

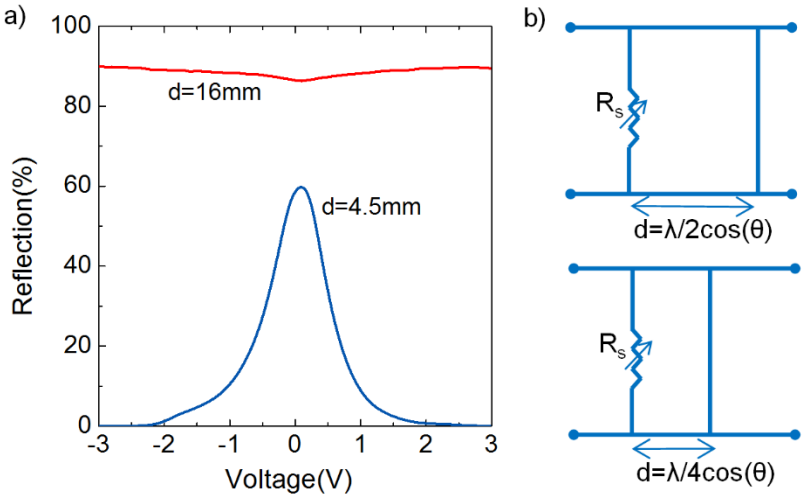

Figure 4.10 (a) Reflection vs. voltage for two different distances. (c, d) Transmission line model for the resonant surface. Graphene electrodes are represented by variable resistance and the metallic surface is represented by a line which shorts the ports.

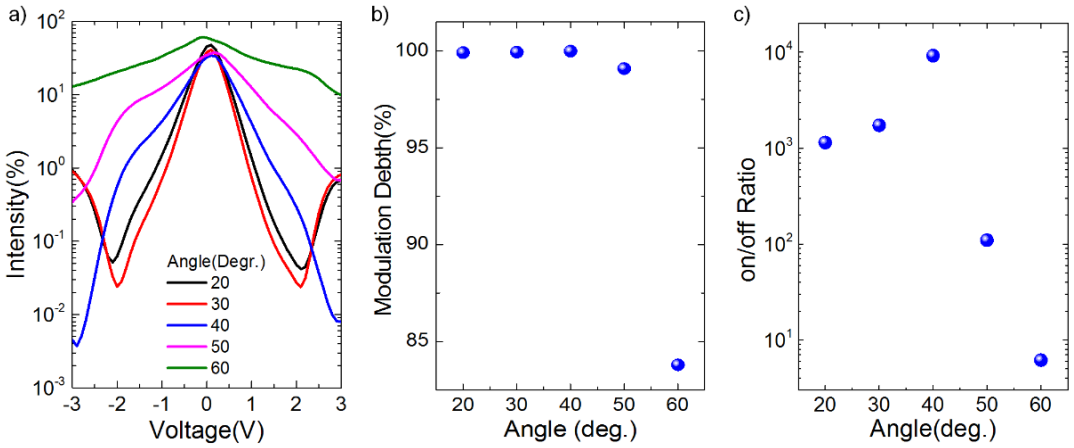

Figure 4.11 (a) Variation of the microwave reflection from the surface of the resonant device with different incidence angle (inset shows the incidence angle). (b) The modulation depth and (c) on-off ratio plotted against incidence angle.

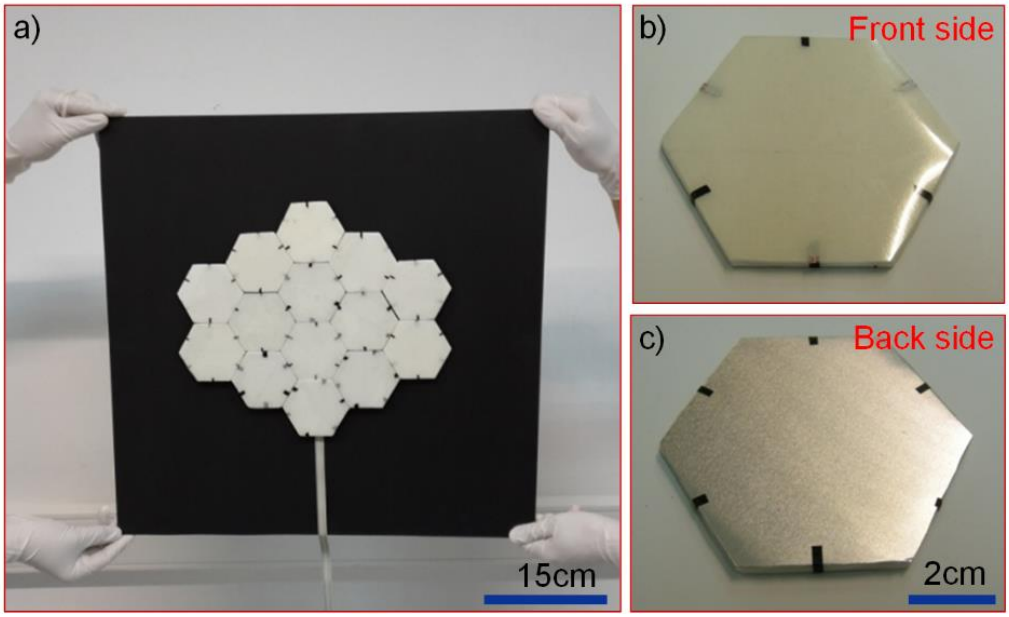

Figure 4.12 (a) Photograph of the pixelated microwave surface consist of 14 individually addressable hexagonal shaped cells. (b, c) Photograph of the front and back side of an individual cell.

Next, we would like to discuss some device strategies to cover large area and nonplanar surfaces. Since microwave has centimeter scale wavelengths, operating these devices over a large area is essential for realistic applications. For this purpose, we developed pixelated surfaces formed by individually addressable hexagonal shaped devices (Figure 4.12). Similar type of multipixel devices has been demonstrated in THz frequencies [65, 76-78]. The individual device (Figure 4.13(a)) consists of a graphene capacitor, a solid spacer (2.5mm thick cardboard) and metallic back surface (aluminum foil). The microwave reflection from an individual device is shown in Figure 4.13(b). At 1.5V, the reflection decreases substantially with a suppression ratio of 1000. Figure 4.14 shows the microwave reflectivity maps of the individual pixel at various voltages. The strong reflection at 0V diminishes at 1.5V with slight background reflection due to the contact metals. Then we imaged 4 cells (scan area is limited by our scanner) at different voltage configurations. When we applied 0V to the cells we observed reflection from all devices. However, the reflectivity of an individual cell can be suppressed at 3V. Figure 4.15 shows reflectivity maps at different voltage configurations. The variation of the reflection within the single cell is due to the reflection from the edges and contact metals. These pixelated surfaces would yield various possibilities for active camouflage systems by shaping the reflectivity pattern from the multipixel adaptive surface.

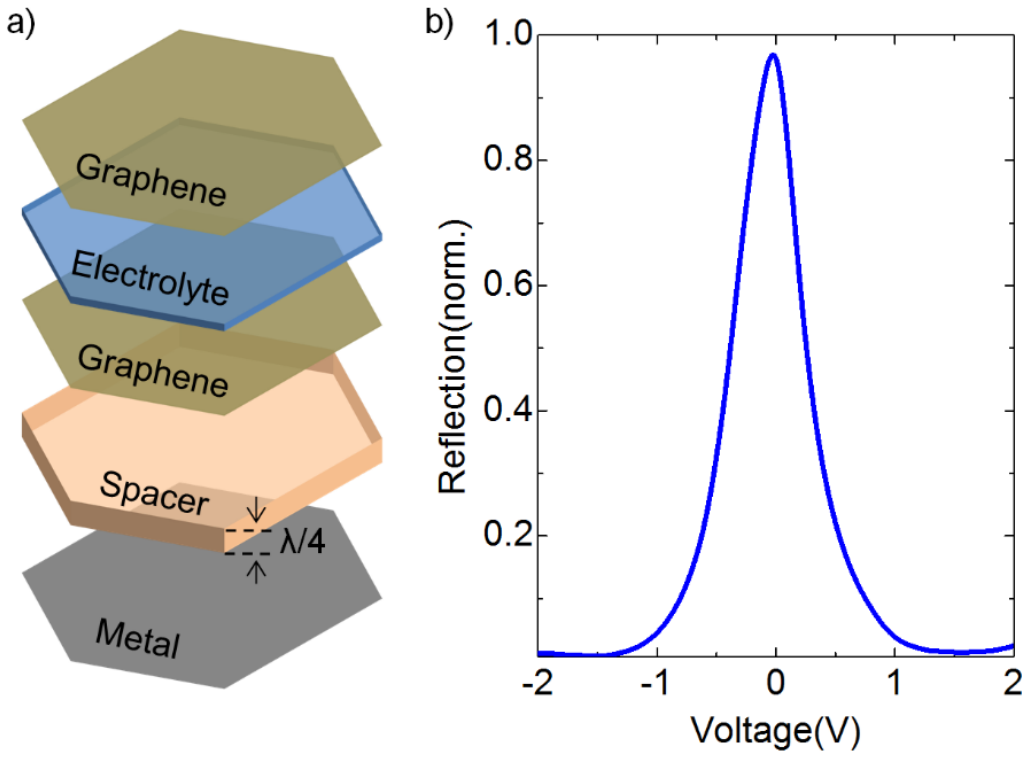

Figure 4.13 (a) Exploited view of the structure of an individual cell showing the layers. (b) Microwave reflection of an individual cell at 10.5 GHz.

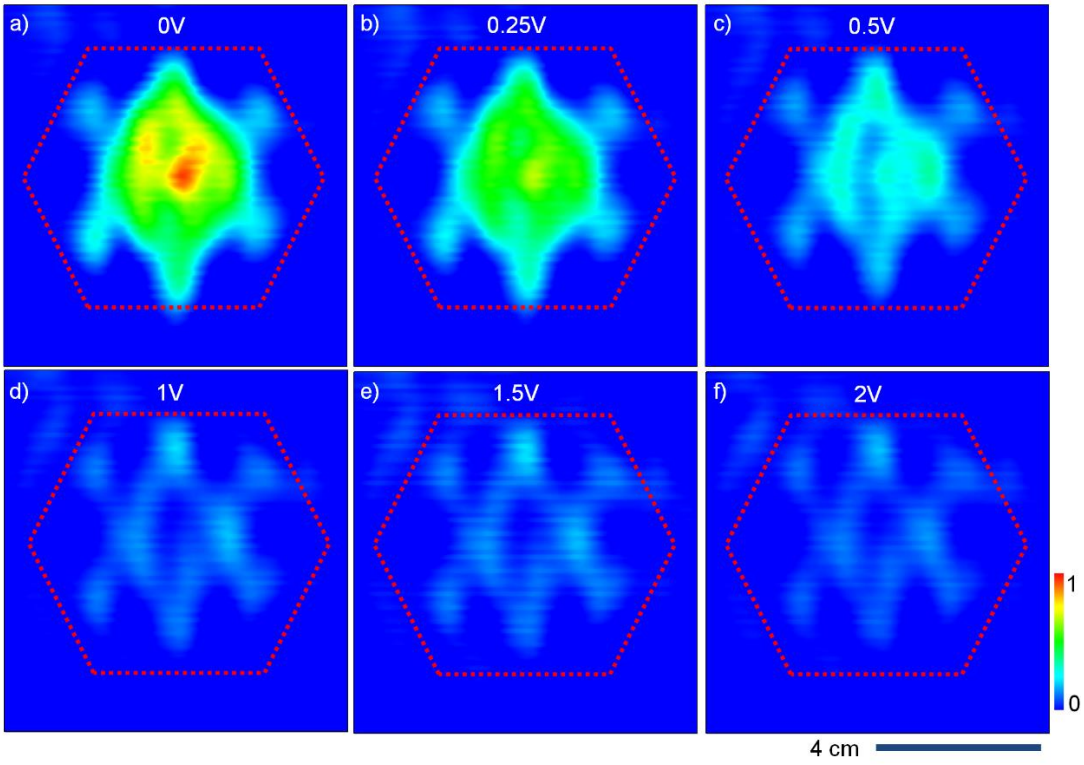

Figure 4.14 Scanning microwave reflection images of an hexagonal cell at different bias voltages.

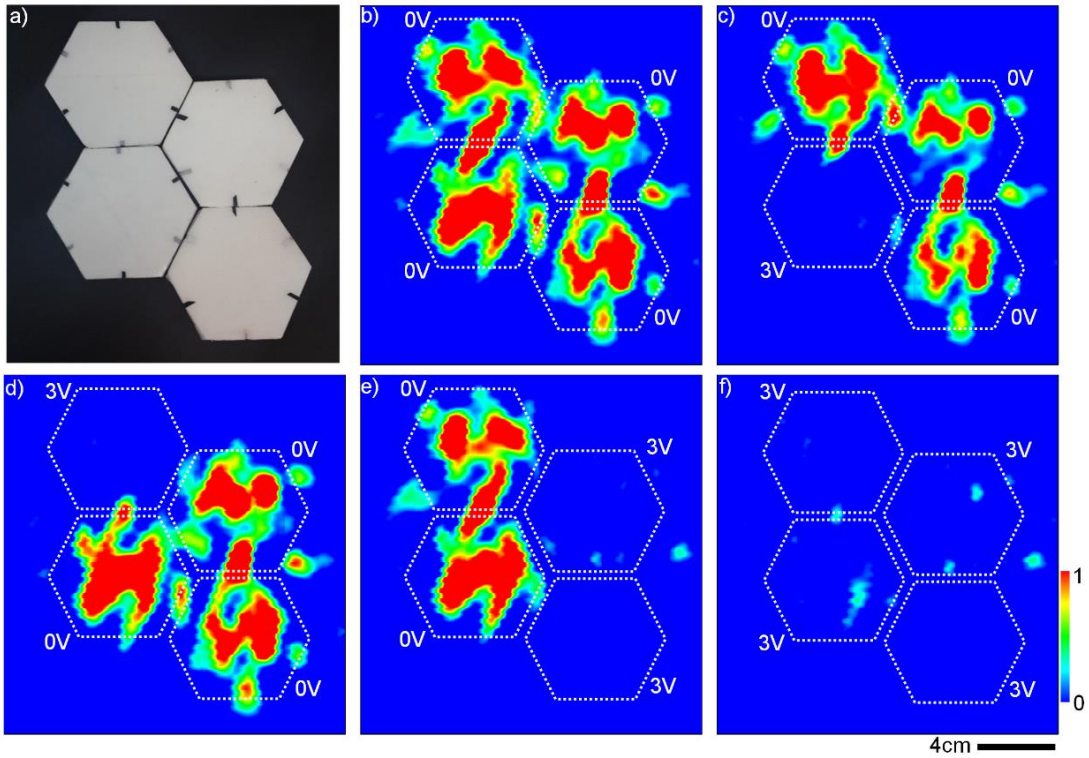

Figure 4.15 Scanning microwave reflection of 4 cells with different voltage configurations.

Furthermore, graphene electrodes on flexible polymer substrates allow us to fabricate non-planar adaptive microwave surfaces as well. Figure 4.16(a) and Figure 4.16(b) shows concave and convex spherical surfaces formed by multiple individually addressable hexagon- and pentagon-shaped cells. The reflectivity of individual cell (structure shown in the Figure 4.12 and Figure 4.13) provide reflection suppression of 1000 for TE polarization. To test an extreme case, we fabricated a cylindrical surface with radius of curvature of 2.6cm (Figure 4.16(c)). Then we placed a metallic cylinder inside the device and measured the reflection from surface at various bias voltages. Figure 4.17(a) shows the variation of the microwave reflection from the cylindrical surface as a function of voltage. Even for a large curvature, the microwave reflection is suppressed by 45dB at 2V. This modulation is

slightly less than the flat resonant surface due to the curvature of the device. The polar plot in Figure 4.17(b) shows the angular dependence of the reflectivity (at 0 and 2V) of the cylinder obtained by rotating the cylinder around its axis. The polar plot represents tunable radar cross section of the metallic cylinder. We anticipate that the ability to cover non planar objects with these active microwave materials will enable new possibilities for microwave cloaking [65, 68].

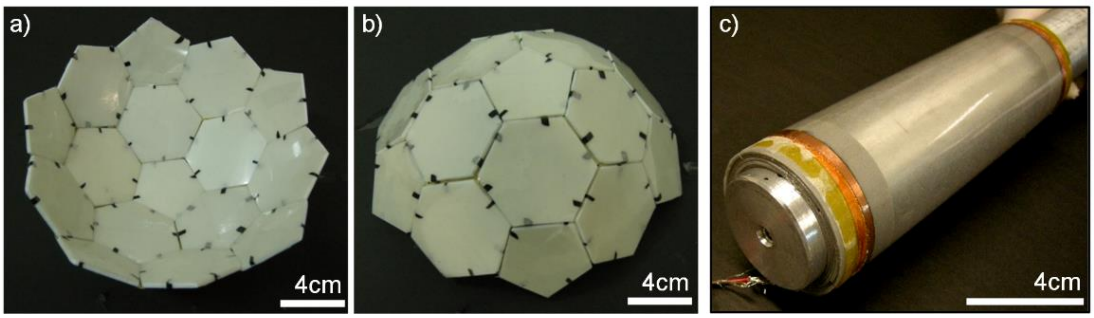

Figure 4.16 Non-planar adaptive radar absorbing surfaces. (a, b) Photograph of concave and convex hemispherical surfaces formed by individually addressable hexagon and pentagon shaped adaptive cells. (c) Photograph of the cylindrical-shaped switchable radar absorbing surface placed around a metallic cylinder. The diameter of the cylinder is 4.2 cm.

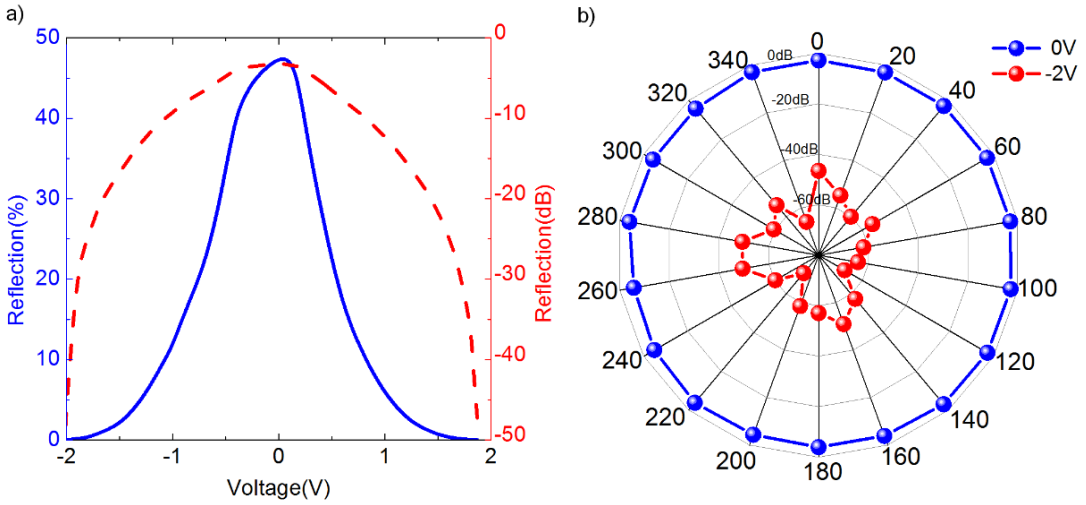

Figure 4.17 (a) Reflection from the cylindrical surface containing a metallic cylinder as a function of bias voltage. (b) Orientation dependence of the normalized reflection from the surface at 0 and 2V, respectively. At 2V the reflectivity is suppressed by 50dB for all directions. The variation of the intensity on the off-state is due the variation of the distance between the graphene electrodes and metallic cylinder.

4.3.Discussion

In summary, we demonstrated a new class of adaptive microwave surfaces using large-area graphene capacitors. We show that graphene electrodes can operate as a tunable Drude metal at microwave frequencies owing to the high mobility carriers whose density can be tuned by electrostatic doping. Interestingly, this simple device structure yields unprecedented ability to control electromagnetic waves in a very broad spectrum from microwave to the visible spectra. Combining this ability with various device architectures, we demonstrated electrically switchable radar absorbing surfaces with reflection suppression ratio of 50dB with operation voltages less than 5V. Furthermore, we fabricated various adaptive surfaces including pixelated and nonplanar surfaces. These electrically switchable radar absorbing surfaces provide technological advantages over the passive microwave absorbers.

Our benchmarking studies (see Table 4-3 and Table 4-4) show that the key attributes of these adaptive microwave surfaces are; the simplicity of device architecture, broadband operation, the mechanical flexibility and potential for low material cost. We believe that these adaptive microwave surfaces will open a new chapter for active camouflage systems which could find immediate applications in radar technologies. Furthermore, integration of these adaptive surfaces with metamaterial could yield tunable adaptive cloaking in microwave frequencies.

Type	Material	Reflection Loss	Band width	Thickness	Flexibility	Reference
Our device	**Graphene**	**70 dB (tunable)**	**7-12 GHz**	**0.2 mm**	**+**	**This study**
Pyramidal Absorbers	Polyurethane absorber	6dB at 0.08 GHz 50dB at 40 GHz	0.08 to 40 GHz	6.4cm	+	Lindgren
	Polyurethane absorber	20dB at 0.08 GHz 50dB at 50 GHz	0.08 to 40 GHz	152cm	+	Lindgren
	Polyurethane Wedge absorber	30dB at 0.5 GHz 47dB at 50 GHz	0.5 to 50 GHz	46cm	+	RaMayes Lindgren
	Polyurethane Convoluted absorber	25dB at 3 GHz 50dB at 30 GHz	3 to 30 GHz	10.2cm	+	RaMayes
	High power honeycomb absorber	30dB at 0.5 GHz 45dB at 45 GHz	0.5 to 18 GHz	61cm		RaMayes
	Ferrite tile wedge absorber	20dB	0.03 to 18GHz	6cm	-	RaMayes
	Cascade absorber	30dB 20-40GHz 20dB 30MHz-2GHz	30MHz to 40GHz	95cm	-	RaMayes
	Polyethylene absorber	30dB at 0.3GHz 50dB at 110GHz	0.3-110GHz	100cm	+	RaMayes
	Ferrite Styrofoam absorber	25dB at 0.07GHz 40dB at 40GHz	0.07 to 40 GHz	130cm	-	RaMayes
Flat Absorbers	Polyurethane foam	20dB	>0.6GHz	11.4cm	+	RaMayes
	Reticulated Foam Absorber	20dB	>3GHz	5.08cm	+	RaMayes
	Honeycomb absorber	15dB at 6 GHz 20dB at 18GHz	6 to 18 GHz	2.54cm	NA	RaMayes
	Ferrite tile flat absorber	15dB at 30MHz 40dB at 200MHz	30MHz to 1 GHz	0.6cm	-	RaMayes
	Walkway absorbers	20dB at 250MHz 40dB at 30GHz	0.25-30 GHz	61cm	NA	Microwave Vision Group
	Tuned Frequency Absorber	20dB	8-12 GHz	0.45cm	NA	Microwave Vision Group
	Flat laminated absorber	20dB at 2Ghz 45dB at 3.5GHz	2-6 GHz	5.7cm	+	Lindgren
	Flat laminated absorber	10dB at 8GHz 25dB at 10GHz 15dB at 18GHz	8-18 GHz	2.9cm	+	Lindgren
	carbonyl-iron/epoxysilicone resin	42dB at 10.3GHz	-	0.2cm	-	[79]
	carbon nanobelts carbon/Fe–Cu hybrids	22dB at 12GHz	-	0.75cm	-	[80]
	carbonyl iron and barium ferrite	27dB at 12GHz	-	0.4cm	-	[81]

Table 4-3 Comparison of commercial microwave absorbers with our devices.

Type	Material	Reflection Loss	Reference
Composite Absorbers	MWCNTs with Fe_3O_4 and Fe	-90dB	[79]
	Ag in epoxy	-46dB	[80]
	Polyaniline and nano-ferrite	-50dB	[81]
	MWCNTs with Viton	-42dB	[82]
	Graphite-novolac phenolic resin	-53dB	[52]
	Crystal of $BaFe_{12}O_{19}$	-54dB	[83]
	Glass-Epoxy with Carbon Black	-54dB	[84]

Table 4-4 Non-commercial (research type) microwave absorbers

Chapter 5

Electrically switchable metadevices

Metamaterials have been a powerful tool to control and manipulate electromagnetic waves and their interactions with matter [33, 85, 86]. Integration of passive metamaterials with a variety of tuning mechanisms has been examined to generate active metadevices that have novel functionalities [87-90]. Based on the tuning mechanisms, these active metadevices can be classified into three general categories; circuit-, material- and physical-based metadevices [91]. The circuit-based metadevices use variable capacitors or switches to alter the lumped elements of the equivalent circuit. For instance, the reverse bias voltage applied on a varactor integrated on a split ring resonator changes the effective capacitance of the equivalent circuit [92-95]. Material-based metadevices rely on controlling bulk material properties such as permittivity, permeability or conductivity of the individual unit cell under an external stimulus [90, 96-101]. The conductivity of semiconducting material deposited in the split gap can be tuned by illumination and thereby alters the resonance frequency of the metamaterial. Similarly, interconnected metamaterials fabricated on a semiconductor surface, were used to tune the depletion area which alters the free carrier absorption [102, 103]. On the other hand, physical-metadevices

tune their response by changing their shape or relative position of sub-components (such as split gap) [104-108]. For example, micro electro mechanical (MEMs) based devices can tune the resonance frequency of metadevices in terahertz spectra [106]. Although these devices provide some degree of tunability, their performances are limited to narrow spectra with a small dynamic range due to the material and fabrication limitations. These technologies would benefit greatly from a material that yields large tunability over broad spectra. None of the existing materials provide these challenging requirements. Furthermore, the requirement for electrically controlled tunability places another challenge for practical applications of metadevices.

2-dimentional crystals provide new perspectives for reconfigurable smart surfaces that can be used for the realization of electrically tunable metadevices [10, 64, 69, 109, 110]. The thickness of 2D crystals is much shorter than the effective wavelength and, therefore, their electromagnetic response solely originates from the charge carriers. Recent studies have shown that tuning the density of high mobility free carriers on graphene yield an unprecedented ability to control light-matter interaction over a very broad spectra ranging from visible to microwave frequencies [70, 111]. By engineering the shape or doping level, the plasmon frequency of graphene can be tuned in IR and THz frequencies [10]. In another approach, graphene is coated on a metamaterial [12, 112] or optical antennas [113, 114] to yield electrically tunable metadevices. Tuning the charge density alters the effective dielectric constant of the medium. However, these devices are not suitable for practical application due to limited tunability [115]. Recently, we discovered a simple device structure consisting of an electrolyte medium sandwiched between two large area graphene electrodes. This geometry permits an efficient mutual gating between two graphene electrodes that yield charge densities on the order of 10^{14} cm^{-2} [5]. Using this supercapacitor structure, we fabricated various optoelectronic devices including optical modulators [5, 72], electro chromic devices [6] and switchable radar

absorbing surfaces [116]. In this chapter, using graphene supercapacitors incorporated with metallic split ring resonators, we demonstrated a new type of electrically controlled metadevices. These metadevices are based on tunable high mobility free carriers on graphene to introduce electrically tunable dissipation in the resonator capacitively coupled to the graphene electrodes.

5.1.Electromagnetic modelling

Integrating split ring resonators (SRR) close proximity of graphene surface yields a new type of hybrid metamaterial whose resonance can be tuned by various means. Previous attempts to integrate graphene with metamaterials yield very limited modulation in infrared and terahertz frequencies. Here, we use a different approach using microwave metamaterials capacitively coupled to large area graphene which yields a substantial tunability. Figure 5.1(a) shows the schematic drawing of this hybrid structure. The presence of graphene in close proximity of the SRR introduces additional electrical losses due to the sheet resistance of graphene. The equivalent small signal model of the hybrid structure is shown Figure 5.1(b). The ring and split gap provide the inductance, *L*, and the capacitance, *C*, respectively. The resistor, *R*, models the dissipation on the metal due to the electrical and radiation resistance. In our design, the SRR is capacitively coupled to graphene ($C_c = \varepsilon\varepsilon_0/d$, the coupling capacitance, ε is the dielectric constant of the medium and ε_0 is the free space permittivity). The graphene layer can be modeled by the sheet resistance ($R_G = 1/\sigma(n)$, where $\sigma(n)$ is a charge dependent sheet conductance of graphene) and quantum capacitance ($C_q = 2e^2\sqrt{n}/\hbar v_F\sqrt{\pi}$ where e is the elementary charge, v_F is the Fermi velocity) of the graphene electrodes. The quantum capacitance of unintentionally doped graphene layer (C_q~$0.5\mu F/cm^2$) is much larger than the serial coupling capacitance (C_c~$5pF/cm^2$) and, therefore, in the small circuit model we can neglect its contribution.

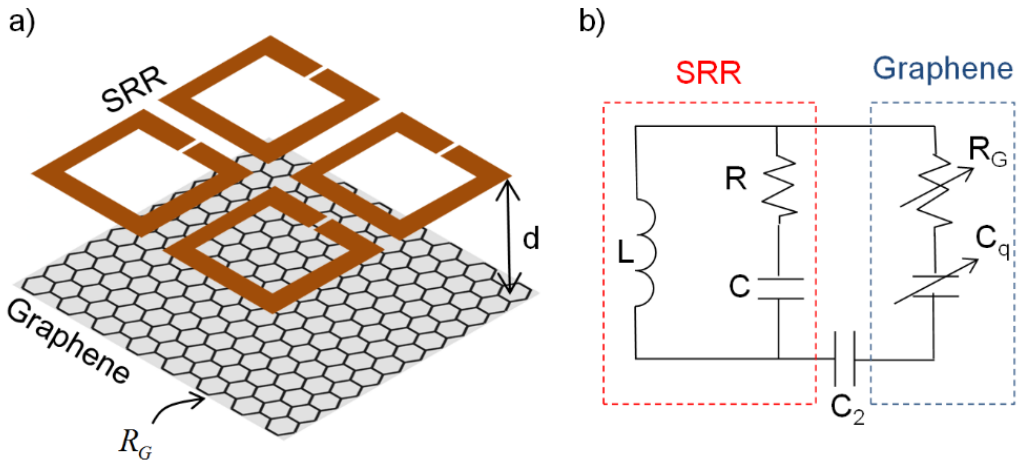

Figure 5.1 Tunable graphene-SRR hybrid metamaterial: a) Schematic representation of the hybrid metamaterial consisting of split ring resonator capacitively coupled to the graphene layer. The capacitive coupling is defined by the SRR-graphene separation, d. b) Small signal equivalent model of the graphene-SRR hybrid metamaterial. SRR is represented by the L, R, C lump circuit elements; the graphene layer is modeled by the variable sheet resistance, R_G and quantum capacitance, C_Q. C_c models the capacitive coupling.

We can tune the electrical resonance of the metamaterials by altering the SRR-graphene spacing or by tuning the charge density. First, we would like to understand the tunability of the resonance of the hybrid structure, using finite element analyses and then we will present the experimental realization of the proposed metadevices. Finite Element Method (FEM) simulations were performed on COMSOL Multi-Physics software package. The graphene layer is modelled as a transient boundary condition with parameterized conductivity function in Electromagnetic Waves and Frequency Domain pack. The low frequency limit of the conductivity is a function of DC conductivity and thickness of the graphene layer. The electrical thickness of the graphene layer is taken as 0.3 nm. Meta-material is

modelled with Floquet periodic boundary condition in lateral directions. The electrical properties of copper are introduced with perfect electrical conductor boundary condition. In the transverse direction, the port boundary conditions are employed for injecting EM waves and reading polarization dependent power. For the simulations, we used unintentionally doped graphene with sheet resistance of 3kΩ and varied the SRR-graphene distance from 2.0 mm down to 0.05 mm. The variation of the calculated transmittance spectrum ($|S_{21}|^2$) with the SRR-graphene spacing is given in Figure 5.2(a). The presence of a free carrier on graphene permits the damping of the resonance. This additional dissipation changes the resonance transmission of the metamaterial. For a spacing of 2 mm, SRR yield a -50 dB transmittance at the resonance. As the spacing decreases, the resonance transmittance varies from -45 dB (d=2 mm) down to -8 dB (d=0.068 mm). We also observed a slight change in the resonance frequency from 15.4 to 14.3 GHz. controlling the sheet resistance of graphene with electrostatic doping, yields an electrical means for tuning metamaterial. We calculated the transmittance spectra by altering the sheet resistance of graphene at a fixed distance (Figure 5.2(b)). The resonance transmittance is tuned from -42 dB down to -15 dB by tuning the sheet resistance from 10 kΩ to 0.5 kΩ. The quality factor of the resonance drops due to enhanced dissipation. The simulation results suggest that metamaterial placed at a distance of 0.3 mm away from graphene yield the largest modulation. We observe an opposite behavior (decrease in the transmittance) at the off-resonance frequencies. The decrease of transmittance at off-resonance frequencies is due to enhanced reflection from the graphene surface.

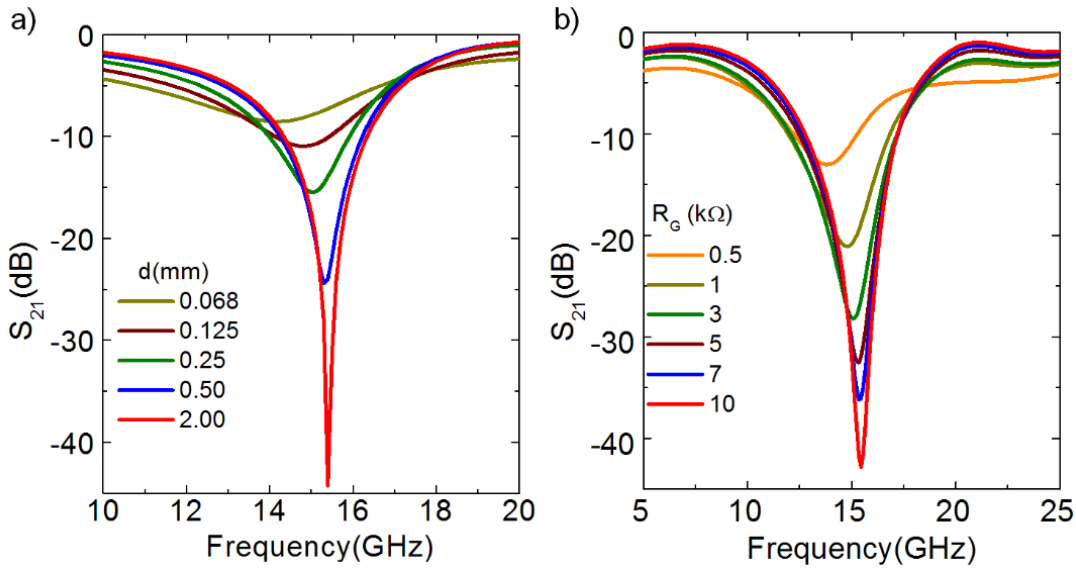

Figure 5.2 Simulated S_{21} values for a graphene-SRR hybrid metamaterial: a) Calculated transmittance spectra for various graphene-SRR distance values with 3kΩ sheet resistance of graphene. b) Calculated transmittance spectra for various sheet resistance of graphene (10 to 0.5 kΩ) at graphene-SRR distance of 0.5 mm.

5.2.Fabrication of graphene metadevice

After understanding the basic device considerations, we fabricated the proposed electrically switchable metadevices. The technical challenge for graphene based microwave devices is the requirement of large area devices due to the centimeter scale wavelength (i.e. λ= 3 cm at 10 GHz). The ability to synthesize large area graphene with chemical vapor deposition on copper foils enables us to realize the proposed microwave metadevices [117]. Figure 5.6(a) shows the schematic drawing of the device consisting of an ionic liquid electrolyte sandwiched between two large area graphene electrodes. The picture of the fabricated device is shown in Figure 5.6(b). Graphene electrodes were synthesized on copper foils using the chemical vapor deposition system and then transferred onto flexible PVC substrates using hot

lamination technique. The metallic SRR were fabricated on PVC by printing the SRR shapes on 10 μm thick copper foil followed by chemical etching of copper as explained in Figure 5.3. The transferred graphene grown copper and etched SRR arrays are laminated with multiple PVC layer by using a hot laminating machine as shown in Figure 5.4. The number of PVC layer between SRR arrays and the graphene layer determines the distance between them. After cutting the laminated graphene-SRR stack, graphene grown copper is etched in a 5mM $FeCl_3$ aqueous solution for 10min as shown in Figure 5.5. We use a thin layer of tissue as a spacer between two graphene electrodes in a metadevice. We first put tissue on graphene electrode on which the SRR array is laminated and then we drop an ionic liquid on the tissue. To finalize the fabrication of metadevice, we put another layer of graphene on PVC on the ionic liquid soaked tissue. This device structure resembles supercapacitors formed by single layer graphene electrodes. The simulation results guided us to find the optimum graphene-SRR separation of 300 μm. The electrolyte permits mutual electrolyte gating between the graphene electrodes without any metallic gate electrodes. Under an external bias voltage, the electrolyte gets polarized and electrostatically dopes the graphene electrodes. The graphene electrode connected to the negative voltage gets electron-doped (n-doped), whereas the other one gets hole-doped (p-doped).

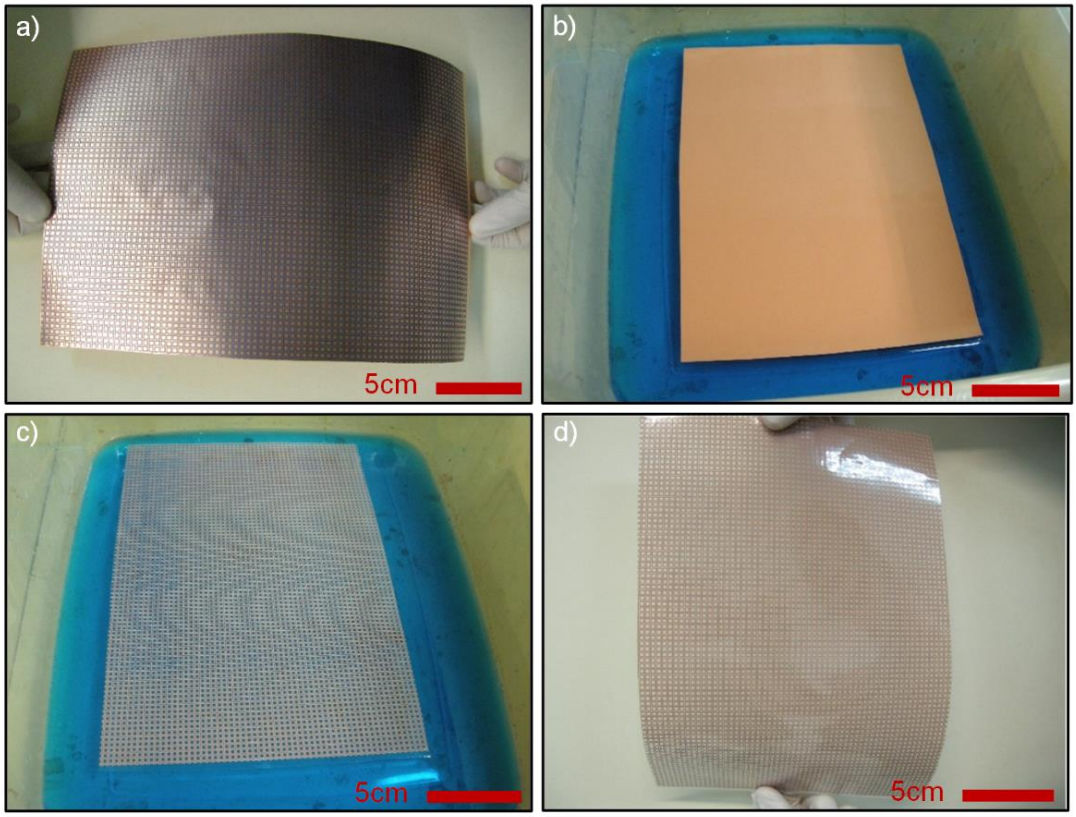

Figure 5.3 Fabrication of large area split ring resonator structure. a) A PVC film is laminated on 10μm thick, clean copper foil. SRR structure is printed on the laminated copper foil by using HP color laser jet printer (CP2020). The printed toner works as an etch mask. b), c) After printing SRR structure on laminated copper foil, the copper foil is etched in a nitric acid aqueous solution. The printed SRR patterns masks the laminated copper film to form SRR structure hence un-printed area on the copper is etched. d) Picture of the fabricated SRR structure on PVC substrate after washing and drying is shown.

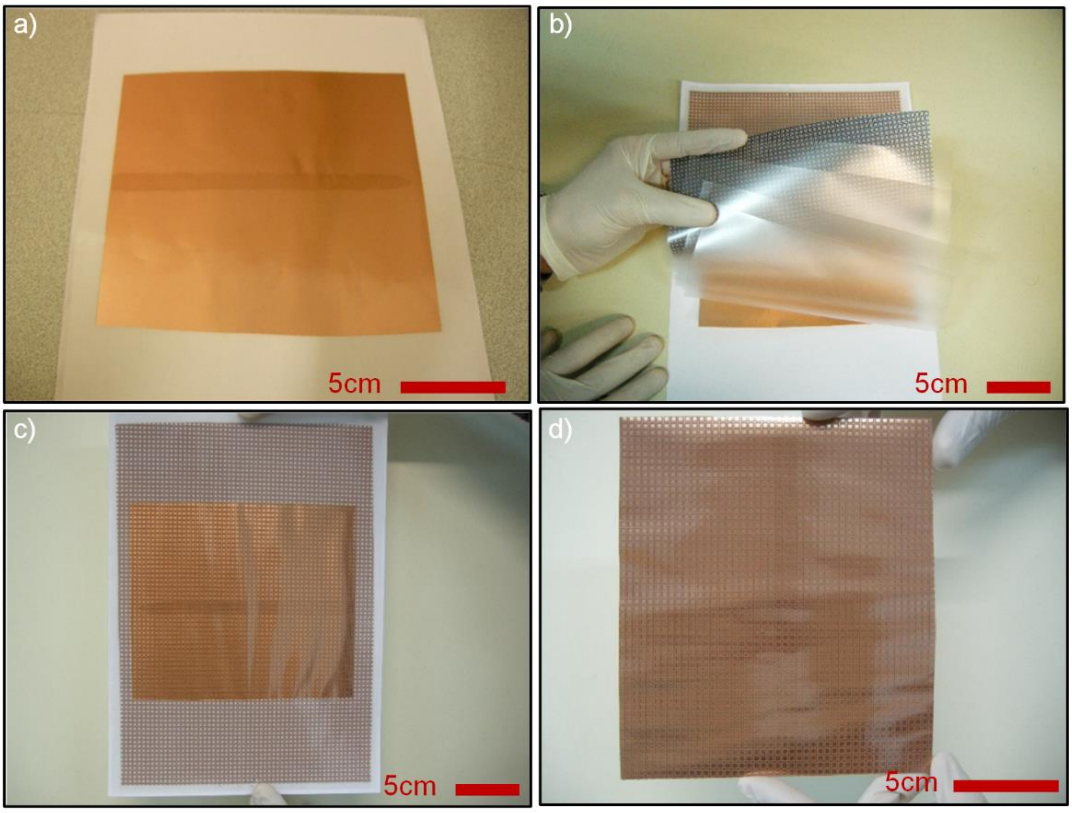

Figure 5.4 Lamination of fabricated SRR arrays on a graphene transferred PVC. a) Single layer graphene is grown on large area copper film and laminated onto polymer film (PVC). b) The SRR is laminated on graphene-grown copper. The four layers of PVC films are inserted between graphene grown copper and the SRR structure as a spacer between graphene and SRR array. c) Laminated SRR array on top of graphene grown copper. d) SRR laminated graphene grown copper is shown. The layers from top to bottom: SRR arrays, multiple PVC films, graphene grown copper foil.

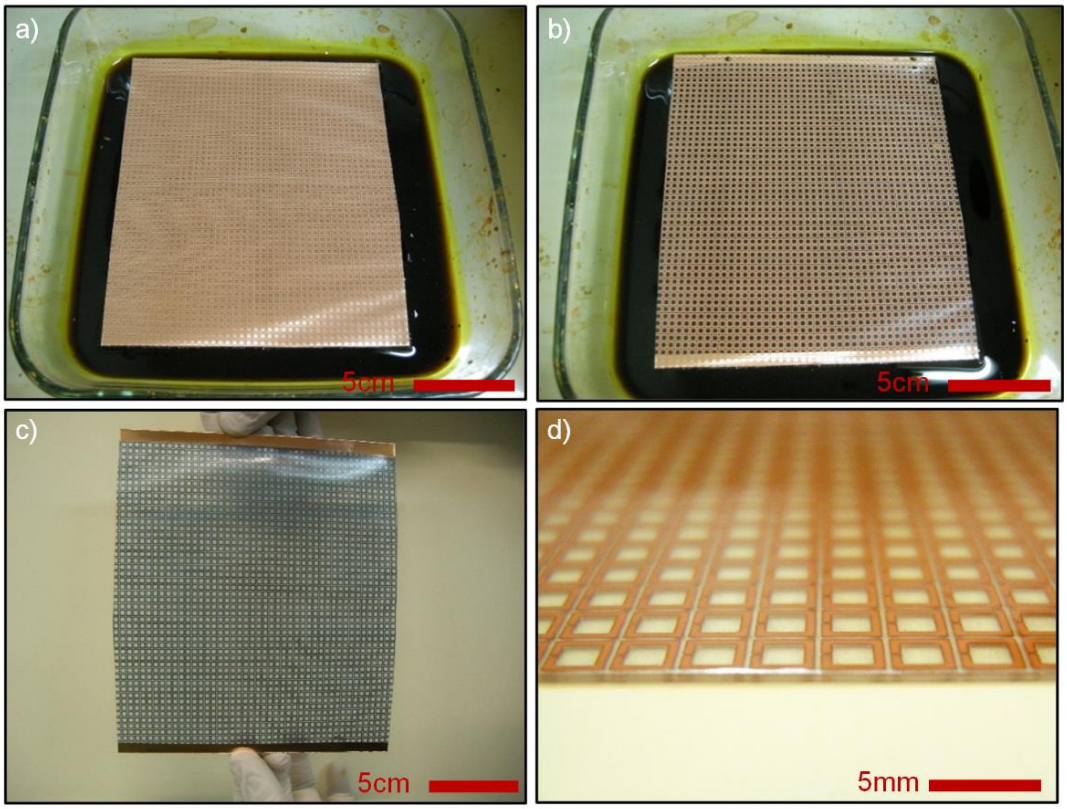

Figure 5.5 Etching the graphene grown copper laminated on the SRR arrays. a) We used 5mM $FeCl_3$ aqueous solution to etch the graphene grown copper foil, it gets 10min to etch 20μm thick copper foil. b), c) Picture of the graphene layer laminated on SRR arrays after etching the graphene grown copper foil. Two strip near the edge of the sample are contact metals used to take electrical contact from graphene layer. d) Picture of the fabricated graphene-SRR stack is shown, SRR arrays are at the top and graphene is at the bottom. Here four layers of PVC are used as a spacer between graphene and SRR arrays. The distance between the graphene layer and the SRR arrays is 3.5mm due to four layers of PVC.

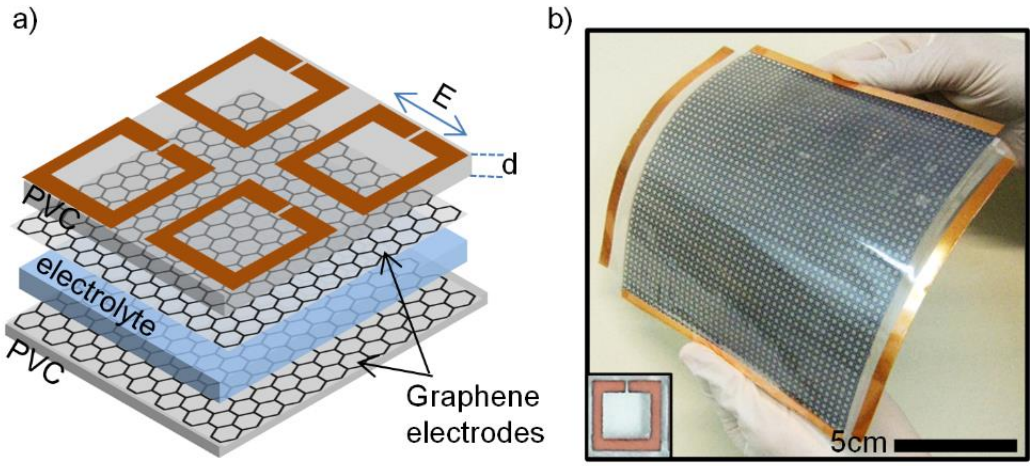

Figure 5.6 Electrically switchable metadevices. a) Schematic representation of the graphene supercapacitor integrated with split ring resonator. The graphene-SRR spacing is controlled by the thickness of the polymer PVC substrate. b), c) Photograph of the fabricated device. The graphene supercapacitor consists of two large area graphene transferred on PVC substrate and electrolyte medium between them. The inset shows SRR with a split gap of 85 μm.

5.3.Microwave response of graphene metadevice

After assembling the device, we measured the scattering parameters using broadband horn antennas and a two-port network analyzer. To excite the electrical resonance, we polarized the electric field along the split gap of SRR. A schematic drawing of two horn antennas and the graphene metadevice is presented in Figure 5.7. Figure 5.8(a) and Figure 5.9(a) show the amplitude and phase of the transmittance through the fabricated device at various bias voltages. At 0 V, the device yields a resonance at 11.02 GHz with a resonance transmittance of -65dB. When we applied a bias voltage, electrons and holes accumulate on the graphene electrodes and yield significant damping which diminishes the resonant behavior. At -3V, the resonance

transmittance is -20 dB (background level). The phase of the resonance also yields a substantial change. Figure 5.8(b) and Figure 5.9(b) show the voltage dependence of the amplitude of transmittance at resonance (11.02 GHz) and the phase at 11 GHz. The phase of the transmitted signal varies from -75^{o} to 22^{o}. We observed a symmetric behavior when we change the polarity of the bias voltage.

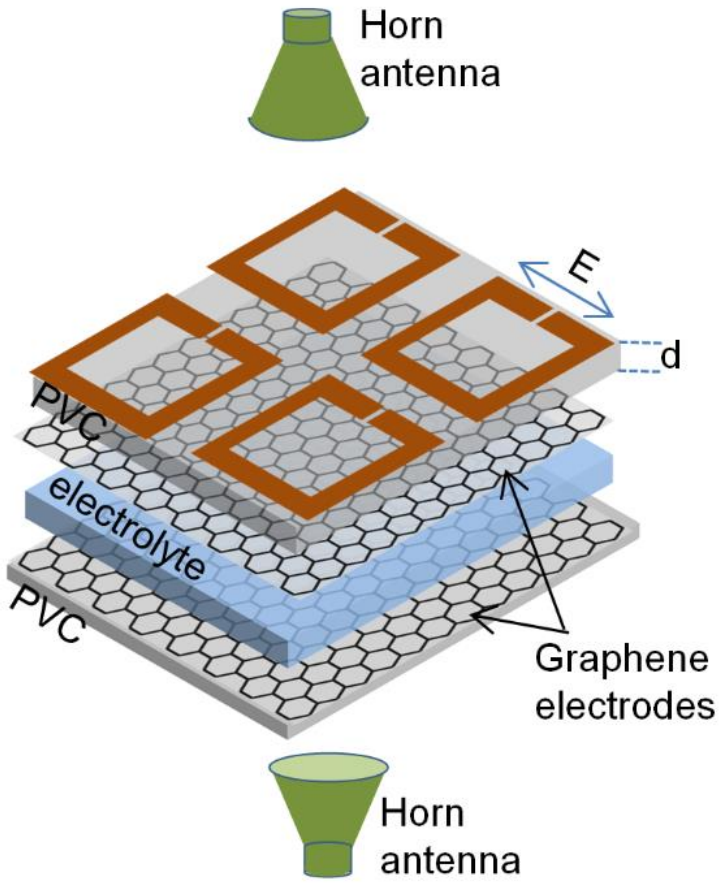

Figure 5.7 Schematic representation of microwave measurement setup for graphene metadevice. Fabricated device is located between two horn antennas connected to Keysight-E5063A network analyzer.

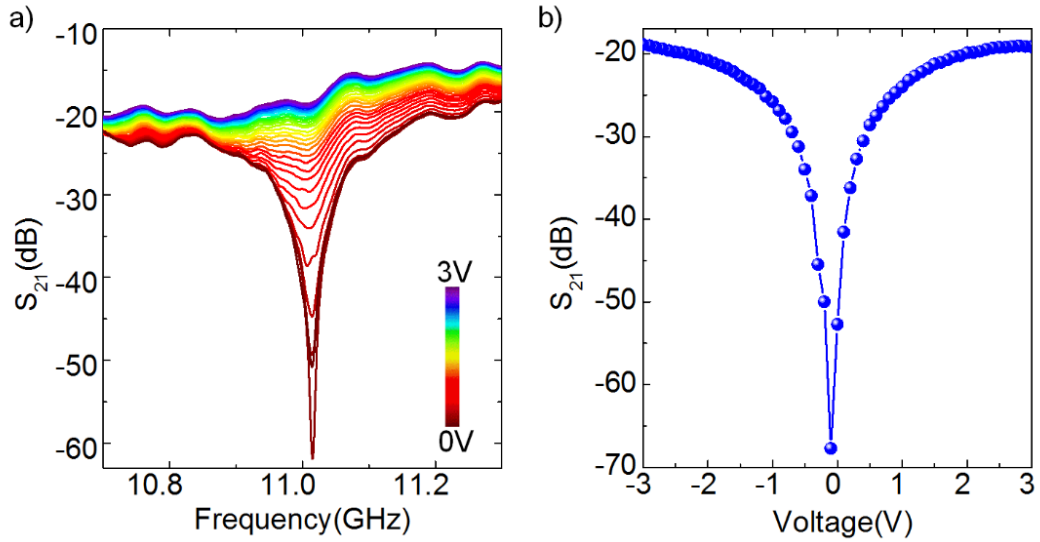

Figure 5.8 a) Frequency dependent magnitude of the transmittance at various bias voltages. The color bar shows the bias voltage. b) Voltage dependence of the amplitude of the transmittance at 11.02 GHz.

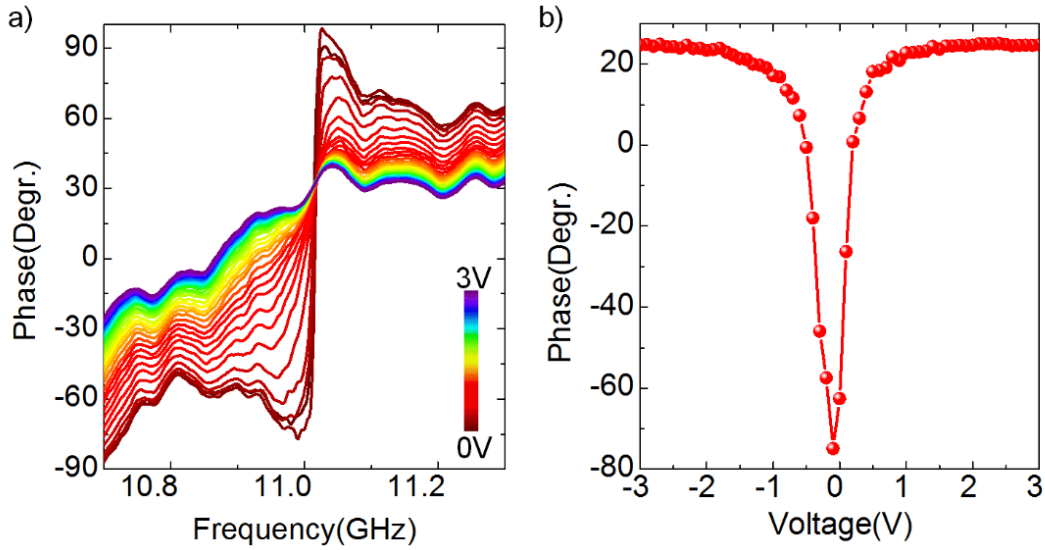

Figure 5.9 Phase modulation of transmittance as a function of frequency for varying bias voltages around resonance frequency of 11.02 GHz. b) Modulation depth of the phase as a function bias voltage at the frequency of 11 GHz.

To gain more insight of the metadevices, we measured the electrical characteristics of the graphene supercapacitor. We measured the voltage dependence of the capacitance of the device and sheet resistance of the graphene electrodes (Figure 5.10(a)) by applying a small alternating voltage (0.1 V at 20 Hz) superimposed with a variable DC voltage. The sheet resistance varies between 2.8 kΩ down to 0.5 kΩ, whereas the device capacitance increases from 0.7 to 2.8 μF/cm^2. The total capacitance is defined by the quantum capacitance of the electrodes because the thickness of the ionic double layers is around a few nanometers, which makes the electrostatic capacitance of electrical double layers much larger than the quantum capacitance of the device. The minimum capacitance is limited by the unintentional doping and charge puddle formation on graphene. From the capacitance measurements, we estimated that the charge density varies from 0.2 to 8x10^{13} cm^{-2}. We observed two peaks both in the voltage dependence of the resistance and capacitance due to the slight difference between the charge neutral points (Dirac point) of the top and bottom graphene electrodes. Figure 5.7(b) shows the variation of the resonance transmittance with the sheet resistance of the graphene electrodes. In comparison to the previously published results of tunable metamaterials, this device shows a much larger modulation depth (>50 dB) with low operation voltage (3V). The improved device performance is a result of the new hybrid structure formed by SRR capacitively coupled to the graphene layer. In this device structure, the tunable charge density yield large dynamic range and atomic thickness yield low insertion loss. There is an ability to control intensity, and phase yield another functionality.

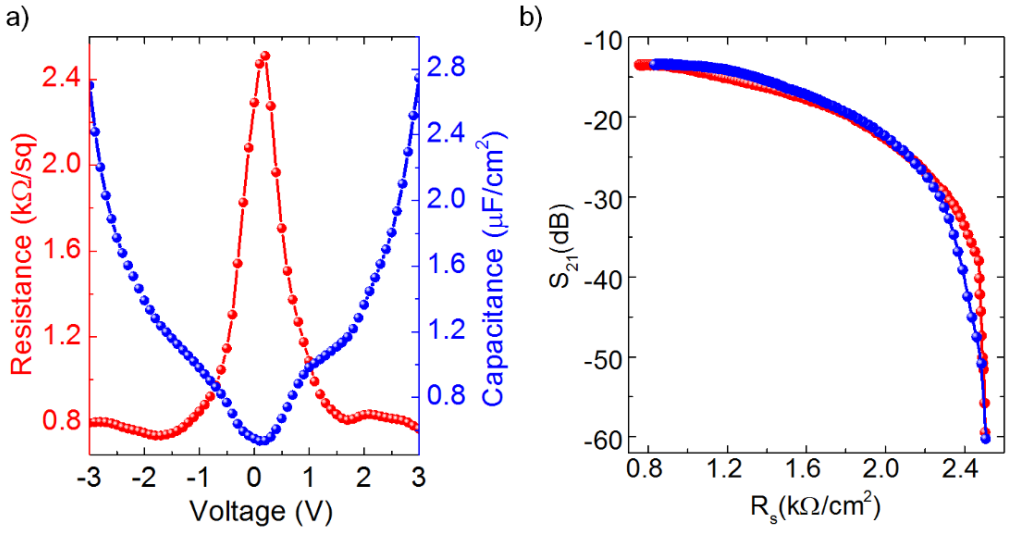

Figure 5.10 Electrical characteristics of the metadevices: a) Variation of the sheet resistance and capacitance of the device. b) The resonance transmittance of the metamaterials plotted against the sheet resistance of graphene electrodes.

The dynamic range of the metadevices depends on the capacitive coupling between the metamaterials and the graphene electrode. This coupling is determined by the thickness of the polymer substrate. To find the optimum thickness, predicted by the electromagnetic simulation, we fabricated different metadevices with different the graphene-SPR separation. Figure 5.11(a) shows the voltage dependent resonance transmittance for these devices. When the metamaterials are very close to the graphene layer, even unintentional doping on graphene is enough to diminish the resonance. Furthermore, the modulation depth is very limited as shown in Figure 5.11(b). Even with very large charge density modulation, the device with 0.15 mm spacing shows very little modulation (<10 dB). In the case of long distance (d > 500 μm), we observe a strong resonance with small modulation. We obtained an optimum thickness of 300 μm which yields a modulation depth of 50dB. The dynamic range of the device is limited by the tunability of the charge density on graphene layer. The electrochemical window of the ionic liquid electrolyte limits the maximum

accumulated charges. The unintentional doping, lack of electronic band gap and charge buddle formation limits the minimum charge density. Other 2D crystals with electronic band gap could provide a larger dynamic range.

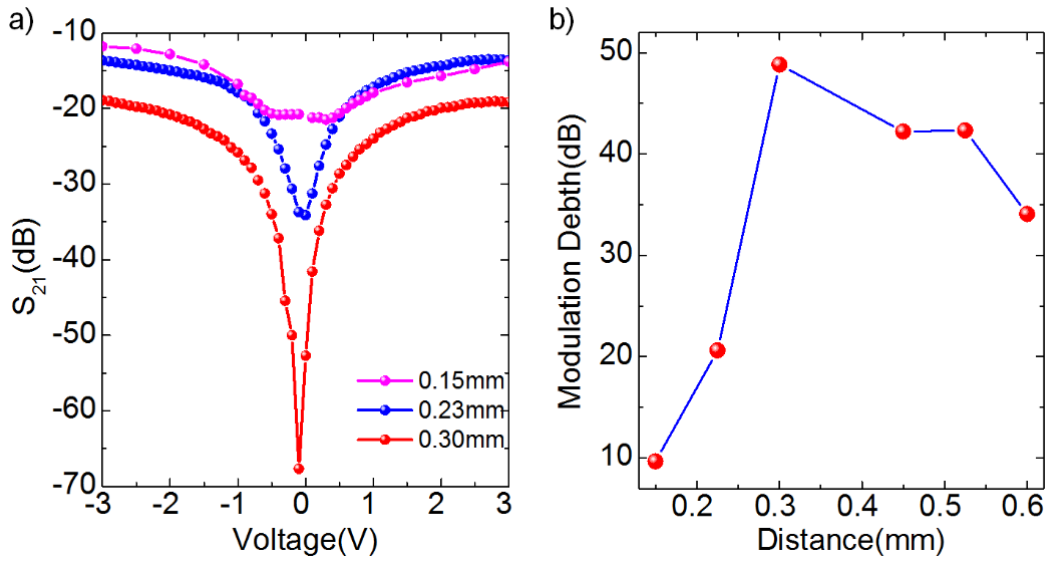

Figure 5.11 Optimization of the device performance: a) Voltage dependence of the resonance transmittance for metamaterial with different graphene-SRR separation. b) Modulation depth plotted against the graphene-SRR separation.

The results presented here confirm a promising approach for electrically controlled metadevices. The core idea of the approach is based on the electrical tuning of dissipation on metamaterials that are capacitively coupled to large area graphene electrodes. Electrostatic tuning of the charge density on graphene yields broadband controllability on metamaterials. The operation frequency of these metadevices can be easily scaled down to the terahertz frequency. Large modulation depth, simple device architecture and mechanical flexibility are the key attributes of the graphene-enabled metadevices. We anticipate that the presented approach could yield new applications ranging from electrically switchable clocking devices to adaptive camouflage systems in microwave and terahertz frequencies.

Chapter 6

Conclusion

In summary, we developed large area graphene based active microwave surfaces, for the first time, to control reflection, transmission and absorption of microwaves. We used large area graphene as an active material. Graphene has a tunable intraband optical absorption in microwave region of electromagnetic spectrum hence tuning the sheet resistance of graphene enables to control microwave optical response of graphene. For this purpose, we fabricated large area graphene supercapacitors by using two large area graphene electrodes and an ionic liquid between them. When we apply a voltage difference between two graphene electrodes of the supercapacitor, positive and negative ions are collected at graphene-ionic liquid interface called electrical double layer (EDL) having a thickness of few nanometer. High voltage drop in the small thickness of EDL create a high electric field on the surface of graphene electrodes. That high electric field shifts the Fermi energy of graphene above or below the Dirac point hence sheet resistance of graphene electrodes decrease. Using this gating mechanism of graphene electrodes, we controlled microwaves in free space. We developed three types of device structures; broad band microwave modulators, radar absorbing surfaces, and active metadevices.

Broad band microwave modulators are based on large area graphene supercapacitors. We measured the transmission and reflection of the device at 10GHz for varying sheet resistance values, and we calculated absorption by subtracting reflection and transmission amplitude from the incident radiation amplitude. As a result, we changed reflection from the surface of device from 2% to 20%,

transmission from 70% to 33% and hence absorption from 22% to 44%. We can actively control the optical response of our device in microwave. The second type of device that we developed is the active radar absorbing surfaces. This device is reflection type and can be used for active camouflage applications. We use large area graphene supercapacitor with a metal plate. We place the metal plate at a distance from the supercapacitor and we measured the microwave reflection from the surface of the device. Due to the resonant nature of the device, a resonant frequency is absorbed at 60dB ratio. The wavelength of the resonant frequency is four times the optical path between the metal plate and the graphene supercapacitor. When we vary the bias voltage on the graphene electrodes, we can tune absorption of the device with 50dB modulation depth. We investigated individually addressable hexagonal device structures to be able to cover nonplanar surfaces and we imaged their microwave absorbing performance. We also designed a cylindrical device structure to show flexibility of our radar absorbing surface. The third device is based on the integration of graphene supercapacitors with a metamaterial surface. Graphene supercapacitors are capacitively coupled to the metamaterial array by placing the device at a critical distance above the metamaterial array. When we change the sheet resistance of the graphene electrodes by applying a bias, we tune the coupling impedance and capacitance. In this way, we can control the resonance amplitude with 50dB and phase with 100^{o} modulation depth by varying the bias voltage.

In conclusion, we investigated the way of active controlling microwaves in free space by using unique device structure based on graphene. We extend our work to obtain high performance radar absorbing surfaces and individually addressable pixels of them. As a final application of our device, we integrated the device to a metamaterial surface to control amplitude and phase of the transmitted microwaves at resonance frequency. Our method of controlling microwaves can find applications in communication, signal processing, active camouflage, and invisibility cloaking technologies.

Bibliography

[1] F. Bonaccorso, Z. Sun, T. Hasan, and A. C. Ferrari, "Graphene photonics and optoelectronics," *Nature Photonics*, vol. 4, pp. 611-622, Sep 2010.

[2] F. Wang, Y. B. Zhang, C. S. Tian, C. Girit, A. Zettl, M. Crommie, *et al.*, "Gate-variable optical transitions in graphene," *Science*, vol. 320, pp. 206-209, Apr 11 2008.

[3] Z. Q. Li, E. A. Henriksen, Z. Jiang, Z. Hao, M. C. Martin, P. Kim, *et al.*, "Dirac charge dynamics in graphene by infrared spectroscopy," *Nature Physics*, vol. 4, pp. 532-535, Jul 2008.

[4] M. Liu, X. B. Yin, E. Ulin-Avila, B. S. Geng, T. Zentgraf, L. Ju, *et al.*, "A graphene-based broadband optical modulator," *Nature*, vol. 474, pp. 64-67, Jun 2 2011.

[5] E. O. Polat and C. Kocabas, "Broadband Optical Modulators Based on Graphene Supercapacitors," *Nano Letters*, vol. 13, pp. 5851-5857, Dec 2013.

[6] E. O. Polat, O. Balci, and C. Kocabas, "Graphene based flexible electrochromic devices," *Scientific Reports*, vol. 4, Oct 1 2014.

[7] B. Sensale-Rodriguez, R. S. Yan, M. M. Kelly, T. Fang, K. Tahy, W. S. Hwang, *et al.*, "Broadband graphene terahertz modulators enabled by intraband transitions," *Nature Communications*, vol. 3, Apr 2012.

[8] B. Sensale-Rodriguez, R. S. Yan, S. Rafique, M. D. Zhu, W. Li, X. L. Liang, *et al.*, "Extraordinary Control of Terahertz Beam Reflectance in Graphene Electro-absorption Modulators," *Nano Letters*, vol. 12, pp. 4518-4522, Sep 2012.

[9] N. Kakenov, T. Takan, V. A. Ozkan, O. Balci, E. O. Polat, H. Altan, *et al.*, "Graphene-enabled electrically controlled terahertz spatial light modulators," *Optics Letters*, vol. 40, pp. 1984-1987, May 1 2015.

[10] L. Ju, B. S. Geng, J. Horng, C. Girit, M. Martin, Z. Hao, *et al.*, "Graphene plasmonics for tunable terahertz metamaterials," *Nature Nanotechnology*, vol. 6, pp. 630-634, Oct 2011.

[11] R. Degl'Innocenti, D. S. Jessop, Y. D. Shah, J. Sibik, J. A. Zeitler, P. R. Kidambi, *et al.*, "Low-Bias Terahertz Amplitude Modulator Based on Split-Ring Resonators and Graphene," *Acs Nano*, vol. 8, pp. 2548-2554, Mar 2014.

[12] S. H. Lee, M. Choi, T. T. Kim, S. Lee, M. Liu, X. Yin, *et al.*, "Switching terahertz waves with gate-controlled active graphene metamaterials," *Nature Materials*, vol. 11, pp. 936-941, Nov 2012.

[13] F. Valmorra, G. Scalari, C. Maissen, W. Y. Fu, C. Schonenberger, J. W. Choi, *et al.*, "Low-Bias Active Control of Terahertz Waves by Coupling Large-Area CVD Graphene to a Terahertz Metamaterial," *Nano Letters*, vol. 13, pp. 3193-3198, Jul 2013.

[14] R. Degl'Innocenti, D. S. Jessop, Y. D. Shah, J. Sibik, A. Zeitler, P. R. Kidambi, *et al.*, "Graphene-based optical modulator realized in metamaterial split-ring resonators operating in the THz frequency range," *Terahertz, Rf, Millimeter, and Submillimeter-Wave Technology and Applications Vii,* vol. 8985, 2014.

[15] R. Saito, G. Dresselhaus, and M. S. Dresselhaus, *Physical properties of carbon nanotubes* vol. 35: World Scientific, 1998.

[16] A. H. Castro Neto, F. Guinea, N. M. R. Peres, K. S. Novoselov, and A. K. Geim, "The electronic properties of graphene," *Reviews of Modern Physics,* vol. 81, pp. 109-162, Jan-Mar 2009.

[17] L. A. Falkovsky, "Optical properties of graphene," *International Conference on Theoretical Physics 'Dubna-Nano2008',* vol. 129, 2008.

[18] N. M. R. Peres, F. Guinea, and A. H. Castro Neto, "Electronic properties of disordered two-dimensional carbon," *Physical Review B,* vol. 73, Mar 2006.

[19] T. Stauber, N. M. R. Peres, and A. K. Geim, "Optical conductivity of graphene in the visible region of the spectrum," *Physical Review B,* vol. 78, Aug 2008.

[20] T. Ando, Y. S. Zheng, and H. Suzuura, "Dynamical conductivity and zero-mode anomaly in honeycomb lattices," *Journal of the Physical Society of Japan,* vol. 71, pp. 1318-1324, May 2002.

[21] A. B. Kuzmenko, E. van Heumen, F. Carbone, and D. van der Marel, "Universal optical conductance of graphite," *Physical Review Letters,* vol. 100, Mar 21 2008.

[22] D. Brida, A. Tomadin, C. Manzoni, Y. J. Kim, A. Lombardo, S. Milana, *et al.*, "Ultrafast collinear scattering and carrier multiplication in graphene," *Nature Communications,* vol. 4, Jun 2013.

[23] T. R. Zhan, X. Shi, Y. Y. Dai, X. H. Liu, and J. Zi, "Transfer matrix method for optics in graphene layers," *Journal of Physics-Condensed Matter,* vol. 25, May 29 2013.

[24] H. Bosman, Y. Y. Lau, and R. M. Gilgenbach, "Microwave absorption on a thin film," *Applied Physics Letters,* vol. 82, pp. 1353-1355, Mar 3 2003.

[25] D. K. Ghodgaonkar, V. V. Varadan, and V. K. Varadan, "A Free-Space Method for Measurement of Dielectric-Constants and Loss Tangents at Microwave-Frequencies," *Ieee Transactions on Instrumentation and Measurement,* vol. 38, pp. 789-793, Jun 1989.

[26] Y. B. Feng, T. Qiu, C. Y. Shen, and X. Y. Li, "Electromagnetic and absorption properties of carbonyl iron/rubber radar absorbing materials," *Ieee Transactions on Magnetics,* vol. 42, pp. 363-368, Mar 2006.

[27] K. C. Pitman, M. W. Lindley, D. Simkin, and J. F. Cooper, "Radar Absorbers - Better by Design," *Iee Proceedings-F Radar and Signal Processing,* vol. 138, pp. 223-228, Jun 1991.

[28] K. L. Ford and B. Chambers, "Smart microwave absorber," *Electronics Letters,* vol. 36, pp. 50-52, Jan 6 2000.

[29] P. S. Neelakanta, A. K. Stampalia, and D. De Groff, "An actively-controlled microwave reflecting surface with binary-pattern modulation," *Microwave Journal,* vol. 46, pp. 22-+, Dec 2003.
[30] B. Chambers, "A smart radar absorber," *Smart Materials & Structures,* vol. 8, pp. 64-72, Feb 1999.
[31] P. S. Neelakanta, J. Abello, and C. L. Gu, "Microwave Reflection at an Active Surface Imbedded with Fast-Ion Conductors," *Ieee Transactions on Microwave Theory and Techniques,* vol. 40, pp. 1028-1030, May 1992.
[32] R. L. Haupt and M. Lanagan, "Reconfigurable Antennas," *Ieee Antennas and Propagation Magazine,* vol. 55, pp. 49-61, Feb 2013.
[33] J. B. Pendry, D. Schurig, and D. R. Smith, "Controlling electromagnetic fields," *Science,* vol. 312, pp. 1780-1782, Jun 23 2006.
[34] M. Mirsaneh, E. Furman, J. V. Ryan, M. T. Lanagan, and C. G. Pantano, "Frequency dependent electrical measurements of amorphous GeSbSe chalcogenide thin films," *Applied Physics Letters,* vol. 96, Mar 15 2010.
[35] P. V. Wright, B. Chambers, A. Barnes, K. Lees, and A. Despotakis, "Progress in smart microwave materials and structures," *Smart Materials & Structures,* vol. 9, pp. 273-279, Jun 2000.
[36] O. G. Vendik, E. K. Hollmann, A. B. Kozyrev, and A. M. Prudan, "Ferroelectric tuning of planar and bulk microwave devices," *Journal of Superconductivity,* vol. 12, pp. 325-338, Apr 1999.
[37] D. M. Pozar and V. Sanchez, "Magnetic Tuning of a Microstrip Antenna on a Ferrite Substrate," *Electronics Letters,* vol. 24, pp. 729-731, Jun 9 1988.
[38] R. C. Hansen and M. Burke, "Antennas with magneto-dielectrics," *Microwave and Optical Technology Letters,* vol. 26, pp. 75-78, Jul 20 2000.
[39] K. S. Novoselov, D. Jiang, F. Schedin, T. J. Booth, V. V. Khotkevich, S. V. Morozov, *et al.*, "Two-dimensional atomic crystals," *Proceedings of the National Academy of Sciences of the United States of America,* vol. 102, pp. 10451-10453, Jul 26 2005.
[40] K. S. Novoselov, A. K. Geim, S. V. Morozov, D. Jiang, M. I. Katsnelson, I. V. Grigorieva, *et al.*, "Two-dimensional gas of massless Dirac fermions in graphene," *Nature,* vol. 438, pp. 197-200, Nov 10 2005.
[41] C. Wang, X. J. Han, P. Xu, X. L. Zhang, Y. C. Du, S. R. Hu, *et al.*, "The electromagnetic property of chemically reduced graphene oxide and its application as microwave absorbing material," *Applied Physics Letters,* vol. 98, Feb 14 2011.
[42] V. K. Singh, A. Shukla, M. K. Patra, L. Saini, R. K. Jani, S. R. Vadera, *et al.*, "Microwave absorbing properties of a thermally reduced graphene oxide/nitrile butadiene rubber composite," *Carbon,* vol. 50, pp. 2202-2208, May 2012.
[43] X. G. Sun, "Effect of carbon nanotube content on the radar absorbing properties. of carbon nanotube/resin composites," *New Carbon Materials,* vol. 22, pp. 375-378, Dec 2007.

[44] X. C. Zhao, Z. M. Zhang, L. Y. Wang, K. Xi, Q. Q. Cao, D. H. Wang, *et al.*, "Excellent microwave absorption property of Graphene-coated Fe nanocomposites," *Scientific Reports,* vol. 3, Dec 5 2013.

[45] B. A. Wu, H. M. Tuncer, M. Naeem, B. Yang, M. T. Cole, W. I. Milne, *et al.*, "Experimental demonstration of a transparent graphene millimetre wave absorber with 28% fractional bandwidth at 140 GHz," *Scientific Reports,* vol. 4, Feb 19 2014.

[46] M. Dragoman, D. Neculoiu, D. Dragoman, G. Deligeorgis, G. Konstantinidis, A. Cismaru, *et al.*, "Graphene for Microwaves," *Ieee Microwave Magazine,* vol. 11, pp. 81-86, Dec 2010.

[47] R. J. Collier and D. G. Hasko, "Measurement of the sheet resistance of resistive films on thin substrates from 120 to 175 GHz using dielectric waveguides," *Journal of Applied Physics,* vol. 91, pp. 2547-2549, Feb 15 2002.

[48] Z. W. Zheng, C. J. Zhao, S. B. Lu, Y. Chen, Y. Li, H. Zhang, *et al.*, "Microwave and optical saturable absorption in graphene," *Optics Express,* vol. 20, pp. 23201-23214, Oct 8 2012.

[49] G. Deligeorgis, M. Dragoman, D. Neculoiu, D. Dragoman, G. Konstantinidis, A. Cismaru, *et al.*, "Microwave propagation in graphene," *Applied Physics Letters,* vol. 95, Aug 17 2009.

[50] Y. Q. Wu, Y. H. Xu, Z. G. Wang, C. Xu, Z. X. Tang, Y. F. Chen, *et al.*, "Microwave transmission properties of chemical vapor deposition graphene," *Applied Physics Letters,* vol. 101, Jul 30 2012.

[51] N. Chamanara, D. Sounas, T. Szkopek, and C. Caloz, "Optically Transparent and Flexible Graphene Reciprocal and Nonreciprocal Microwave Planar Components," *Ieee Microwave and Wireless Components Letters,* vol. 22, pp. 360-362, Jul 2012.

[52] J. P. Gogoi, N. S. Bhattacharyya, and S. Bhattacharyya, "Single layer microwave absorber based on expanded graphite-novolac phenolic resin composite for X-band applications," *Composites Part B-Engineering,* vol. 58, pp. 518-523, Mar 2014.

[53] T. Ando, A. B. Fowler, and F. Stern, "Electronic-Properties of Two-Dimensional Systems," *Reviews of Modern Physics,* vol. 54, pp. 437-672, 1982.

[54] A. K. Tagantsev, V. O. Sherman, K. F. Astafiev, J. Venkatesh, and N. Setter, "Ferroelectric materials for microwave tunable applications," *Journal of Electroceramics,* vol. 11, pp. 5-66, Sep-Nov 2003.

[55] C. H. Lee, N. D. Orloff, T. Birol, Y. Zhu, V. Goian, E. Rocas, *et al.*, "Exploiting dimensionality and defect mitigation to create tunable microwave dielectrics," *Nature,* vol. 502, pp. 532-+, Oct 24 2013.

[56] L. J. Buckley and D. Mohl, "Smart Polymeric Materials for Active Camouflage," *Active Materials and Adaptive Structures,* pp. 23-26, 1992.

[57] T. L. Rose, S. DAntonio, M. H. Jillson, A. B. Kon, R. Suresh, and F. Wang, "A microwave shutter using conductive polymers," *Synthetic Metals,* vol. 85, pp. 1439-1440, Feb 15 1997.

[58] J. L. Freeman, B. J. Lamberty, and G. S. Andrews, "Optoelectronically Reconfigurable Monopole Antenna," *Electronics Letters,* vol. 28, pp. 1502-1503, Jul 30 1992.

[59] G. Grewal and G. W. Hanson, "Optically-controlled solid-state plasma leaky-wave antenna," *Microwave and Optical Technology Letters,* vol. 39, pp. 450-453, Dec 20 2003.

[60] J. T. Bernhard, E. Kiely, and G. Washington, "A smart mechanically actuated two-layer electromagnetically coupled microstrip antenna with variable frequency, bandwidth, and antenna gain," *Ieee Transactions on Antennas and Propagation,* vol. 49, pp. 597-601, Apr 2001.

[61] G. Washington, H. S. Yoon, M. Angelino, and W. H. Theunissen, "Design, modeling, and optimization of mechanically reconfigurable aperture antennas," *Ieee Transactions on Antennas and Propagation,* vol. 50, pp. 628-637, May 2002.

[62] M. Tamagnone, A. Fallahi, J. R. Mosig, and J. Perruisseau-Carrier, "Fundamental limits and near-optimal design of graphene modulators and non-reciprocal devices," *Nature Photonics,* vol. 8, pp. 556-563, Jul 2014.

[63] S. Badhwar, R. Puddy, P. R. Kidambi, J. Sibik, A. Brewer, J. R. Freeman, *et al.*, "Indirect Modulation of a Terahertz Quantum Cascade Laser Using Gate Tunable Graphene," *Ieee Photonics Journal,* vol. 4, pp. 1776-1782, Oct 2012.

[64] B. Sensale-Rodriguez, T. Fang, R. S. Yan, M. M. Kelly, D. Jena, L. Liu, *et al.*, "Unique prospects for graphene-based terahertz modulators," *Applied Physics Letters,* vol. 99, Sep 12 2011.

[65] P. Y. Chen, J. Soric, Y. R. Padooru, H. M. Bernety, A. B. Yakovlev, and A. Alu, "Nanostructured graphene metasurface for tunable terahertz cloaking," *New Journal of Physics,* vol. 15, Dec 17 2013.

[66] A. Fallahi and J. Perruisseau-Carrier, "Design of tunable biperiodic graphene metasurfaces," *Physical Review B,* vol. 86, Nov 5 2012.

[67] J. S. Gomez-Diaz, C. Moldovan, S. Capdevila, J. Romeu, L. S. Bernard, A. Magrez, *et al.*, "Self-biased reconfigurable graphene stacks for terahertz plasmonics," *Nature Communications,* vol. 6, Mar 2015.

[68] P. Y. Chen and A. Alu, "Atomically Thin Surface Cloak Using Graphene Monolayers," *Acs Nano,* vol. 5, pp. 5855-5863, Jul 2011.

[69] B. Sensale-Rodriguez, R. S. Yan, L. Liu, D. Jena, and H. G. Xing, "Graphene for Reconfigurable Terahertz Optoelectronics," *Proceedings of the Ieee,* vol. 101, pp. 1705-1716, Jul 2013.

[70] K. F. Mak, L. Ju, F. Wang, and T. F. Heinz, "Optical spectroscopy of graphene: From the far infrared to the ultraviolet," *Solid State Communications,* vol. 152, pp. 1341-1349, Aug 2012.

[71] V. E. Dorgan, M. H. Bae, and E. Pop, "Mobility and saturation velocity in graphene on SiO2," *Applied Physics Letters,* vol. 97, Aug 23 2010.
[72] I. Baylam, M. N. Cizmeciyan, S. Ozharar, E. O. Polat, C. Kocabas, and A. Sennaroglu, "Femtosecond pulse generation with voltage-controlled graphene saturable absorber," *Optics Letters,* vol. 39, pp. 5180-5183, Sep 1 2014.
[73] S. Adam, E. H. Hwang, V. M. Galitski, and S. Das Sarma, "A self-consistent theory for graphene transport," *Proceedings of the National Academy of Sciences of the United States of America,* vol. 104, pp. 18392-18397, Nov 20 2007.
[74] M. Hayyan, F. S. Mjalli, M. A. Hashim, I. M. AlNashef, and T. X. Mei, "Investigating the electrochemical windows of ionic liquids," *Journal of Industrial and Engineering Chemistry,* vol. 19, pp. 106-112, Jan 25 2013.
[75] J. M. Woo, M. S. Kim, H. W. Kim, and J. H. Jang, "Graphene based salisbury screen for terahertz absorber," *Applied Physics Letters,* vol. 104, Feb 24 2014.
[76] B. Sensale-Rodriguez, S. Rafique, R. S. Yan, M. D. Zhu, V. Protasenko, D. Jena, *et al.*, "Terahertz imaging employing graphene modulator arrays," *Optics Express,* vol. 21, pp. 2324-2330, Jan 28 2013.
[77] C. M. Watts, D. Shrekenhamer, J. Montoya, G. Lipworth, J. Hunt, T. Sleasman, *et al.*, "Terahertz compressive imaging with metamaterial spatial light modulators," *Nature Photonics,* vol. 8, pp. 605-609, Aug 2014.
[78] E. Carrasco, M. Tamagnone, and J. Perruisseau-Carrier, "Tunable graphene reflective cells for THz reflectarrays and generalized law of reflection," *Applied Physics Letters,* vol. 102, Mar 11 2013.
[79] Y. J. Liu, D. Song, C. X. Wu, and J. S. Leng, "EMI shielding performance of nanocomposites with MWCNTs, nanosized Fe3O4 and Fe," *Composites Part B-Engineering,* vol. 63, pp. 34-40, Jul 2014.
[80] J. Joo and C. Y. Lee, "High frequency electromagnetic interference shielding response of mixtures and multilayer films based on conducting polymers," *Journal of Applied Physics,* vol. 88, pp. 513-518, Jul 1 2000.
[81] S. P. Gairola, V. Verma, L. Kumar, M. A. Dar, S. Annapoorni, and R. K. Kotnala, "Enhanced microwave absorption properties in polyaniline and nano-ferrite composite in X-band," *Synthetic Metals,* vol. 160, pp. 2315-2318, Nov 2010.
[82] A. Fletcher, M. C. Gupta, K. L. Dudley, and E. Vedeler, "Elastomer foam nanocomposites for electromagnetic dissipation and shielding applications," *Composites Science and Technology,* vol. 70, pp. 953-958, Jun 2010.
[83] R. Sharma, R. C. Agarwala, and V. Agarwala, "Development of radar absorbing nano crystals by microwave irradiation," *Materials Letters,* vol. 62, pp. 2233-2236, Jun 15 2008.
[84] J. H. Oh, K. S. Oh, C. G. Kim, and C. S. Hong, "Design of radar absorbing structures using glass/epoxy composite containing carbon black in X-band frequency ranges," *Composites Part B-Engineering,* vol. 35, pp. 49-56, 2004.

[85] H. Tao, W. J. Padilla, X. Zhang, and R. D. Averitt, "Recent Progress in Electromagnetic Metamaterial Devices for Terahertz Applications," *Ieee Journal of Selected Topics in Quantum Electronics*, vol. 17, pp. 92-101, Jan-Feb 2011.

[86] E. Ozbay, "Plasmonics: Merging photonics and electronics at nanoscale dimensions," *Science*, vol. 311, pp. 189-193, Jan 13 2006.

[87] D. Shin, Y. Urzhumov, Y. Jung, G. Kang, S. Baek, M. Choi, *et al.*, "Broadband electromagnetic cloaking with smart metamaterials," *Nat Commun*, vol. 3, Nov 2012.

[88] N. I. Zheludev and Y. S. Kivshar, "From metamaterials to metadevices," *Nature Materials*, vol. 11, pp. 917-924, Nov 2012.

[89] Y. Urzhumov, J. S. Lee, T. Tyler, S. Dhar, V. Nguyen, N. M. Jokerst, *et al.*, "Electronically reconfigurable metal-on-silicon metamaterial," *Physical Review B*, vol. 86, Aug 8 2012.

[90] M. D. Goldflam, T. Driscoll, B. Chapler, O. Khatib, N. M. Jokerst, S. Palit, *et al.*, "Reconfigurable gradient index using VO2 memory metamaterials," *Applied Physics Letters*, vol. 99, Jul 25 2011.

[91] J. P. Turpin, J. A. Bossard, K. L. Morgan, D. H. Werner, and P. L. Werner, "Reconfigurable and Tunable Metamaterials: A Review of the Theory and Applications," *International Journal of Antennas and Propagation*, 2014.

[92] T. H. Hand and S. A. Cummer, "Reconfigurable Reflectarray Using Addressable Metamaterials," *Ieee Antennas and Wireless Propagation Letters*, vol. 9, pp. 70-74, 2010.

[93] F. Costa, A. Monorchio, and G. P. Vastante, "Tunable High-Impedance Surface With a Reduced Number of Varactors," *Ieee Antennas and Wireless Propagation Letters*, vol. 10, pp. 11-13, 2011.

[94] O. Reynet and O. Acher, "Voltage controlled metamaterial," *Applied Physics Letters*, vol. 84, pp. 1198-1200, Feb 16 2004.

[95] K. Aydin and E. Ozbay, "Capacitor-loaded split ring resonators as tunable metamaterial components," *Journal of Applied Physics*, vol. 101, Jan 15 2007.

[96] D. H. Werner, D. H. Kwon, and I. C. Khoo, "Liquid crystal clad near-infrared metamaterials with tunable negative-zero-positive refractive indices," *Optics Express*, vol. 15, pp. 3342-3347, Mar 19 2007.

[97] D. F. Gardner, J. S. Evans, and I. I. Smalyukh, "Towards Reconfigurable Optical Metamaterials: Colloidal Nanoparticle Self-Assembly and Self-Alignment in Liquid Crystals," *Molecular Crystals and Liquid Crystals*, vol. 545, pp. 1227-1245, 2011.

[98] A. B. Golovin and O. D. Lavrentovich, "Electrically reconfigurable optical metamaterial based on colloidal dispersion of metal nanorods in dielectric fluid," *Applied Physics Letters*, vol. 95, Dec 21 2009.

[99] J. Han and A. Lakhtakia, "Semiconductor split-ring resonators for thermally tunable terahertz metamaterials," *Journal of Modern Optics*, vol. 56, pp. 554-557, 2009.

[100] J. G. Han, A. Lakhtakia, and C. W. Qiu, "Terahertz metamaterials with semiconductor split-ring resonators for magnetostatic tunability," *Optics Express*, vol. 16, pp. 14390-14396, Sep 15 2008.
[101] J. Q. Wang, S. C. Liu, S. Guruswamy, and A. Nahata, "Reconfigurable liquid metal based terahertz metamaterials via selective erasure and refilling to the unit cell level," *Applied Physics Letters*, vol. 103, Nov 25 2013.
[102] H. T. Chen, W. J. Padilla, J. M. O. Zide, A. C. Gossard, A. J. Taylor, and R. D. Averitt, "Active terahertz metamaterial devices," *Nature*, vol. 444, pp. 597-600, Nov 30 2006.
[103] H. T. Chen, W. J. Padilla, M. J. Cich, A. K. Azad, R. D. Averitt, and A. J. Taylor, "A metamaterial solid-state terahertz phase modulator," *Nature Photonics*, vol. 3, pp. 148-151, Mar 2009.
[104] J. Y. Ou, E. Plum, J. F. Zhang, and N. I. Zheludev, "An electromechanically reconfigurable plasmonic metamaterial operating in the near-infrared," *Nature Nanotechnology*, vol. 8, pp. 252-255, Apr 2013.
[105] H. Tao, A. C. Strikwerda, K. B. Fan, W. J. Padilla, X. Zhang, and R. D. Averitt, "MEMS Based Structurally Tunable Metamaterials at Terahertz Frequencies," *Journal of Infrared Millimeter and Terahertz Waves*, vol. 32, pp. 580-595, May 2011.
[106] H. Tao, A. C. Strikwerda, K. Fan, W. J. Padilla, X. Zhang, and R. D. Averitt, "Reconfigurable Terahertz Metamaterials," *Physical Review Letters*, vol. 103, Oct 2 2009.
[107] F. S. Ma, Y. S. Lin, X. H. Zhang, and C. Lee, "Tunable multiband terahertz metamaterials using a reconfigurable electric split-ring resonator array," *Light-Science & Applications*, vol. 3, May 2014.
[108] I. M. Pryce, K. Aydin, Y. A. Kelaita, R. M. Briggs, and H. A. Atwater, "Highly Strained Compliant Optical Metamaterials with Large Frequency Tunability," *Nano Letters*, vol. 10, pp. 4222-4227, Oct 2010.
[109] B. Sensale-Rodriguez, R. S. Yan, M. M. Kelly, T. Fang, K. Tahy, W. S. Hwang, *et al.*, "Broadband graphene terahertz modulators enabled by intraband transitions," *Nat Commun*, vol. 3, Apr 2012.
[110] P. Tassin, T. Koschny, and C. M. Soukoulis, "Graphene for Terahertz Applications," *Science*, vol. 341, pp. 620-621, Aug 9 2013.
[111] N. Rouhi, S. Capdevila, D. Jain, K. Zand, Y. Y. Wang, E. Brown, *et al.*, "Terahertz graphene optics," *Nano Research*, vol. 5, pp. 667-678, Oct 2012.
[112] N. K. Emani, T. F. Chung, X. J. Ni, A. V. Kildishev, Y. P. Chen, and A. Boltasseva, "Electrically Tunable Damping of Plasmonic Resonances with Graphene," *Nano Letters*, vol. 12, pp. 5202-5206, Oct 2012.
[113] Y. Yao, M. A. Kats, P. Genevet, N. F. Yu, Y. Song, J. Kong, *et al.*, "Broad Electrical Tuning of Graphene-Loaded Plasmonic Antennas," *Nano Letters*, vol. 13, pp. 1257-1264, Mar 2013.

[114] J. Kim, H. Son, D. J. Cho, B. S. Geng, W. Regan, S. F. Shi, *et al.*, "Electrical Control of Optical Plasmon Resonance with Graphene," *Nano Letters*, vol. 12, pp. 5598-5602, Nov 2012.
[115] S. H. Lee, J. Choi, H. D. Kim, H. Choi, and B. Min, "Ultrafast refractive index control of a terahertz graphene metamaterial," *Scientific Reports*, vol. 3, Jul 4 2013.
[116] E. E. P. Osman Balci, Nurbek Kakenov, Coskun Kocabas, "Graphene-enabled electrically switchable radar absorbing surfaces," *Nature Communications*, vol. in press, 2015.
[117] S. Bae, H. Kim, Y. Lee, X. F. Xu, J. S. Park, Y. Zheng, *et al.*, "Roll-to-roll production of 30-inch graphene films for transparent electrodes," *Nature Nanotechnology*, vol. 5, pp. 574-578, Aug 2010.